

1989

## Local density approximation study of transition and f-electron materials

Zhi Wei Lu

*College of William & Mary - Arts & Sciences*

Follow this and additional works at: <https://scholarworks.wm.edu/etd>



Part of the [Condensed Matter Physics Commons](#)

---

### Recommended Citation

Lu, Zhi Wei, "Local density approximation study of transition and f-electron materials" (1989). *Dissertations, Theses, and Masters Projects*. Paper 1539623781. <https://dx.doi.org/doi:10.21220/s2-mg9r-bp62>

This Dissertation is brought to you for free and open access by the Theses, Dissertations, & Master Projects at W&M ScholarWorks. It has been accepted for inclusion in Dissertations, Theses, and Masters Projects by an authorized administrator of W&M ScholarWorks. For more information, please contact [scholarworks@wm.edu](mailto:scholarworks@wm.edu).

## INFORMATION TO USERS

The most advanced technology has been used to photograph and reproduce this manuscript from the microfilm master. UMI films the text directly from the original or copy submitted. Thus, some thesis and dissertation copies are in typewriter face, while others may be from any type of computer printer.

The quality of this reproduction is dependent upon the quality of the copy submitted. Broken or indistinct print, colored or poor quality illustrations and photographs, print bleedthrough, substandard margins, and improper alignment can adversely affect reproduction.

In the unlikely event that the author did not send UMI a complete manuscript and there are missing pages, these will be noted. Also, if unauthorized copyright material had to be removed, a note will indicate the deletion.

Oversize materials (e.g., maps, drawings, charts) are reproduced by sectioning the original, beginning at the upper left-hand corner and continuing from left to right in equal sections with small overlaps. Each original is also photographed in one exposure and is included in reduced form at the back of the book. These are also available as one exposure on a standard 35mm slide or as a 17" x 23" black and white photographic print for an additional charge.

Photographs included in the original manuscript have been reproduced xerographically in this copy. Higher quality 6" x 9" black and white photographic prints are available for any photographs or illustrations appearing in this copy for an additional charge. Contact UMI directly to order.

# U·M·I

University Microfilms International  
A Bell & Howell Information Company  
300 North Zeeb Road, Ann Arbor, MI 48106-1346 USA  
313/761-4700 800/521-0600



Order Number 8923167

**Local density approximation study of transition and f-electron  
materials**

Lu, Zhi Wei, Ph.D.

The College of William and Mary, 1989

**U·M·I**  
300 N. Zeeb Rd.  
Ann Arbor, MI 48106



LOCAL DENSITY APPROXIMATION STUDY  
OF TRANSITION AND f-ELECTRON MATERIALS

---

A Dissertation

Presented to

The Faculty of the Department of Physics  
The College of William and Mary in Virginia

In Partial Fulfillment

Of the Requirements for the Degree of  
Doctor of Philosophy

---

by

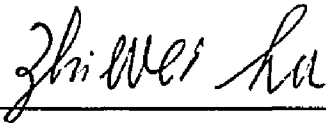
Zhi Wei Lu

May 1989

APPROVAL SHEET

This dissertation is submitted in partial fulfillment of  
the requirements of the degree of


Doctor of Philosophy



---

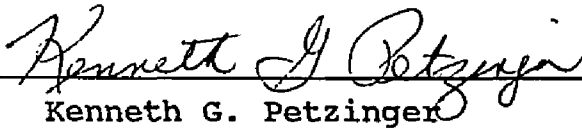
Zhi Wei Lu

Approved, May 1989



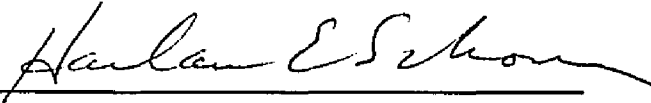
---

Henry Krakauer



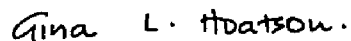
---

Kenneth G. Petzinger



---

Harlan E. Schone



---

Gina L. Hoatson



---

Gary C. Defotis (Chemistry Dept.)

## CONTENTS

<b>ACKNOWLEDGMENTS</b> . . . . .	v
<b>LIST OF TABLES</b> . . . . .	vi
<b>LIST OF FIGURES</b> . . . . .	ix
<b>ABSTRACTS</b> . . . . .	xv

Chapter	page
<b>I. FOREWORD</b> . . . . .	2
purposes . . . . .	2
local density approximation . . . . .	5
corrections beyond the LDA . . . . .	11
<b>II. LAPW METHOD</b> . . . . .	13
introduction . . . . .	13
basis functions . . . . .	14
potential . . . . .	17
hamiltonian and overlap matrices . . . . .	21
charge density . . . . .	23
total energy . . . . .	25
<b>III. TITANIUM AND ZIRCONIUM</b> . . . . .	31
introduction . . . . .	31
details of calculation . . . . .	32
equilibrium properties . . . . .	33
electronic properties . . . . .	46
summary . . . . .	52
<b>IV. FCC AND BCC LANTHANUM</b> . . . . .	59
introduction . . . . .	59
details of calculation . . . . .	60
total energy calculations . . . . .	61
band structure and density of states . . . . .	71
summary . . . . .	79
<b>V. LDA STUDY OF LaS AND SmS</b> . . . . .	80
introduction . . . . .	80



	structural properties . . . . .	81
	band structures . . . . .	89
	summary . . . . .	100
<b>VI.</b>	<b>PRESSURE INDUCED PHASE TRANSITIONS IN HgSe AND HgTe . . . . .</b>	<b>101</b>
	introduction . . . . .	101
	calculational detail . . . . .	103
	structural properties . . . . .	104
	(a) zinc-blende phase . . . . .	105
	(b) high pressure phases . . . . .	107
	electronic properties . . . . .	111
	summary . . . . .	126
<b>VII.</b>	<b>Pd(111) SURFACE RELAXATION . . . . .</b>	<b>127</b>
	introduction . . . . .	127
	details of calculation . . . . .	128
	bulk fcc Pd . . . . .	131
	Pd(111) . . . . .	136
	(a) surface relaxation . . . . .	136
	(b) electronic structure . . . . .	140
	summary . . . . .	148
<b>VIII.</b>	<b>CONCLUSIONS . . . . .</b>	<b>149</b>
	<b>REFERENCES . . . . .</b>	<b>150</b>

## ACKNOWLEDGEMENTS

Once again, it is getting so beautiful around the Williamsburg area, where I have spent my last few years. I feel attached to this place, particularly the Physics department, the William Small Laboratory, and the friends I will leave behind.

First, I would like to thank my adviser Henry Krakauer, for his constant guidance, support, and sincere encouragement throughout the course of my thesis work. Thank also goes to David Singh, for his useful advice and helpful discussions.

I would also take this opportunity to express my feeling towards the invincible Physics volleyball team. I have enjoyed playing volleyball with y'all.

It is also a time to say farewell to my friends. I wish to thank y'all for your help during my years in William and Mary. Thanks goes to Doug Baker, Eric Cheung, Harris Hoke, MuYu Guo, David Garren, C.W. Sun, Rick "capt." Weening, Tim Williams ...

I also want to thank Drs. Ken Petzinger, Harlan Schone, Gina Hoatson, and Gary Defotis for serving on my committee.

Finally, I wish to express my deep gratitude to my parents for their patience, support, and encouragement.

## LIST OF TABLES

Table	page
2.1 Precision requirement for various structural quantities. . . . .	26
3.1 $E(c/a) + C$ versus $c/a$ at the calculated equilibrium volume for Ti. For the HL, $V_0 = 109.21$ a.u. <sup>3</sup> , $C = 1703$ Ry and $E(V_0) = -1703.97798$ Ry. For the $X\alpha$ , $V_0 = 116.65$ a.u. <sup>3</sup> , $C = 1700$ Ry and $E(V_0) = -1700.41153$ Ry. . . . .	36
3.2 $E(c/a) + C$ versus $c/a$ at the calculated equilibrium volume for Zr. For the HL, $V_0 = 147.85$ a.u. <sup>3</sup> , $C = 7190$ Ry and $E(V_0) = -7190.42068$ Ry. For the $X\alpha$ , $V_0 = 158.92$ a.u. <sup>3</sup> , $C = 7183$ Ry and $E(V_0) = -7183.26556$ Ry. . . . .	37
3.3 Minimum $E(V) + C$ (Ry) as determined from Eq. (1) vs volume $V$ (a.u. <sup>3</sup> ) and the corresponding $c/a$ ratio for Ti. For the HL, $C = 1703$ Ry. For the $X\alpha$ , $C = 1700$ Ry. . . . .	40
3.4 Minimum $E(V) + C$ (Ry) as determined from Eq. (1) vs volume $V$ (a.u. <sup>3</sup> ) and the corresponding $c/a$ ratio for Zr. For the HL, $C = 7190$ Ry. For the $X\alpha$ , $C = 7183$ Ry. . . . .	41
3.5 Ground state properties of Ti in the hcp structure and a comparison with the experimental data. The experimental data are from Ref. Vil85, Kit76 and Fis64. . . . .	44
3.6 Ground state properties of Zr in the hcp structure and a comparison with the experimental data. The experimental data are from Ref. Vil85, Kit76 and Fis64. . . . .	46
3.7 Spin-polarized total energies for isolated atom Ti and Zr, $E_{\text{atom}}$ , and minimum total energies for hcp Ti and Zr, $E(V_0)$ . . . . .	51
4.1 Calculated and experimental lattice constants	

	and bulk moduli for fcc lanthanum. . . . .	66
4.2	Calculated total energy minimum $E_{\min}$ and corresponding lattice parameter $a_{\min}$ for three different exchange correlation potentials, the $X\alpha$ , Wigner and H-L form. . . . .	67
4.3	Calculation for isolated La atom with three different XC potentials. . . . .	67
4.4	Calculated and experimental lattice constants and bulk moduli for bcc lanthanum. . . . .	70
4.5	Band structure parameters (in mRy) as defined in Pickett <i>et al.</i> (Pic80) for fcc La at $a=10.0348$ a.u. . . . .	72
4.6	Density of states ( states/Ry atom ) of fcc La at $a=10.0348$ a. u. at Fermi Level $N(E_f)$ . . . . .	78
5.1	Muffin-tin radii used in the calculations for S, La and Sm. . . . .	81
5.2	Calculated total energies + 21650 Ry versus lattice parameter for SmS ( $a_{\text{expt}} = 11.289$ a.u. ). . . . .	87
5.3	Equilibrium properties of SmS. . . . .	87
6.1	The ground state (ZnS phase) properties of HgTe and HgSe. . . . .	107
6.2	Equation of state fits for the high pressure phases of HgTe and HgSe, $E_{\min}$ are relative to that of the ZnS phase, $V_{\text{expt}}$ are the equilibrium volumes of both materials. . . . .	108
6.3	Transition pressure from the NaCl to the $\beta$ -Sn phase for HgTe and HgSe and corresponding specific volumes (with respect to the equilibrium volumes). . . . .	110
6.4	Calculated band gaps $E_g$ both scalar-relativistically (SR) and fully relativistically (R), center of d-band $\epsilon_d$ , spin-orbit splittings of valence bands at $\Gamma(\Delta_0)$ and $L(\Delta_1)$ , and Hg d bands $\Delta_d$ , for HgTe and HgSe. All energies are in eV. . . . .	120
7.1	Energy eigenvalues relative to the Fermi energy (in mRy) at the symmetry points $\Gamma$ and L, and comparison with the previous	

	calculations and experiment. . . . .	132
7.2	Density of states at the Fermi energy at the experimental volume. . . . .	136
7.3	Bulk Pd structural properties. . . . .	136
7.4	Work function for Pd(111) . . . . .	140
7.5	Surface state and surface resonances for Pd(111) relative to the Fermi energy (in eV). . . . .	141

## LIST OF FIGURES

Figure	page
2.1 Flow diagram of the LAPW method. . . . .	30
3.1 (a) Unit cell for the hexagonal-close-packed crystal structure. (b) Half of the Brillouin zone for the hexagonal-close -packed structure with the 1/24th zone. . .	34
3.2 Calculated $E(V)-E(V_0)$ vs $V$ of Ti with the HL and the $X\alpha$ , the solid line is a Murnaghan equation of state fit. $E(V_0) = -1703.97798$ Ry for the HL and $E(V_0) = -1700.41153$ Ry for the $X\alpha$ . . . . .	38
3.3 Calculated $E(V)-E(V_0)$ vs $V$ of Zr with the HL and the $X\alpha$ , the solid line is a Murnaghan equation of state fit. $E(V_0) = -7190.42068$ Ry for the HL and $E(V_0) = -7183.26556$ Ry for the $X\alpha$ . . . . .	39
3.4 $c/a$ ratio corresponding to the minimum energy at certain volume versus volume for Ti and Zr. $\circ$ for the HL, $\bullet$ for the $X\alpha$ , and $*$ for the experimental $c/a$ ratio at experimental volume. . . . .	42
3.5 Linear relationship between $c$ and $a_{min}$ gives Poisson's ratio ( see text ). $+$ for the HL and $*$ for the $X\alpha$ . . . . .	47
3.6 Band structure for Ti using the HL XC. . . . .	49
3.7 Band structure for Ti at equilibrium lattice constants using the $X\alpha$ and the HL are nearly identical; see Fig. 3.6 for labels.	50
3.8 Density of states for Ti and Zr (the $X\alpha$ poten- tial). The Fermi energy is indicated by the dashed line. . . . .	53
3.9 Contour plot of the valence charge density of Ti calculated using the $X\alpha$ potential. The charge density is given in units of	

	$10^{-2} e/a.u.^3$ ; the step size is 2. . . . .	54
3.10	Band structure for Zr using the HL. . . . .	55
3.11	Band structure for Zr using the $X\alpha$ and HL at equilibrium lattice constants are very similar, see Fig. 3.10 for labels. . . . .	56
3.12	Contour plot of the valence charge density of Ti Calculated using the $X\alpha$ potential. The charge density is given in units of $10^{-2} e/a.u.^3$ ; the step size is 1. . . . .	57
4.1	(a) unit cell for face centered cubic structure, (b) unit cell for body centered cubic structure, (c) first Brillouin zone for fcc, and (d) first Brillouin zone for bcc. . . . .	62
4.2	Calculated total energy - $E_{min}$ vs. volume for fcc La for the $X\alpha$ , Wigner and H-L form respectively, the solid lines being their respective Murnaghan equation of state fit. For the $X\alpha$ form, the lower curve was determined including the spin-orbit interaction, while the upper curve omits it. . . . .	64
4.3	Calculated total energy - $E_{min}$ vs. volume for bcc La and the Murnaghan equation of state fit. . . . .	69
4.4	Semirelativistic band structure of fcc La at $a=10.0348$ a.u. using $X\alpha$ exchange correlation potential. . . . .	73
4.5	Density of states of fcc La at $a=10.0348$ a.u. . . . .	74
4.6	Charge density contours for fcc La calculated with the $X\alpha$ XC potential in units $10^{-3} e/a.u.^3$ ; the step size is 1. . . . .	75
4.7	Semirelativistic band structure of bcc La at $a=8.050$ a.u. using $X\alpha$ exchange correlation potential. . . . .	76
4.8	Density of states of bcc La at $a=8.050$ a.u. (Note the change in the vertical scale from the fcc DOS). . . . .	77
5.1	Calculated total energy + 17778.43550 Ry vs. volume for LaS. The solid line is a fit to the Murnaghan equation of state. . . . .	83

5.2	Calculated total energy - $E_{\min}$ Versus volume for SmS, open circles are for $f$ -electrons treated as valence electrons $E_{\min} = -21650.71103$ Ry, while filled circles are for $f$ -electrons treated as core electrons $E_{\min} = -21650.56872$ Ry (see text). The solid lines are fits to the Murnaghan equation of state. . . . .	86
5.3	Band structure of LaS at the experimental volume, dashed line indicates the Fermi level. . . . .	91
5.4	Density of states of LaS at the experimental volume. . . . .	92
5.5	Band structure of SmS at the experimental volume. . . . .	93
5.6	Detail band structure (5.5) about the Fermi energy. . . . .	94
5.7	Density of states of SmS at the experimental volume. . . . .	95
5.8	A detailed view of Fig. 5.7 about the Fermi energy. . . . .	96
5.9	A detailed view of the band structure of SmS at $a=10.40$ a.u. . . . .	97
5.10	A detailed view DOS about the Fermi energy at $a=10.40$ a.u. . . . .	98
5.11.	Variation of $d$ - $f$ overlap with volume as defined in the text. Total energy softens at larger volume but no indications of phase transition. The solid curve is the fit to the Murnaghan equation of state around the equilibrium volume and its extrapolation to large volume. The filled circles are for the overlap, the open circles are for the calculated total energy + 21650.75000 Ry. . . . .	99
6.1	Fully relativistic total energy - $E_{\min}$ for HgTe and HgSe respectively, where $E_{\min}$ is the minimum energy of Zinc-blende phase (-52884.14470 Ry for HgTe and -44155.92946 Ry for HgSe respectively). $V_{\text{expt}}$ is the experimental equilibrium volume of 454.57 a.u. <sup>3</sup> for HgTe and 380.02 a.u. <sup>3</sup> for HgSe. . . . .	106



6.2	The volume dependence of the $c/a$ ratio for the high pressure $\beta$ -Sn structure. The $c/a$ ratio of HgTe decreases almost linearly with volume, while for HgSe, it is almost a constant. . . . .	112
6.3	Scalar relativistic band structure for ZnS structure HgTe and HgSe at equilibrium volume and 90% of equilibrium volume. Dashed lines denote doubly degenerate states. . . . .	113
6.4	Fully relativistic density of states of ZnS structured HgTe and HgSe. . . . .	115
6.5	Fully relativistic partial density of states of HgTe and HgSe at different volumes for the ZnS structure. . . . .	116
6.6	Scalar relativistic band structures of NaCl structure HgTe and HgSe. The dashed lines denote doubly degenerate states. The $d$ band width at X and L increases at higher pressure. . . . .	117
6.7	Densities of states of NaCl structured HgTe and HgSe calculated fully relativistically. . . . .	118
6.8	Fully relativistic partial density of states of HgTe and HgSe at different volumes for the NaCl structure. . . . .	119
6.9	Fully relativistic density of states for HgTe and HgSe in the $\beta$ -Sn structure. . . . .	122
6.10	Fully relativistic partial density of states of HgTe and HgSe in the $\beta$ -Sn structure. . . . .	123
6.11	Valence charge densities of HgTe and HgSe in a (110) plane at experimental equilibrium volume $V_{\text{expt}}$ and $0.90 V_{\text{expt}}$ . The charge density is given in units of $10^{-2} \text{ e/a.u.}^3$ ; adjacent contours are separated by 1 unit. . . . .	124
6.12	The valence charge densities of NaCl structure HgTe of a (100) plane. The units are in $10^{-2} \text{ e/a.u.}^3$ adjacent contours are separated by 1 unit. . . . .	125
7.1	(a) Crystal structure of the (111) face of face-centered-cubic Pd. Circles denote the atoms in A layers; squares denote atoms in B layers; triangles denote	

	atoms in C layers. The length of $\bar{a}$ and $\bar{b}$ are $a/2^{1/3}$ , where a is cubic edge length. The distance between successive layers is $a/3^{1/3}$ . (b) The two-dimensional reciprocal lattice for fcc (111) face. . . . .	130
7.2	Scalar relativistic band structure of Pd at the experimental lattice constant ( $a=3.887\text{\AA}$ ). . . . .	133
7.3	Fully relativistic density of states of Pd at the experimental lattice constant, which agrees well with the previous calculations. . . . .	134
7.4	Total energy versus volume for bulk Pd. The lower two curves are the scalar and fully relativistic results, which have a larger basis set cutoff $R_{mt,max}=8.8$ . Upper curve is the scalar relativistic result and with a smaller basis set cutoff $R_{mt,max}=8.0$ , which converges reasonably well compared to that of the larger basis set. . . . .	135
7.5	The total valence charge density is shown on the $(\bar{1}10)$ plane cutting the Pd(111) surface. The charge density at the second layer already resembles the bulk density. The adjacent contour is separated by $\rho(n+1)/\rho(n)=1.272$ , and in units of $10^{-2} e/a.u.^3$ . . . . .	138
7.6	Total energy vs the top layer spacing (relative to the ideal experimental bulk spacing). The total energy minimum falls at -1%. . . . .	139
7.7	Local density of states (LDOS) for Pd(111) at the surface (S), S-1, S-2, and the center layer. The LDOS in the center layer resembles the bulk density of state (Fig. 7.3). The LDOS difference between the center and the surface layer reveals that the LDOS enhancement below the Fermi energy is at the price of the LDOS at the bottom of the d bands. . . . .	144
7.8	Surface states at $\bar{\Gamma}$ (a) at -5.1 eV, (b) at -2.4 eV (doubly degenerate), (c) at -0.2 eV, and (d) at 1.1 eV. See Fig. 7.5 for units. . . . .	145
7.9	Surface states at $\bar{K}$ (a) at -3.4 eV, (b) at -2.3 eV (doubly degenerate), and (c) at	

	-1.3 eV. See Fig. 7.5 for units. . . . .	146
7.10	Surface states at $\bar{M}$ (a) at -4.5 and (b) at 0.3 eV. See Fig. 7.5 for units. . . . .	147

## ABSTRACT

The local density approximation (LDA) has been proved to be a powerful starting point for calculating electronic and structural properties for many real materials. We have studied the effects of particular forms of exchange-correlation potentials (the  $X_\alpha$  and Hedin-Lundqvist form) upon the structural properties for the 3d Ti and 4d Zr using a highly accurate linearized augmented plane wave (LAPW) method. The calculated equilibrium volumes differ by 6-8% for these two forms (with  $X_\alpha$  results in better agreement with experiment) with proportional differences in other structural properties, which we take to be an indication of the intrinsic reliability of the LDA. Considerable sensitivity in the calculated structural properties to the particular exchange-correlation potential (the  $X_\alpha$ , Wigner, and Hedin-Lundqvist) was also found for the fcc and the high temperature bcc La. The calculation on SmS reveals that the LDA is inadequate for this very localized 4f electron system, while the LDA works fairly well for the chemically similar material LaS. For HgTe and HgSe, the fully occupied 5d electrons in Hg has been found to be important in determining the structural properties through the Hg d - chalcogen p interactions, however this p-d hybridization appears to be relatively unchanged through the various pressure induced phase transitions. We calculated the total energy of the seven layer slabs of Pd(111) surface as a function of the top layer spacing, the relaxation is found to be very small (<1%).

**LOCAL DENSITY APPROXIMATION STUDY OF  
TRANSITION AND f-ELECTRON MATERIALS**

## Chapter I

### FOREWORD

#### 1.1 PURPOSES

One of the exciting advances in the field of electronic structure theory in the last decade has been the development and implementation of accurate methods for predicting the ground state electronic and structural properties of bulk solids and surfaces using the local-density-functional approximation (LDA) (Hoh64, Koh65). In order to determine the ground state structure, e.g., lattice constant, bulk modulus, cohesive energy, phonon frequency, and heat of formation of a particular real or novel material, it is essential to accurately calculate the total energy of the system. The accuracy requirement for total energy is extremely high, since we are normally interested in total-energy difference related properties, a subset of those are listed above. The total-energy is the functional of the electronic charge density. Therefore, the accurate total-energy depends critically on the adequate convergence of the wave function and energy eigenvalues in the process of solving the self-consistent single particle Kohn-Sham equations (Koh65). The Kohn-Sham equations must be solved by iteration. Hence, computationally, it is extremely demanding.

With the development of efficient computational schemes, such as the linearized method of Andersen(And75), and combined with the ever increasing powers of modern supercomputers, it is feasible and possible to predict the electronic and structural properties of many real materials with the LDA based methods. There has been many successful applications of LDA based calculations. The calculated values are, in general, within a few percent of the experimental values for properties such as lattice constants, cohesive energies, bulk moduli, and phonon frequencies(Mor78,Dev85). The accurate evaluation of the total energy also enables us to predict the equilibrium phase, to investigate pressure induced phase transitions(Fro83), and to probe the atomic geometries and adsorption site of surfaces(Tom86,-Sin88). It is rather remarkable, since the only input to these calculations are the atomic numbers and crystallographic information of a particular material.

The local density approximation (LDA) is based on the exact density functional theory of Hohenberg and Kohn (Hoh64). Kohn and Sham (Koh65) further prove that it is possible to set up an effective one electron Schrödinger-like equation, the so called Kohn-Sham equation. The main difficulty to the realistic calculation is the unknown exchange-correlation (XC) energy. The LDA approximates the XC energy, which depends on all the other electrons effects, with the local uniform electron XC value. The LDA is easy

to implement for band structure calculation and has been very successful. The approximate local XC energy is obtained from homogeneous electron data, and is believed to give similar results for solids. However, there has been very few studies of the effects of the different commonly used XC energies upon the structural and cohesive properties. To this end, we have examined the effects upon the structural and cohesive properties for the IVA transition metals titanium (3d) and zirconium (4d) using two different XC energies, i.e., the  $X_\alpha$  (Koh65) and Hedin-Lundqvist (Hed-75) forms. This will be covered in chapter IV. In chapter V, we will further investigate the properties of the IIIA metal lanthanum with three different XC energy forms, i.e., the  $X_\alpha$ , Wigner interpolation scheme (Wig34), and Hedin-Lundqvist forms.

The LDA is formally justified for a slowly varying charge density or a small change of charge density over an inverse of Fermi vector. Nevertheless, it has been successfully applied to atoms, localized d and f electron systems, and surfaces. However, there has been indications that the LDA is inadequate for some localized 4f systems, for example, the LDA based calculation (Min86) severely underestimates the lattice constant and overestimates the bulk modulus for  $\alpha$ -Ce, furthermore it failed to predict the experimentally observed localized ( $\alpha$ -Ce fcc) to delocalized ( $\beta$ -Ce fcc) isostructural phase transition. In chapter V we



will apply the LDA based linearized augmented plane wave (LAPW) method to the localized 4f-electron system, SmS, in which there is an experimentally observed isostructural phase transition (NaCl to NaCl) (Jay72), to see if the LDA is adequate for this system.

Chapter VI deals with the electronic structures of semimetallic compounds HgTe and HgSe, which exhibit a variety of phases under pressure. While in Chapter VII, we will study the electronic structure and surface relaxation of the Pd(111) surface, which has a rich surface states (resonances).

## 1.2 LOCAL DENSITY APPROXIMATION

In order to investigate the electronic properties of atoms, molecules, and condensed matter, one must solve a many-body Hamiltonian:

$$H = \sum_{i=1}^N \left[ -\frac{\hbar^2}{2m} \nabla^2 + V_{\text{ext}}(\vec{r}_i) \right] + \frac{1}{2} \sum_{i \neq j}^N \frac{e^2}{|\vec{r}_i - \vec{r}_j|} , \quad (1.1)$$

where  $V_{\text{ext}}$  is the external potential including the sum of potentials arising from nuclei or ion cores. It is impractical to seek exact solutions to this many-body Hamiltonian analytically or numerically, since  $N$  is of the order of  $10^{20}$  for a realistic electronic system like a bulk solid. There are a few methods which attempt to solve the Hamiltonian approximately for the ground state, the local density ap-

proximation (LDA) being one of them.

The LDA has become one of the most widely used approaches for calculations of the total energy and other ground state properties of matter at present time. The framework of the density functional method was laid down by Hohenberg, Kohn, and Sham (Hoh64, Koh65). They proved that the total energy of the exact ground state of the many-body quantum mechanical system is a unique functional of the charge density  $\rho(\vec{r})$  and the ground state energy functional is stationary with respect to variation in the charge density and takes on its minimum value at the true charge density. Since that time there have been many important contributions, e.g., the extension to spin density functional and analysis of the nature of the corrections in the excited states, which can be found in the review book "Theory of the Inhomogeneous Electron Gas" (Lun83).

The density functional method is in principle exact and provides an alternative way to treat the full many-body Hamiltonian. Therefore, one can establish rigorous expressions for other physical quantities, such as the force and the stress in the density functional formalism. It is the local approximations to the exact functional which are both simple to implement for realistic calculations and are remarkably accurate for a varieties of properties of the electronic system in normal states of matter, e.g., atoms, molecules, and condensed matter.

The total energy of the system can be written as

$$E[\rho] = T[\rho] + U[\rho] + \int V_{\text{ext}}(\vec{r}) \rho(\vec{r}) d\vec{r} + E_{\text{xc}}[\rho] \quad , \quad (1.2)$$

where  $T[\rho]$  is the kinetic energy of the non-interacting electrons of the same density  $\rho(\vec{r})$ ;  $U[\rho]$  gives the electron-electron Coulomb repulsion or Hartree energy;  $V_{\text{ext}}$  is the interaction with the external potential including the electron-nuclei interaction; and  $E_{\text{xc}}[\rho]$ , contains all the many body effects, is the so-called XC energy which is an universal functional of  $\rho$ .

The correct ground state charge density minimizes the total energy, i.e.,

$$\frac{\delta E}{\delta \rho} = 0 \quad , \quad (1.3)$$

at physical  $\rho(\vec{r})$ . Therefore, the problem of finding the ground state energy is reduced to solving a set of effective one electron equations with a local potential, the so-called Kohn-Sham (Koh65) equations (in atomic units):

$$(-\nabla^2 + V(\vec{r}))\psi_i(\vec{r}) = \epsilon_i \psi_i(\vec{r}) \quad (1.4)$$

$$V(\vec{r}) = V_{\text{ext}}(\vec{r}) + V_{\text{H}}(\vec{r}) + \mu_{\text{xc}}[\rho] \quad . \quad (1.5)$$

From now on everything will be expressed in atomic units ( $m=\frac{1}{2}$ ,  $e^2=2$ ,  $\hbar=1$ , length in Bohr radii, and energy in Rydbergs) except when explicitly stated otherwise. The XC part of the effective potential is given by  $\mu_{\text{xc}} = \delta E_{\text{xc}}/\delta \rho$  and the density is obtained from the one particle wavefunctions

$$\rho(\vec{r}) = \sum_{i=1}^N |\psi_i(\vec{r})|^2 \quad (1.6)$$

where  $N$  is the number of electrons in the system.

This formalism reduces the many body problem to an effective single-particle problem which in principle gives the exact ground state energy. However, the functional form of the XC functional  $E_{xc}$  remains unknown. The most widely used approach is the LDA. For a sufficiently slowly varying charge density, or  $\rho(\vec{r})$  does not change appreciably over a distance corresponding to an inverse Fermi wave vector:

$$E_{xc}^{LDA} = \int d\vec{r} \rho(\vec{r}) \epsilon_{xc}^{hom}(\rho(\vec{r})) \quad (1.7)$$

where  $\epsilon_{xc}^{hom}(\rho)$  is the XC energy density of the homogeneous electron gas of density  $\rho$ . The XC potential of the total energy in the local density approximation can be accumulated additively from each portion of an inhomogeneous system gas as if it were locally homogeneous. The XC potential has the following form,

$$\mu_{xc}(\rho) = \frac{\delta(\epsilon_{xc}(\rho)\rho)}{\delta\rho} \quad (1.8)$$

Equations (1.4)-(1.6) define a self-consistent problem since each  $\psi_i$  is a solution of a single-particle Schrödinger equation in which the potential is a function of all the occupied wavefunctions  $\psi_i(\vec{r})$ . Martin(Mar85) summarizes the six essential steps for solving the self-consistent field

equations:

- 1) Choice of the function  $\epsilon_{xc}(\rho)$ ,
- 2) fixing the positions of nuclei and the interaction potential  $V_{ext}$ ,
- 3) solution of the differential equation (1.4) for a given potential  $V(\vec{r})$ ,
- 4) summation over filled states to find  $\rho(\vec{r})$  and a new  $V(\vec{r})$ ,
- 5) iteration to arrive at self-consistency,
- 6) optional evaluation of the total energy, force, and stress.

Although the exact function  $\epsilon_{xc}(\rho)$  is still unknown, there are a few commonly used approximations for the XC potential, which were obtained from the electron gas data, for example the  $X_\alpha$  XC potential(Koh65),

$$\epsilon_{xc}(\rho) = \alpha \{-3/4\pi [3\pi^2 \rho(\vec{r})]^{1/3}\} \quad , \quad (1.9)$$

where  $\alpha$  is chosen between 2/3 to 1, and the Wigner interpolation formula(Wig34),

$$\epsilon_{xc}(\rho) = -0.738\rho^{1/3} \left[ 1 + \frac{0.959}{1 + 12.57\rho^{1/3}} \right] \quad , \quad (1.10)$$

which was chosen to reproduce properly the high-density (uncorrelated) limit and the low-density Wigner crystal energy. Other widely used forms are the Hedin-Lundqvist form(Hed71) and its spin-polarized generalization the von

Barth-Hedin form(Bar72), and many other(Gun74,Cep78,Vos80). An important point is that the different forms for  $\epsilon_{xc}$  in current use are very similar. There has been only limited investigation of the consequences of the effects of the different functions upon the solid state properties(McM81).

The LDA has been proved to be a very accurate approach to the ground state properties of the electronic systems, owing largely to its computational simplicity of the LDA XC functional. The LDA has been successfully applied to atoms and molecules(Gun80), metals(Mor78), semiconductor(Yin82), surfaces(Lan73,App76,Wim85), and defects(Bar84). Generally, the lattice constants and phonon frequencies are predicted within  $\sim 1\%$  and the bulk moduli within  $\sim 10\%$  of experiment. The cohesive energy is generally overestimated, a result usually attributed to the predicted underbinding of atom by the LDA.

Despite the apparent successes of the LDA, there are still many problems associated with it. The LDA incorrectly leads to the exponential decay form of the potential instead of the  $r^{-1}$  form for large  $r$  in atoms and  $z^{-1}$  form far from the surfaces. The  $\epsilon_i$  from the Kohn-Sham equations are interpreted as quasiparticle energies, agreement with experiment is less satisfactory. The relative positions of valence band energies for bulk materials agree well with photo-emission experiments. However, the LDA gap given by the eigenvalue difference between the valence-band maximum

and the conduction-band minimum are usually underestimated by 30-50% (Ihm81, Ham79, Hea80) for semiconductors and insulators, even though the topology of the conduction band agree well with experiment. The LDA also tends to overestimate the  $f$  bonding for mixed-valence systems (Nor87); as a result, the LDA-based total-energy calculations predict contracted lattice constants and larger bulk moduli.

### 1.3 CORRECTIONS BEYOND THE LDA

The success of the the LDA can be understood by the XC hole (Gun76). The hole is a consequence of the exchange and Coulomb interactions which cause a depletion of charge in the vicinity of each electron. The sum rule states that the total amount of displaced charge corresponds to one unit of charge for all space, which is satisfied by the LDA. However, the LDA misrepresent the shape and position of an XC hole, which is spherical and is always centered on the electrons in investigation. Fortunately, the total-energy of the system depends only on the spherical average of the XC hole, making it insensitive to the XC hole shape. A systematic cancellation of errors also occurs when sum rules is satisfied.

There have been many attempts to go beyond the limitations of the LDA. The earliest and seemingly natural attempt was a correction using a gradient expansion. The application of the lowest order corrections to inhomogeneous

systems, however, have not been encouraging(Lun83). The LDA is formally justified when the gradient of the density is small or when the deviations from the average density are small, which has been thought to be violated over much of the unit cell in many solids where the LDA nevertheless works well. Langreth and Mehl(Lan83) has argued that the LDA remains a good approximation well beyond the range of uniformity for which the lowest order gradient term gives the dominant correction. The weighted density approximation (WDA) (Alo78,Gun79), which generalizes the LDA by evaluating the XC hole for a weighted density surrounding the point  $\vec{r}$ , gives the correct limit  $V_{XC} \sim -r^{-1}$  for large  $r$  in atom and  $V_{XC} \sim -z^{-1}$  far from surface. However, the improvement of the WDA XC energies over that of the LDA is very modest. Other approaches to go beyond the LDA, such as the self-interaction correction to the LDA (SIC-LDA), has improved the description of the tightly bound core electrons and thus improved the binding energies(Per81). There are still many questions to be answered in density functional theory and research in this area remains active and will bear fruitful results.



## Chapter II

### LINEARIZED AUGMENTED PLANE WAVE METHOD

#### 2.1 INTRODUCTION

The linearized augmented plane wave (LAPW) method, which is based on the LDA, has proved to be a highly accurate method. Slater(Sla37) formulated the original augmented plane wave (APW) method. The APW method didn't come into general use until around 1960, is described in detail by Loucks(Lou67). The linearized version of the APW method, i.e., the LAPW method, was based on the linearized method of Andersen(And75) and was first implemented by Koelling and Arbman(Koe75). The LAPW basis functions include not only the radial solution but its energy derivative as well. It eliminates the two major difficulties (Koe75) associated with the standard APW method, i.e., energy dependence of the secular equation resulting from the nonlinear parameters used in setting up the radial solutions inside the muffin-tin spheres and the singular behavior of the secular equation which occurs when a node of the radial solution falls at the muffin-tin-sphere boundary. The LAPW method also eliminates one minor problem of the APW method, that is the discontinuities of the slope of basis function across the

muffin-tin-sphere boundary. Furthermore, it also facilitates the inclusion of the non-muffin-tin part of the potential. A fairly detailed description of the LAPW method is given by Wei (Wei85).

A review of the general potential LAPW method is given below. First, we set up the basis functions.

## 2.2 BASIS FUNCTIONS

In order to solve the Kohn-Sham equation with the LAPW method, space is partitioned into two distinct parts: (I) the muffin-tin spheres (MT) which are centered at the fixed nuclear sites and (II) the remaining interstitial region. The variational trial wave function is expanded as

$$\psi_{\vec{k}}^n(\vec{r}) = \sum_{\vec{G}} C_{\vec{G}}^n \phi_{\vec{k}+\vec{G}}(\vec{r}) \quad (2.1)$$

$$\vec{K} = \vec{k} + \vec{G} \quad , \quad (2.2)$$

where  $n$  is the energy band index,  $\vec{G}$  specifies a particular reciprocal lattice vector,  $C_{\vec{G}}^n$  is the variational coefficient, and  $\phi_{\vec{k}}(\vec{r})$  is the basis function, which can be expressed in the following form,

$$\phi_{\vec{k}}(\vec{r}) = \begin{cases} \Omega^{-1/2} e^{i\vec{k} \cdot \vec{r}} & \vec{r} \in \text{int.} \\ \sum_{lm} [A_{lm}^{\alpha} u_l^{\alpha}(E_l^{\alpha}, r_{\alpha}) + B_{lm}^{\alpha} \hat{u}_l^{\alpha}(E_l^{\alpha}, r_{\alpha})] Y_{lm}(\hat{r}_{\alpha}) & |\vec{r} - \vec{r}_{\alpha}| \leq R_{\alpha} \end{cases} \quad (2.3)$$

where  $\Omega$  is the volume of the unit cell,  $u^\alpha$  and  $\dot{u}^\alpha$  are radial solutions to the Schrödinger (or Dirac) equation at fixed energy  $E$  and its energy derivative, respectively;  $\vec{r}_\alpha = \vec{r} - \vec{r}_\alpha$ ,  $\vec{r}_\alpha$  is the position of the nucleus  $\alpha$ ;  $l, m$  are the angular momentum quantum numbers; coefficients  $A_{lm}, B_{lm}$  are determined by matching the basis functions at the muffin-tin sphere surface to the plane wave basis functions. The plane wave basis functions in the interstitial region are an appropriate choice since the potential in that region is generally flat.

Koelling and Arbman (Koe75) describe how to construct the radial solution and its energy derivative, which is the solution of the following equations for fixed energy parameter:

$$h_l u_l - E u_l = 0 \quad (2.4a)$$

$$h_l = -\frac{1}{r} \frac{d^2}{dr^2} r + \frac{l(l+1)}{r^2} + V(r) \quad (2.4b)$$

by a straightforward differentiation from equation (2.4a), one obtains the differentiation equation for  $\dot{u}_l$ :

$$h_l \dot{u}_l - E \dot{u}_l = \dot{u}_l \quad (2.5)$$

The radial solutions are normalized inside the muffin-tin sphere (with radius  $R$ ), which are convenient in setting up the Hamiltonian and overlap matrices:

$$\int_0^R r^2 u^2 dr = 1 \quad , \quad (2.6)$$

The  $u_l$  and  $\dot{u}_l$  are orthogonal, which can be seen by differentiating the normalization condition with  $E$ ,

$$\int_0^R r^2 u_l \dot{u}_l dr = 0 \quad . \quad (2.7)$$

We may also notice that the normalization constant for  $u_l$  is not in general equal to unity,

$$N_l = \int_0^R r^2 \dot{u}_l^2 dr \quad . \quad (2.8)$$

The actual  $u_l$  and  $\dot{u}_l$  used in calculations are the large component of the radial solutions of the so-called "j-weighted-averaged" Dirac equation as formulated by Koelling and Harmon (Koe77), in which all the scalar relativistic effects are included.

By expanding the plane wave in the spherical Bessel functions and spherical harmonics (Lou67), and combining with an important approximation, we can obtain elegant expressions for  $A_{lm}$  and  $B_{lm}$ ,

$$e^{i\vec{k}\cdot\vec{r}} = 4\pi e^{i\vec{k}\cdot\vec{r}_\alpha} \sum_{lm} i^l j_l(kr_\alpha) Y_{lm}^*(\hat{K}) Y_{lm}(\hat{r}_\alpha) \quad , \quad (2.9)$$

$$R_\alpha^2 \left[ u u' - u u' \right]_{R_\alpha} = 1 \quad , \quad (2.10)$$

where  $j_l(x)$  is the spherical Bessel function of order  $l$  and  $Y_{lm}$  are the usual spherical harmonics. The approximation (2.10) was shown to be excellent by Krakauer *et. al*(Kra79),  $A_{lm}$  and  $B_{lm}$  is then given below:

$$A_{lm}^\alpha(\vec{K}) = F_{lm}^\alpha(\vec{K}) [j_l'(KR_\alpha) u_l^\alpha(R_\alpha) - j_l(KR_\alpha) u_l^{\alpha'}(R_\alpha)] \quad (2.11a)$$

$$B_{lm}^\alpha(\vec{K}) = F_{lm}^\alpha(\vec{K}) [j_l(KR_\alpha) u_l^{\alpha'}(R_\alpha) - j_l'(KR_\alpha) u_l^\alpha(R_\alpha)] \quad (2.11b)$$

$$F_{lm}^\alpha(\vec{K}) = i^l \frac{4\pi R_\alpha^2}{\Omega^{\frac{1}{2}}} e^{i\vec{K} \cdot \vec{r}_\alpha} Y_{lm}^*[\vec{M}\vec{K}] \quad , \quad (2.11c)$$

where prime ' denotes  $d/dr$ . Next we obtain the potential.

### 2.3 POTENTIAL

In the standard APW method, the potential was usually approximated by a spherical muffin-tin potential (Lou67). However, there is no shape restricted approximation in the LAPW method. Both the spherical muffin-tin and non-spherical potential are included in the muffin-tin spheres; in the interstitial region, potential is expanded in a Fourier series. The potential is the sum of the Coulomb potential and an XC potential. The Coulomb potential is obtained by solving the Poisson's equation(Jac75),

$$\nabla^2 V(\vec{r}) = -8\pi\rho(\vec{r}) \quad , \quad (2.12)$$

where  $V(\vec{r})$  is the potential to be determined and  $\rho(\vec{r})$  is the given charge density which can be written in the following form

$$\rho(\vec{r}) = \begin{cases} \sum_{\mu} \rho_{\mu}^{\alpha}(\mathbf{r}_{\alpha}) K_{\mu}^{\alpha}(\vec{r}_{\alpha}) & r_{\alpha} \leq R_{\alpha} \\ \sum_s \rho_s \phi_s(\vec{r}) & \vec{r} \in \text{int.} \end{cases} \quad (2.13)$$

where the  $K_{\mu}^{\alpha}(\vec{r}_{\alpha})$  are the lattice harmonics, which are just linear combinations of spherical harmonics and possess all the point symmetry properties of the crystal;  $\phi_s$  are the star functions, which are the symmetrized plane waves.

Weinert(Wei81) has formulated an efficient and elegant way to solve the Poisson's equation, which is based on the concepts of multipole potential and the Dirichlet problem for a sphere in which all contributions are treated equivalently. The potential at a point outside the muffin-tin sphere due to the charge distribution inside sphere is given by the multipole expansion (Jac75)

$$V(\mathbf{r}) = \sum_{l=0}^{\infty} \sum_{m=-l}^l \frac{4\pi}{2l+1} q_{lm} \frac{Y_{lm}(\hat{r})}{r^{l+1}} \quad (2.14)$$

$$q_{lm} = \int_S Y_{lm}^*(\hat{r}) r^l \rho(\vec{r}) d\vec{r} \quad (2.15)$$

the potential outside sphere depends on the charge density only through multipole moments; the real charge density is actually immaterial. Therefore, we have the freedom to choose a more convenient pseudocharge density. In general, the real charge density inside the muffin-tin sphere has a

slowly convergent Fourier expansion due to the large oscillations near the nuclei, which can be replaced by a smoothly varying pseudocharge density such that it has a rapidly convergent Fourier expansion. However, the charge density in the interstitial region varies smoothly and has a rapidly convergent Fourier expansion. It is easier to solve the Poisson's equation in the interstitial region first, then obtain the Coulomb potential inside the muffin-tin spheres by solving the boundary value problem for a sphere.

We define the pseudocharge density as

$$\begin{aligned} \bar{\rho}(\vec{r}) &= \sum_s \rho_s \phi_s(\vec{r}) + \sum_{\alpha\mu} \Delta\bar{\rho}_\mu^\alpha(r_\alpha) K_\mu^\alpha(\vec{r}_\alpha) \theta(\vec{r}_\alpha) \\ &= \sum_s \bar{\rho}_s \phi_s(\vec{r}) \end{aligned} \quad , \quad (2.16)$$

where  $\theta(\vec{r}_\alpha)$  is the step function defined as

$$\theta(\vec{r}_\alpha) = \begin{cases} 1 & r_\alpha \leq R_\alpha \\ 0 & \vec{r} \in \text{int.} \end{cases} \quad . \quad (2.17)$$

The interstitial charge density is extended to the muffin-tin spheres.  $\Delta\bar{\rho}_\mu^\alpha(r_\alpha)$  is chosen such that its multipole moments are the difference of the original and the extended interstitial plane wave moments. The difference charge density has the polynomial form,

$$\Delta\bar{\rho}_{lm}(r_\alpha) = Q_{lm} \frac{r^l}{R_\alpha^{2l+3}} \left[ 1 - \frac{r^2}{R_\alpha^2} \right]^N \quad , \quad (2.18)$$

where  $N$  is a convergence parameter which is chosen such that the first zero of the spherical Jacob function  $j_{l+N+1}(x)$  is approximately equal to  $(GR)_{\max}$ ; for a fixed  $l$  value,  $N$  will be chosen to give the best convergence possible of the pseudocharge density and the interstitial potential. The parameter  $Q_{lm}$  is determined by requiring that the moments are equal to that of the difference charge. The expansion coefficients  $\tilde{\rho}_s$  for the pseudocharge density

$$\tilde{\rho}_s = \rho_s + \frac{4\pi}{\Omega} \sum_n \text{neq}(n) \sum_{lm} (-i)^l \Delta \tilde{q}_{lm}^\alpha \frac{(2l+2N+3)!!}{R_\alpha^2 (2l+1)!!} \times \frac{j_{N+l+1}(G_s R_\alpha)}{(G_s R_\alpha)^{N+1}} \sum_s m_s \text{PHS}^*(\vec{G}_j^s) e^{-i\vec{G} \cdot \vec{r}_\alpha} Y_{lm}(\vec{G}_j^s), \quad (2.19)$$

where  $m_s$  is the number of members in the star  $\vec{G}_s$ ,  $\text{neq}(n)$  is the number of type  $n$  atoms in the unit cell, and  $\text{PHS}(\vec{G}_j^s)$  is the phase factor of reciprocal vector  $\vec{G}_j^s$ . In the same star  $\vec{G}_s$ , all the members have the same magnitude of  $G_s$ . We can then obtain the interstitial Coulomb potential easily

$$V_c(\vec{r}) = \sum_s \frac{8\pi \tilde{\rho}_s}{G_s^2} \phi_s(\vec{r}), \quad (2.20)$$

which is exact in the interstitial region and on the muffin-tin sphere surface. Consequently, we can obtain the potential inside the muffin-tin sphere as well by the standard Green's function method, which is given below



$$V_c(\vec{r}) = \int \rho(\vec{r}') G(\vec{r}_\alpha, \vec{r}') d\vec{r}' - (4\pi)^{-1} \oint_S V(\vec{R}_\alpha) \frac{\partial G}{\partial n} dS \quad (2.21a)$$

$$G(\vec{r}_\alpha, \vec{r}) = 4\pi \sum_{lm} \frac{Y_{lm}^*(\vec{r}) Y_{lm}(\vec{r}_\alpha)}{2l+1} \frac{r_{<}^l}{r_{>}^{l+1}} \left[ 1 - \left( \frac{r_{>}}{R_\alpha} \right)^{2l+1} \right] \quad (2.21b)$$

$$\frac{\partial G}{\partial n} = \frac{\partial G}{\partial r} \Big|_{r=R_\alpha} = -\frac{4\pi}{R_\alpha} \sum_{lm} \left( \frac{r}{R_\alpha} \right)^l Y_{lm}^*(\vec{r}) Y_{lm}(\vec{r}_\alpha) \quad (2.21c)$$

This method of obtaining Coulomb potential has been proven (Wei81) to be very accurate and efficient. There are only absolutely and uniformly convergent reciprocal space sums. The convergence properties of the summations are easily monitored by checking the  $(GR)_{\max}$  and  $N_l$  values.

The total potential can be finally obtained by adding the Coulomb potential and the XC potential together. As in the case of charge density, the potential is also expanded in the lattice harmonics and star functions similar to the charge density expression eq. (2.13).

#### 2.4 HAMILTONIAN AND OVERLAP MATRICES

Applying the variational principle to each of  $C_{\vec{G}}^n$  yields the LAPW secular equations:

$$\sum_{\vec{G}'} [H_{\vec{G},\vec{G}'}(\vec{K}) - E_n(\vec{K}) O_{\vec{G},\vec{G}'}(\vec{K})] C_{\vec{G}'}^n(\vec{K}) = 0 \quad (2.22a)$$

$$H_{\vec{G},\vec{G}'}(\vec{K}) = \langle \Phi_{\vec{G}',\vec{K}}(\vec{r}) | H | \Phi_{\vec{G},\vec{K}}(\vec{r}) \rangle \quad (2.22b)$$

$$O_{\vec{G},\vec{G}'}(\vec{K}) = \langle \Phi_{\vec{G}',\vec{K}}(\vec{r}) | \Phi_{\vec{G},\vec{K}}(\vec{r}) \rangle \quad (2.22c)$$

where  $H_{\vec{g},\vec{g}}(\vec{k})$  and  $O_{\vec{g},\vec{g}}(\vec{k})$  are Hamiltonian and overlap matrix elements, respectively. Equation (2.22a) can be written in following form

$$HX = \epsilon OX \quad , \quad (2.23)$$

which can be solved with a standard approach. The Hamiltonian can be separated into three terms

$$H = H_{MT} + H_I + H_{NS} \quad , \quad (2.24)$$

where  $H_{MT}$  is due to the muffin-tin (spherical component) potential only,  $H_I$  comes from the actual interstitial potential, and  $H_{NS}$  is the non-spherical potential inside the muffin-tin spheres.

$$H_{MT} = \begin{cases} K_{op} + V_{MT}^{\alpha}(r_{\alpha}) & r_{\alpha} \leq R_{\alpha} \\ -\nabla^2 & \vec{r} \in \text{int.} \end{cases} \quad , \quad (2.25)$$

$$H_I = \begin{cases} 0 & r_{\alpha} \leq R_{\alpha} \\ \sum_{\vec{g}} V_{\vec{g}} e^{i\vec{g} \cdot \vec{r}} & \vec{r} \in \text{int.} \end{cases} \quad , \quad (2.26)$$

$$H_{NS} = \begin{cases} \sum_{\mu \neq 0} V_{\mu}^{\alpha}(r_{\alpha}) K_{\mu}^{\alpha}(\vec{r}_{\alpha}) & r_{\alpha} \leq R_{\alpha} \\ 0 & \vec{r} \in \text{int.} \end{cases} \quad , \quad (2.27)$$

where the kinetic energy operator  $K_{op}$  is

$$K_{op} = \begin{cases} -\nabla^2 & \text{nonrelativistically} \\ c\vec{\alpha} \cdot \vec{\beta} + mc^2(\beta-1) & \text{relativistically} \end{cases} \quad (2.28)$$

The Hamiltonian and overlap matrices can now be evaluated together with the basis functions and equations (2.9)-(2.11). The spin-orbit interaction can be included by a second variational procedure (Mac80, Pic81), which involves re-diagonalization of  $2M \times 2M$  matrices,  $M$  being the order of the number of occupied bands.

## 2.5 CHARGE DENSITY

Having solved the Kohn-Sham equation, the charge density can be constructed as

$$\rho(\vec{r}) = \sum_n \int |\psi_{n,\vec{k}}(\vec{r})|^2 d\vec{k} \quad , \quad (2.29)$$

where sum goes over all the occupied states and the reciprocal space integration runs over the first Brillouin zone. In practice, the integration over  $\vec{k}$  space can be further reduced to the wedge of the irreducible Brillouin zone by utilizing the symmetry properties of the crystal. The integration over  $\vec{k}$  must be approximated by summation over a set of discrete  $\vec{k}$  points, since we do not know the eigenfunctions analytically. The commonly used schemes are 1) uniformly distributed  $\vec{k}$ -points, 2) the tetrahedron method (Jep71, Sin75), and 3) the special  $\vec{k}$ -points method (Cha73, Mon76). The charge density can now be written as

$$\bar{\rho}(\vec{r}) = \sum_{n,\vec{k}} |\psi_{n,\vec{k}}(\vec{r})|^2 \omega_n(\vec{k}) \quad , \quad (2.30)$$

where  $\omega_n(\bar{k})$  is the weight function which depends on both the band index  $n$  and specific  $\bar{k}$ -point.

The symmetrization of charge density can be done by projecting onto lattice harmonics and 3D star functions in the muffin-tin spheres and interstitial region, respectively. These functions possess all the symmetry of the crystal and orthogonal to each other.

Self-consistency, is essential in obtaining reliable total energy and other electronic properties, must be accomplished iteratively. The most straightforward scheme, is the linear mixing method. The real output charge density  $\rho$  is the linear combination of the previous "input" charge density  $\rho_{in}$  and the "output" charge density  $\rho_{out}$ , i.e.,

$$\rho_{in}^{m+1} = \alpha \rho_{out}^m + (1-\alpha) \rho_{in}^m, \quad (2.31)$$

where  $\alpha$  is the mixing parameter which is usually chosen to be less than 0.5, and 0.1 to be common. The convergence rate for this simple method, which is more or less linearly convergent, is not always satisfactory in the problems like a surface or system with large number of atoms in the unit cell. There are other more sophisticated methods which speed up the convergence, for example the Broyden's method (-Bro65, Sin86), which uses the charge densities of at least two previous iterations. The applicability of Broyden's method to LAPW method and its rapid convergence has been demonstrated by Singh *et. al* (Sin86). The convergence process can be monitored by defining a parameter  $d$

$$d = [\int_{\Omega} |\rho_{\text{out}} - \rho_{\text{in}}|^2 / \Omega d\vec{r}]^{1/2}, \quad (2.32)$$

when  $d$  goes under  $10^{-5}$  electrons/a.u.<sup>3</sup>, the total energy of the system is usually converged to around  $10^{-5}$  Ry, in which self-consistency can be regarded achieved. Having reached the self-consistency, we can then evaluate the total energy, stress, force, and other properties of the system.

## 2.5 TOTAL ENERGY

The total energy of a condensed matter system is one of the most important physical quantities, through which one can examine related properties, such as phase stabilities, equilibrium structural properties (lattice constants, force constants), and electronic properties.

The LDA provides an elegant framework in which the total energy of the solid-state system can be obtained for any geometrical configuration of the nuclei. The main difficulty preventing an implementation of the total energy expression to an all electron method, arises from the cancellation between the very large kinetic and potential-energy contributions. The problem obviously becomes more severe for heavier atoms (d- and f-electron atoms), since the chemically inert core electrons are responsible for the largest part of the total energy. The total energy itself is of the order of tens of thousands of Rydbergs. For example, the total energy for Mercury atom using the Hedin-Lundqvist XC potential(Hed71) is -39301.836 Ry. However the

difference of total energy due to structural variation is of the order of mRy. The following table shows the precision requirements for calculating various properties of solids as summarized by Louie(Lou85),

Table 2.1

Precision requirement for various structural quantities.

Physical quantity	Precision requirement
Cohesive energy	0.01 Ry/atom
Lattice constant and bulk modulus	0.001 Ry/atom
Phonon frequencies	0.0001 Ry/atom

To avoid this large cancellation, one has to remove the core electron contributions as done in the pseudopotential approach(Ihm79). For the all-electron LAPW method, we use the approach developed by Weinert *et. al*(Wei82), in which high accuracy is retained by explicit cancellation of the Coulomb singularity in the kinetic and potential-energy terms arising from the nuclear charge.

The total energy of a solid state system within the LDA framework is given by a sum of kinetic, potential, and XC energy terms as given in the eq. (1.2). The kinetic and potential energy can be written as

$$T[\rho] = \sum_i \int \psi_i^*(\vec{r}) K_{op} \psi_i(\vec{r}) d\vec{r} \quad , \quad (2.33)$$

$$U[\rho] = \frac{1}{2} \left[ \int \frac{\rho(\vec{r})\rho(\vec{r}')}{|\vec{r}-\vec{r}'|} d\vec{r}d\vec{r}' - 2 \sum_{\alpha} \int \frac{\rho(\vec{r})}{|\vec{r}-\vec{r}_{\alpha}|} d\vec{r} + \sum_{\alpha \neq \beta} \frac{Z_{\alpha}Z_{\beta}}{|\vec{r}_{\beta}-\vec{r}_{\alpha}|} \right] \quad (2.34)$$

where summation over  $i$  includes both the band index and  $\vec{k}$  space,  $\psi_i$  are solutions of the Kohn-Sham equation (1.4) and (1.5), and the charge density  $\rho$  is defined as equation (2.30). The effective potential is the sum of the Coulomb potential and XC potential. The XC energy functional can be written in the LDA as in equation (1.7).

The kinetic energy part,  $T[\rho]$  per unit cell can also be written as

$$\begin{aligned} T[\rho] &= \sum_i \int \psi_i^*(\vec{r}) [\epsilon_i - V_{\text{eff}}(\vec{r})] \psi_i(\vec{r}) d\vec{r} \\ &= \sum_i \epsilon_i - \int V_C(\vec{r}) \rho(\vec{r}) d\vec{r} - \int \mu_{\text{XC}}(\vec{r}) \rho(\vec{r}) d\vec{r} \quad , \end{aligned} \quad (2.35)$$

while the potential energy per unit cell can be recombined as

$$U[\rho] = \frac{1}{2} \left[ \int V_C(\vec{r}) \rho(\vec{r}) d\vec{r} - \sum_{\alpha} Z_{\alpha} V_M(\vec{r}_{\alpha}) \right] \quad , \quad (2.36)$$

where  $V_C(\vec{r})$  is the Coulomb potential at  $\vec{r}$

$$V_C(\vec{r}) = \int \frac{\rho(\vec{r}')}{|\vec{r}-\vec{r}'|} d\vec{r}' - \sum_{\alpha} \frac{Z_{\alpha}}{|\vec{r}-\vec{r}_{\alpha}|} \quad , \quad (2.37)$$

and  $V_M(\vec{r})$  is a generalized Madelung potential, i.e., the Coulomb potential at  $\vec{r}$  due to all charges in the crystal except for the nuclear charge at this site

$$V_M(\vec{r}_\alpha) = \int \frac{\rho(\vec{r})}{|\vec{r} - \vec{r}_\alpha|} d\vec{r} - \sum_{\beta \neq \alpha} \frac{Z_\alpha}{|\vec{r}_\beta - \vec{r}_\alpha|} \quad (2.38)$$

which can be obtained the same way as the Coulomb potential is obtained, i.e., solve the Dirichlet boundary-value problem for a sphere with electronic density and  $V_{MT}(R_\alpha)$ . Only the spherical part ( $l=0$ ) is needed, since we want the potential at the center of sphere,

$$\begin{aligned} V_M(\vec{r}_\alpha) &= R_\alpha^{-1} [R_\alpha V_{MT}^\alpha(R_\alpha) + Z_\alpha - Q_{MT}^\alpha] + (4\pi)^{1/2} \int_0^{R_\alpha} \rho_{00}(r) r dr \\ &= R_\alpha^{-1} [R_\alpha V_{MT}^\alpha(R_\alpha) + Z_\alpha - Q_{MT}^\alpha] + \left\langle \frac{\rho(\vec{r})}{r} \right\rangle_\alpha \end{aligned} \quad (2.39)$$

Thus we can write the total energy per unit cell into following form,

$$E[\rho] = \sum_i \epsilon_i - \frac{1}{2} \int (V_C(\vec{r}) + 2[\mu_{XC}(\vec{r}) - \epsilon_{XC}(\vec{r})]) \rho(\vec{r}) d\vec{r} - \frac{1}{2} \sum_\alpha Z_\alpha V_M(\vec{r}_\alpha) \quad (2.40)$$

where  $Q_{MT}^\alpha$  is the number of electrons inside the sphere  $\alpha$ . The combined terms in the large parentheses explicitly cancels the Coulomb singularities at the nuclei. The total energy can be finally written in a form(Wei85) which is suitable for the LAPW method, i.e., the lattice harmonics expression inside the muffin-tin spheres and star functions in the interstitial region,

$$E[\rho] = \sum_i \epsilon_i - \frac{1}{2} \sum_\alpha Z_\alpha R_\alpha^{-1} [2(Z_\alpha - Q_{MT}^\alpha) + R_\alpha V_{MT}^\alpha(R_\alpha)]$$



$$\begin{aligned}
& - \frac{1}{2} \int_V \rho(\vec{r}) \chi(\vec{r}) d\vec{r} - \frac{1}{2} \sum_{\alpha\mu} \int_0^{R_\alpha} \chi_\mu(r_\alpha) \rho_\mu(r_\alpha) r_\alpha^2 dr_\alpha \\
& - \frac{1}{2} \sum_{\alpha} \int_0^{R_\alpha} [2Z_\alpha \sigma(r_\alpha) r_\alpha^{-1} + \chi_{HT}(r_\alpha) \sigma(r_\alpha)] dr_\alpha \quad , \quad (2.41)
\end{aligned}$$

where  $\chi(\vec{r})$  defined as

$$\chi(\vec{r}) = V_c(\vec{r}) + 2[\mu_{XC}(\vec{r}) - \epsilon_{XC}(\vec{r})] \quad , \quad (2.42)$$

and  $\sigma(r_\alpha) = 4\pi r_\alpha^2 \rho(r_\alpha)$ . There are other physical quantities which can be obtained directly from the self-consistent charge density, eigenvalues, and eigenfunctions: e.g., the pressure and force of the system. In summary, the LAPW method or other all electron LDA based band structure calculations can be illustrated in the following simplified flow diagram:

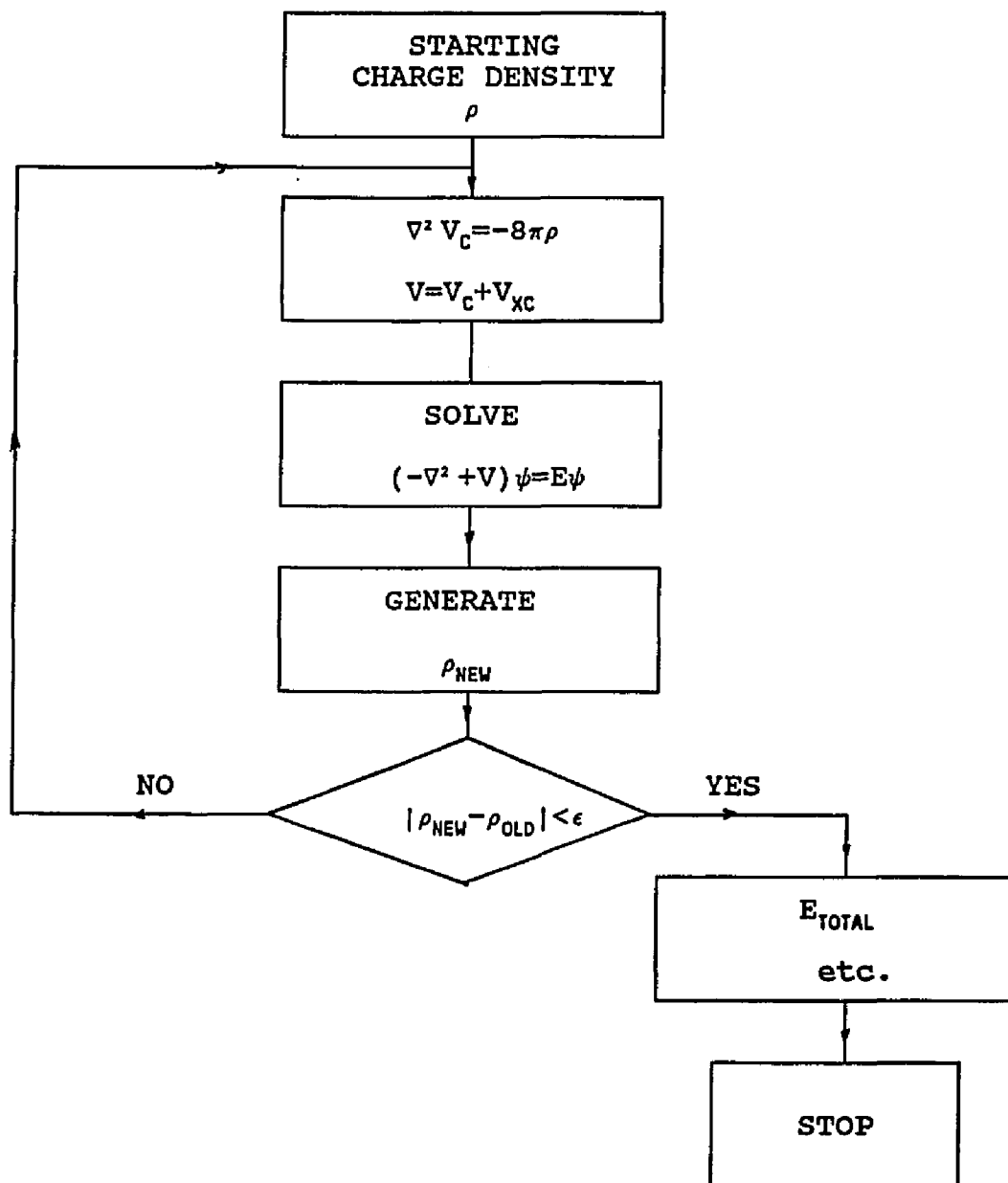


Fig. 2.1 Flow diagram of the LAPW method.

## Chapter III

### Titanium and Zirconium

#### 3.1 INTRODUCTION

In recent years the local density functional approximation has, by its numerous successful applications, proved to be a powerful starting point for the calculation of structural and electronic properties of solids and surfaces. There have, however, been relatively few LDA based calculations of the ground state properties of elements at the beginnings of the transition metal series, perhaps because of the fact that these elements (Sc,Ti,V,Zr,La,Hf) crystallize in the hcp structure. Here, we report structural and electronic properties of hcp titanium and zirconium calculated within the LDA using a highly accurate self-consistent general potential LAPW method. In order to assess the reliability of the LDA for these materials we carried out parallel calculations using two exchange-correlation (XC) potentials namely the widely used Hedin-Lundqvist form (Hed71) and the exchange-only  $X_\alpha$  ( $\alpha=2/3$ ) form(Koh65). We find that these different local approximations yield equilibrium volumes differing by about 6% with corresponding differences in other structural properties. We take these

difference to be an indication of the intrinsic reliability of the LDA.

There have been a few calculations of the band structures and the densities of states of hcp Ti(Alt58a,Mat64,-Hyg70,Jep75a, Fei79) and Zr(Alt58b,Lou67b,Jep75b,Iya76,-Cha84). Morruzi *et al.*(Mor78) have calculated the structural and the electronic properties of Ti and Zr assuming a fcc structure instead of the actual hcp structure. Jepsen and coworkers(Jep75a, Jep75b) have elucidated the general electronic structures of the hcp transition metals and their dependence on atomic number using a non-self-consistent linear-muffin-tin-orbital (LMTO) method.

### 3.2 DETAILS OF CALCULATION

The LAPW method has been discussed in detail in Chapter 2, here, we will only present a brief summary of the details pertinent to the present calculation.

The MT radius is chosen in order to have nearly touching spheres at the smallest lattice parameter; the MT radii used in the present calculations were 2.59 a.u. for Ti and 2.84 a.u. for Zr. A basis set of about 110 LAPWs (And75) was used for both Ti and Zr, corresponding to  $R_{MT}K_{max}=8.0$  or corresponding to cut off energy of 9.54 Ry and 7.93 Ry for Ti and Zr respectively. Inside the MT spheres, the LAPW basis functions were expanded up to  $l=8$ , as were the potentials and charge densities.

The unit cell for the hcp crystal structure and the Brillouin zone are shown in Fig. 3.1. The space group for hexagonal-close-packed is non-symmorphic  $D_{6h}^4$ ; there are 24 operations and half of them with a shift of  $\vec{r}=(1/2,2/3,1/3)$ . It is convenient to set the origin at midway between the two representative atoms, which is the inversion center; thus we will have a real Hamiltonian matrix. The bands at point  $\vec{k}=(k_x, k_y, \pi/c)$  are all doubly degenerate which arise from time-reversal symmetry.

The Brillouin zone summations were done using 40 special  $\vec{k}$ -point(Mon76) for both Ti and Zr with an artificial Fermi-Dirac distribution of width  $kT=2$  mRy, which stabilizes and speeds the convergence process. Self-consistency was considered achieved when the total energy was stable to within 0.01 mRy.

The densities of states (DOS) were calculated using the tetrahedral method with 133 uniformly distributed  $\vec{k}$ -point in the irreducible Brillouin zone (corresponding to 1728 in the full zone), which results in 432 tetrahedrons in the wedge.

### 3.3 EQUILIBRIUM PROPERTIES

In a cubic system the equilibrium lattice constant and bulk modulus can be obtained straightforwardly by calculating the total energy at a few values around the equilibrium lattice parameter, the lattice parameter and the bulk modulus being determined by a fit to the Murnaghan equation of

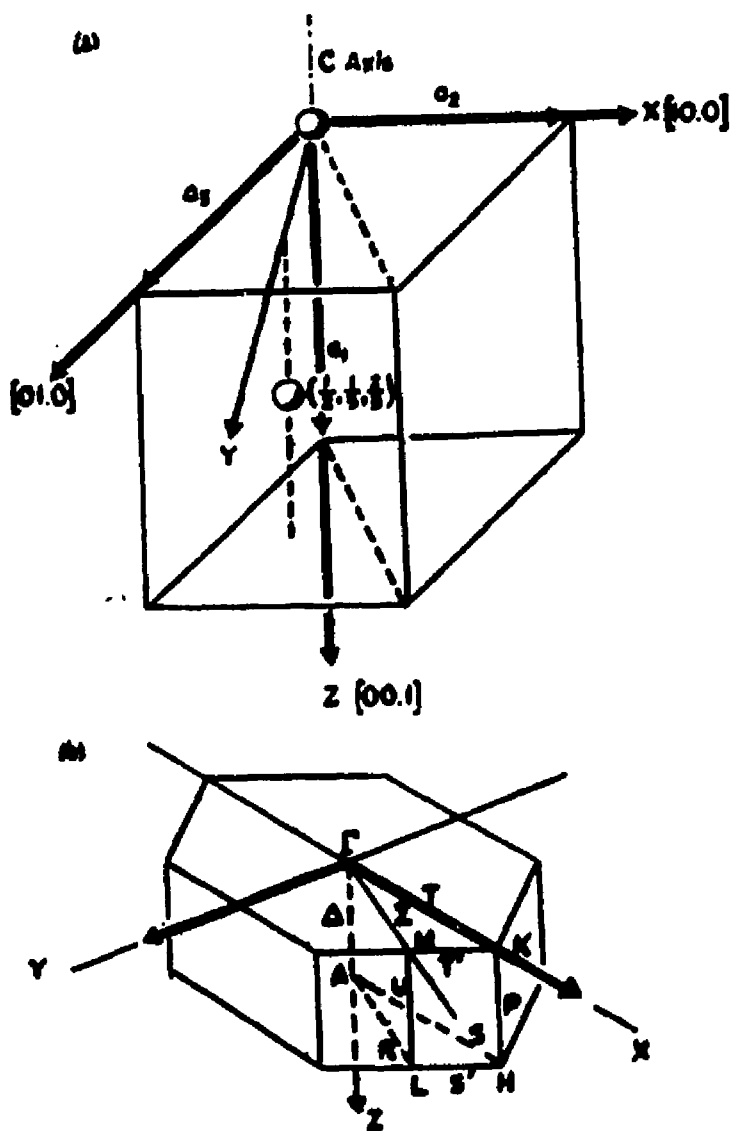


Figure 3.1 (a) Unit cell for the hexagonal-close-packed crystal structure. (b) Half of the Brillouin zone for the hexagonal-close-packed structure with the 1/24th zone (after ref. Hyg70).

state (Mur44),

$$E(V) = \frac{B_0 V}{B_0'} \left[ \frac{(V_0/V)^{B_0'}}{B_0' - 1} + 1 \right] + \text{const.} \quad , \quad (3.1)$$

where  $B_0$  and  $B_0'$  are the bulk modulus and its pressure derivative at the equilibrium volume  $V_0$ . However, for hcp titanium and zirconium, things are not so straightforward; one must optimize both lattice parameters  $a$  and  $c$ . The above approach is thus not directly applicable to hcp systems. In order to obtain a physically meaningful  $(V_0, B_0, B_0')$ , one must find  $E(V)$ , the minimum total energy at fixed volume. The approach used was to first calculate the total energy as a function of the  $c/a$  ratio at a fixed volume  $V$ , and then fit  $E(c/a)$  to a quadratic or a cubic form. The form used is given by

$$E(c/a) = \alpha(c/a)^3 + \beta(c/a)^2 + \gamma(c/a) + \delta \quad , \quad (3.2)$$

where  $\alpha, \beta, \gamma$  and  $\delta$  are fitting parameters. For each volume  $V$ , total energies at a minimum of four distinct  $c/a$  ratios are required by Eq. (2). From the fit of  $E(V)$ , the minimum energy at volume  $V$  was obtained. The resulting  $E(V)$  near the equilibrium volume was then used to extract  $(V_0, B_0, B_0')$  from a fit to (1). A similar procedure was used in ref. Che86. In order to evaluate the lattice parameters, one must find

the  $c/a$  ratio at the calculated equilibrium volume  $V_0$ . This was done using the total energy as a function of the  $c/a$  ratio at the equilibrium volume  $V_0$  which was obtained as above, the  $c/a$  ratio corresponding to the minimum energy in (2) being the equilibrium  $c/a$  ratio. This calculation at  $V_0$  provided additional data with which to check the accuracy of the Murnaghan fit. The fits turned out to be very stable for  $(V_0, B_0, B_0')$ . The rms fitting errors for both (1) and (2) were all within  $10^{-5}$  Ry. Tables 3.1 and 3.2 present the  $E(c/a)$  versus  $c/a$  at the calculated equilibrium volume  $V_0$  for Ti and Zr respectively using two different XC potentials, the Hedin-Lundqvist (HL) and  $X\alpha$  forms.

TABLE 3.1

$E(c/a) + C$  versus  $c/a$  at the calculated equilibrium volume for Ti. For HL,  $V_0=109.21$  a.u.<sup>3</sup>,  $C = 1703$  Ry and  $E(V_0) = -1703.97798$  Ry. For  $X\alpha$ ,  $V_0 = 116.65$  a.u.<sup>3</sup>,  $C = 1700$  Ry and  $E(V_0) = -1700.41153$  Ry.

HL		$X\alpha$	
$c/a$	$E(c/a)$	$c/a$	$E(c/a)$
1.540	-0.97771	1.560	-0.41136
1.570	-0.97795	1.570	-0.41149
1.585	-0.97798	1.585	-0.41153
1.600	-0.97796	1.600	-0.41152
1.634	-0.97774	1.615	-0.41148
		1.634	-0.41143



TABLE 3.2

$E(c/a) + C$  versus  $c/a$  at the calculated equilibrium volume for Zr. For the HL,  $V_0 = 147.85 \text{ a.u.}^3$ ,  $C = 7190 \text{ Ry}$ , and  $E(V_0) = -7190.42068 \text{ Ry}$ . For the  $X\alpha$ ,  $V_0 = 158.92 \text{ a.u.}^3$ ,  $C = 7183 \text{ Ry}$  and  $E(V_0) = -7183.26556 \text{ Ry}$ .

HL		$X\alpha$	
$c/a$	$E(c/a)$	$c/a$	$E(c/a)$
1.580	-0.42044	1.570	-0.26538
1.600	-0.42059	1.585	-0.26549
1.620	-0.42067	1.600	-0.26555
1.630	-0.42068	1.615	-0.26555
1.640	-0.42065	1.634	-0.26546

We also tabulate the minimum energies  $E(V)$  at fixed volumes,  $V$ , in Table 3.3 and 3.4, which are plotted in Figs. 3.2-3.3 for Ti and Zr respectively along with the Murnaghan equation of state fits.

We find that the structural parameters of both Ti and Zr are rather sensitive to the particular form of the XC potential used. It is found that the HL XC potential significantly underestimates the equilibrium volumes of both Ti and Zr, while the simpler  $X\alpha$  form yields very good ground state properties for these two elements. We will return to this issue later on.

The calculated  $E(c/a)$  (Tables 3.1 and 3.2) at the equilibrium volume clearly reveals that these curves are very flat, which makes it difficult to predict the exact  $c/a$

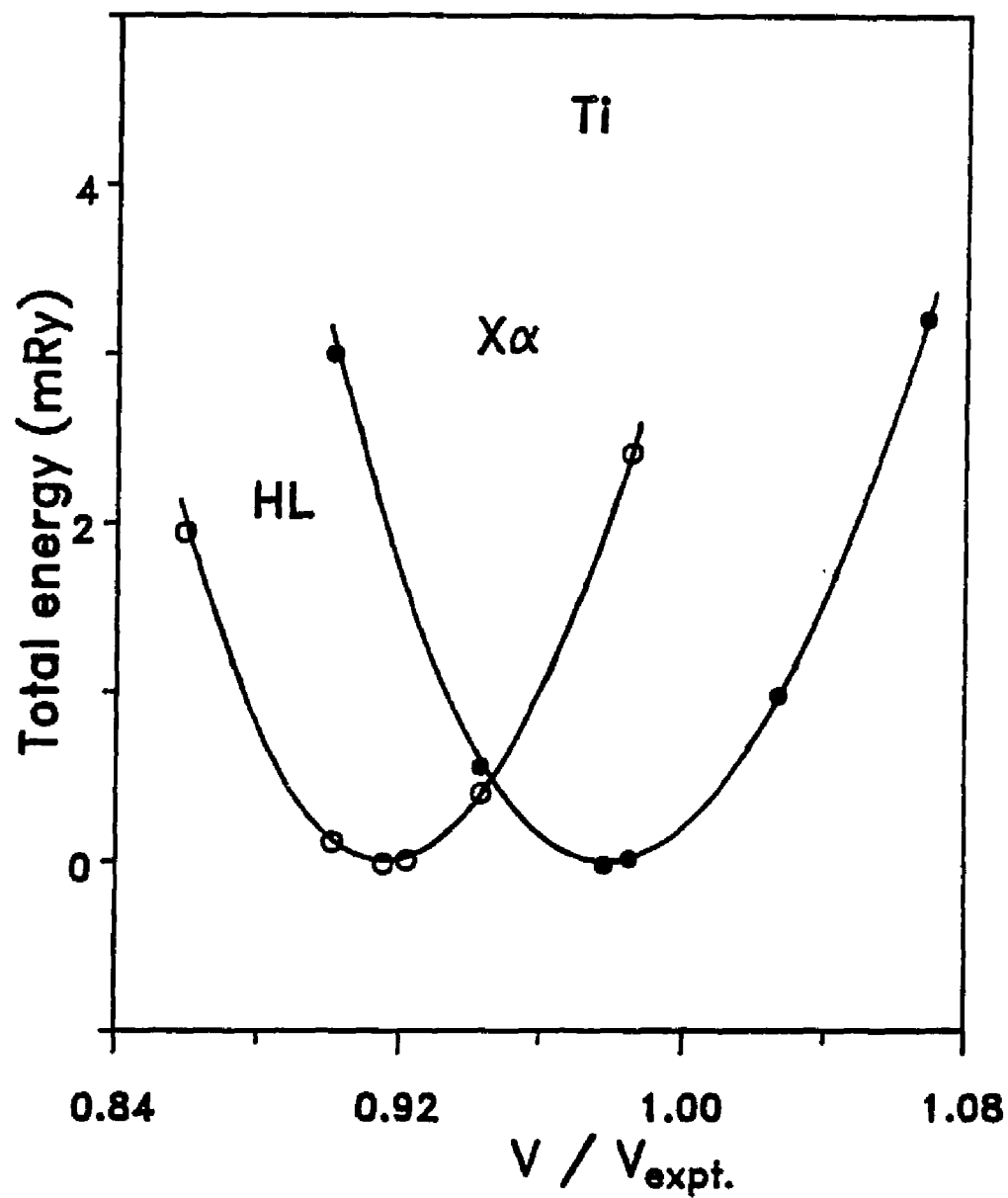


Figure 3.2 Calculated  $E(V) - E(V_0)$  vs  $V$  of Ti with the HL and  $X\alpha$ , the solid line is a Murnaghan equation of state fit.  $E(V_0) = -1703.97798$  Ry for the HL and  $E(V_0) = -1700.41153$  Ry for the  $X\alpha$ .

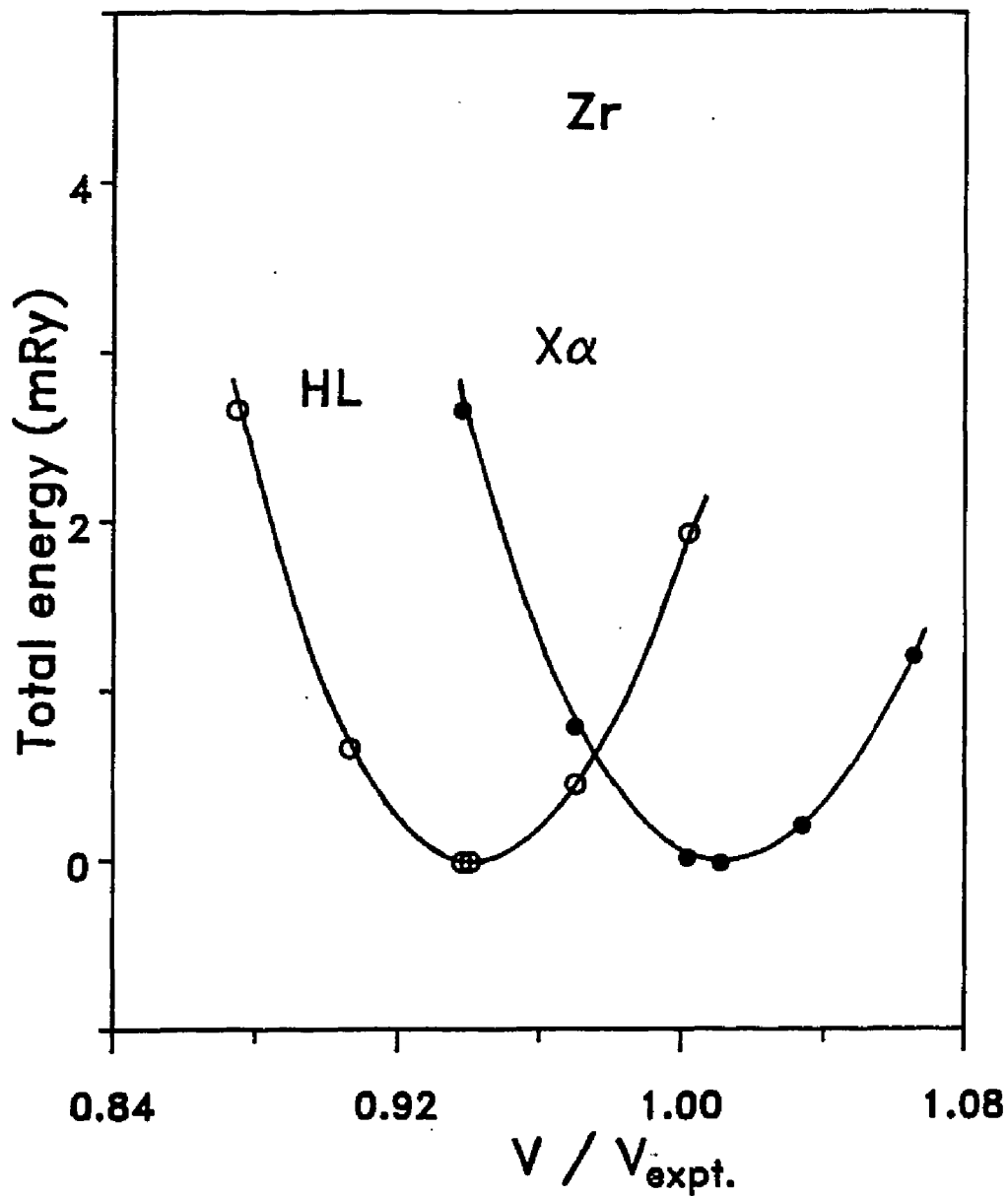


Figure 3.3 Calculated  $E(V) - E(V_0)$  vs  $V$  of Zr with the HL and  $X\alpha$ , the solid line is a Murnaghan equation of state fit.  $E(V_0) = -7190.42068$  Ry for the HL and  $E(V_0) = -7183.26556$  Ry for the  $X\alpha$ .

ratio. We estimate the error in the predicted  $c/a$  ratios to be about 1-2%. Both the experimental and our calculated value of  $c/a$  are less than the ideal value of  $\sqrt{8/3}$  (1.6333) for both Ti and Zr. In Table 3.3 and 3.4, we also list minimum energies  $E(V)$  and the corresponding  $c/a$  ratios at various volumes. The  $c/a$  ratios are plotted in Fig. 3.4. For Ti, the  $c/a$  ratio is weakly volume dependent. The considerable scatter in the calculated  $c/a$  ratios around an equilibrium value of 1.588 for Ti reflects the very small energy changes associated with this distortion. By contrast, the  $c/a$  ratio for Zr is considerably more volume dependent increasing with decreasing volumes. Similar behavior was found for Ru in ref. Che86.

TABLE 3.3

Minimum  $E(V) + C$  (Ry) as determined from Eq. (1) vs volume  $V$  (a.u.<sup>3</sup>) and the corresponding  $c/a$  ratio for Ti. For the HL,  $C = 1703$  Ry. For the  $X\alpha$ , constant = 1700 Ry.

$V$	HL $E_0$	$c/a$	$V$	$X\alpha$ $E_0$	$c/a$
102.50	-0.97602	1.596	107.50	-0.40851	1.583
107.50	-0.97785	1.590	112.50	-0.41095	1.582
109.21	-0.97798	1.586	116.65	-0.41153	1.595
110.00	-0.97796	1.588	117.50	-0.41148	1.600
112.50	-0.97756	1.587	122.50	-0.41053	1.590
117.50	-0.97555	1.590	127.50	-0.40830	1.592

TABLE 3.4

Minimum  $E(V) + C$  (Ry) as determined from Eq. (1) vs volume  $V$  (a.u.<sup>3</sup>) and the corresponding  $c/a$  ratio for Zr. For HL,  $C = 7190$  Ry. For the  $X\alpha$ ,  $C = 7183$  Ry.

HL			$X\alpha$		
$V$	$E_0$	$c/a$	$V$	$E_0$	$c/a$
137.50	-0.41801	1.647	147.50	-0.26289	1.621
142.50	-0.42001	1.644	152.50	-0.26476	1.618
147.50	-0.42068	1.626	157.50	-0.26553	1.611
147.85	-0.42068	1.627	158.92	-0.26556	1.608
152.50	-0.42022	1.620	162.50	-0.26534	1.598
157.50	-0.41874	1.613	167.50	-0.26434	1.596

Having calculated the  $c/a$  ratios, it is straightforward to find the lattice parameters  $a$  and  $c$  from the equilibrium volume obtained from the Murnaghan fit (1) as well as other equilibrium properties such as Poisson's ratio and the cohesive energy. These are reported in Tables 3.5 and 3.6. The experimental lattice parameters were taken from Ref. Vil85. In order to obtain the cohesive energies, the total energies of the isolated atoms were calculated using the same XC potential as in the bulk calculation. The difference between  $E_{\text{atom}}$  and  $E(V_0)$  yields the cohesive energy,  $E(V_0)$ , being the total energy at equilibrium volume  $V_0$  as determined from (2). The LSD ground state configurations are Ti( $3d^3 4s^1$ ) and Zr( $4d^3 5s^1$ ) (Mor78). We calculated the cohesive

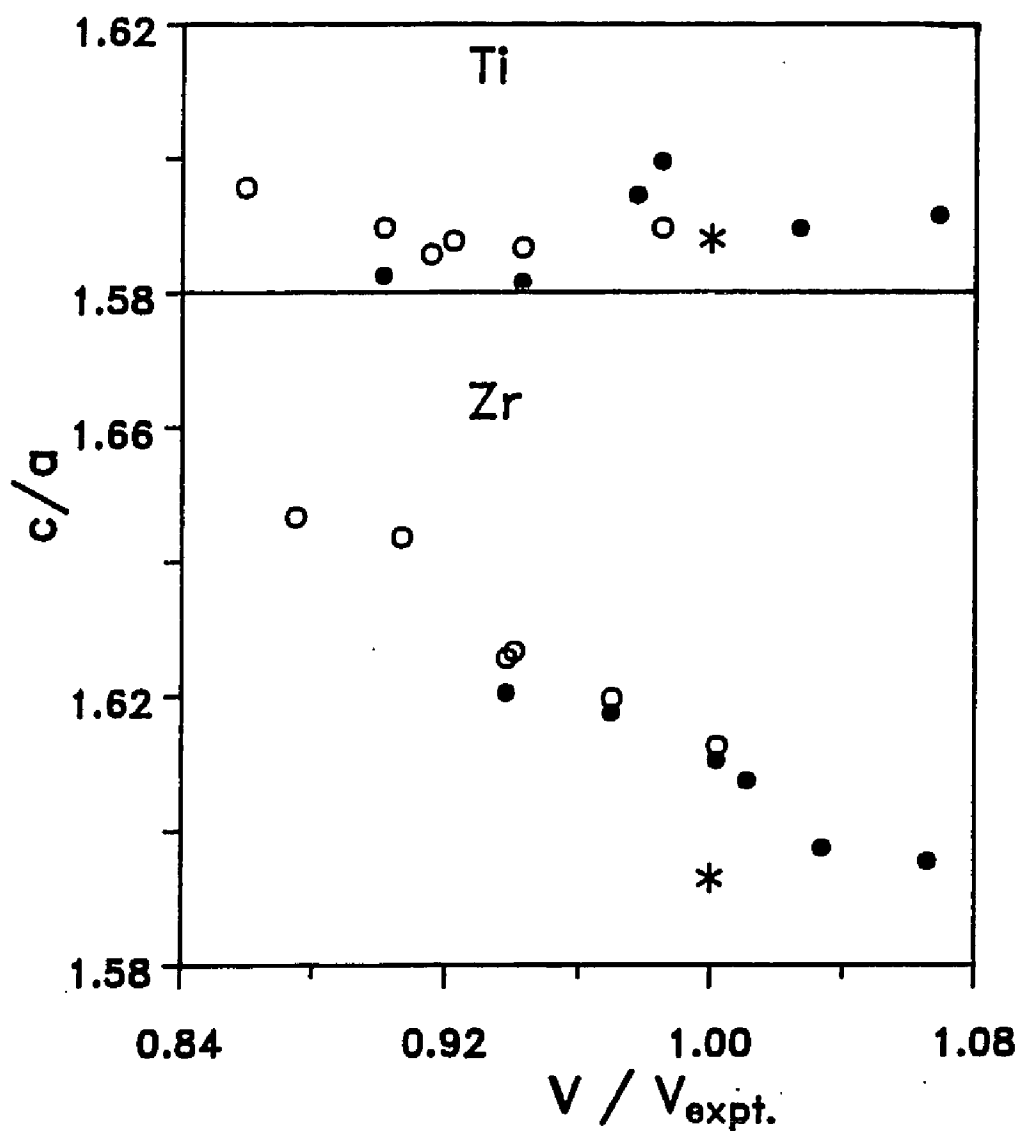


Figure 3.4  $c/a$  ratio corresponding to the minimum energy at certain volume versus volume for Ti and Zr. ○ for the HL, ● for the  $X\alpha$ , and \* for the experimental  $c/a$  ratio at experimental volume.

energies using both the von Barth-Hedin (spin-polarized version of the HL) and the  $X\alpha$  XC potentials. The calculated atomic energies,  $E_{\text{atom}}$ , are -1703.5061 Ry for Ti and -7189.-8768 Ry for Zr using the HL XC potential.  $E_{\text{atom}}$  and  $E(V_0)$  can be found in Table 3.7. The cohesive energies thus obtained are about 32% larger than the experimental value (Kit76) for Ti and 18% larger for Zr. When the  $X\alpha$  XC potential was used, we find that  $E_{\text{atom}} = -1700.0290$  Ry for Ti and -7182.8214 Ry for Zr. Thus, the cohesive energies are in better agreement about 7% larger than the experimental values for Ti and 3% less than the experimental value for Zr. It is well known that the local density approximation tends to overestimate the cohesive energies, the error coming mainly from the atomic calculation. This is the case for the HL result, errors of similar size for Ti were also observed by Moruzzi *et al.* (Mor78), who calculated the electronic properties using a close-packed fcc lattice, which is very similar to hcp structure. For Zr, the calculated value in ref. Mor78 was 6.75 eV in somewhat better agreement with experiment than the present results. While for the  $X\alpha$ , we underestimate the cohesive energy for Zr. Hattox *et al.* (Hat73) also found underestimation of cohesive energy for Vanadium with the  $X\alpha$  method, the number was 0.33 Ry. Moruzzi *et al.* (Mor78) overestimated the cohesive energy of Vanadium with Von Barth-Hedin XC potential, which was 0.450 Ry, the cohesive energy difference between these two calculations is about .

0.12 Ry. We find that the cohesive energy differences between the HL and  $X\alpha$  for Ti and Zr are of the same magnitude.

TABLE 3.5

Ground state properties of Ti in the hcp structure and a comparison with the experimental data. The experimental data are from ref. Vil85, Kit76 and Fis64.

Property	Experiment	HL	$X\alpha$
$V_0$ (a.u. <sup>3</sup> )	119.210	109.21	116.65
$c/a$	1.588	1.586	1.595
$a$ (Å)	2.9508	2.866	2.925
$c$ (Å)	4.6855	4.547	4.666
Bulk Modulus (Mbar)	1.05	1.27	1.08
$B_0'$		3.59	3.82
Poisson's Ratio	0.26	0.32	0.31
Cohesive Energy (eV)	4.85	6.42	5.20

Poisson's ratio  $\sigma$  is the negative ratio of the transverse strain to the corresponding axial strain in a body subject to uniaxial stress. For a fixed value of  $c$ , the total energies at three (or more) different values of  $a$  were calculated and fit to a parabola. The value of  $a$  ( $a_{min}$ ) which corresponds to the minimum total energy was then used to evaluate  $\sigma$  directly from a linear fit of  $a_{min}$  versus  $c$ .



$$\sigma = - (\Delta a / \Delta c) (c/a) \quad (3)$$

where  $\Delta a / \Delta c$  is the slope of the fit and  $c/a$  is the equilibrium  $c/a$  ratio. Uniform meshes of nine values of  $c$  and  $a$  around the experimental  $c$  and  $a$  values were used except for  $X_\alpha$  Ti calculation, for which a twelve point mesh was used. The results are shown in Fig. 3.5 and in Tables 3.5 and 3.6 along with the single crystal Poisson's ratio obtained from the elastic constants of ref. Fis64. It may be noted that the HL XC potential tends give a somewhat larger Poisson's ratio for both elements. The sensitivity of the calculated results to the particular form of the XC potential deserves some discussion. We find that for both Ti and Zr the calculated  $V_0$  and  $B_0$  are in very good agreement with experiment when the  $X_\alpha$  ( $\alpha=2/3$ ) XC potential was used, the deviation for the equilibrium volume ( $V_0$ ) being -2.2% for Ti and +1.2% for Zr. However, when the Hedin-Lundqvist XC was used, larger discrepancies in the equilibrium volumes are found, the deviations being -8% and -6% for Ti and Zr respectively. In this case bulk moduli,  $B_0$ , are about 20% larger than the experimental values as might be expected based on the smaller calculated equilibrium volumes. Sensitivity of this magnitude has previously been reported for semiconductors (Hol-83). The  $c/a$  ratios are all within in 1% of the experimental values, except for Zr with the HL form, where the discrepancy is about 2%. As we have discussed before, the  $X_\alpha$

form predicts better cohesive energies than the HL form for both Ti and Zr, but in both cases the cohesive energies are overestimated except Zr with the  $X\alpha$  from, which underestimates the cohesive energy by about 3%.

TABLE 3.6

Ground state properties of Zr in the hcp structure and a comparison with the experimental data. The experimental data are from ref. Vil85, Kit76 and Fis64.

Property	Experiment	HL	$X\alpha$
$V_0$ (a.u. <sup>3</sup> )	157.05	147.84	158.92
$c/a$	1.593	1.627	1.608
$a$ (Å)	3.232	3.145	3.234
$c$ (Å)	5.147	5.116	5.200
Bulk Modulus (Mbar)	0.833	0.986	0.846
$B_0'$		3.00	4.02
Poisson's Ratio	0.29	0.34	0.29
Cohesive Energy (eV)	6.25	7.40	6.04

### 3.4 ELECTRONIC PROPERTIES

The band structure and the density of states of Ti have been previously calculated by a number of authors using a variety of methods (Alt58a, Mat64, Hug70, Jep75a, Fei79). The band structure reported here was calculated at the experimental lattice parameters (Vil85) using both the HL and

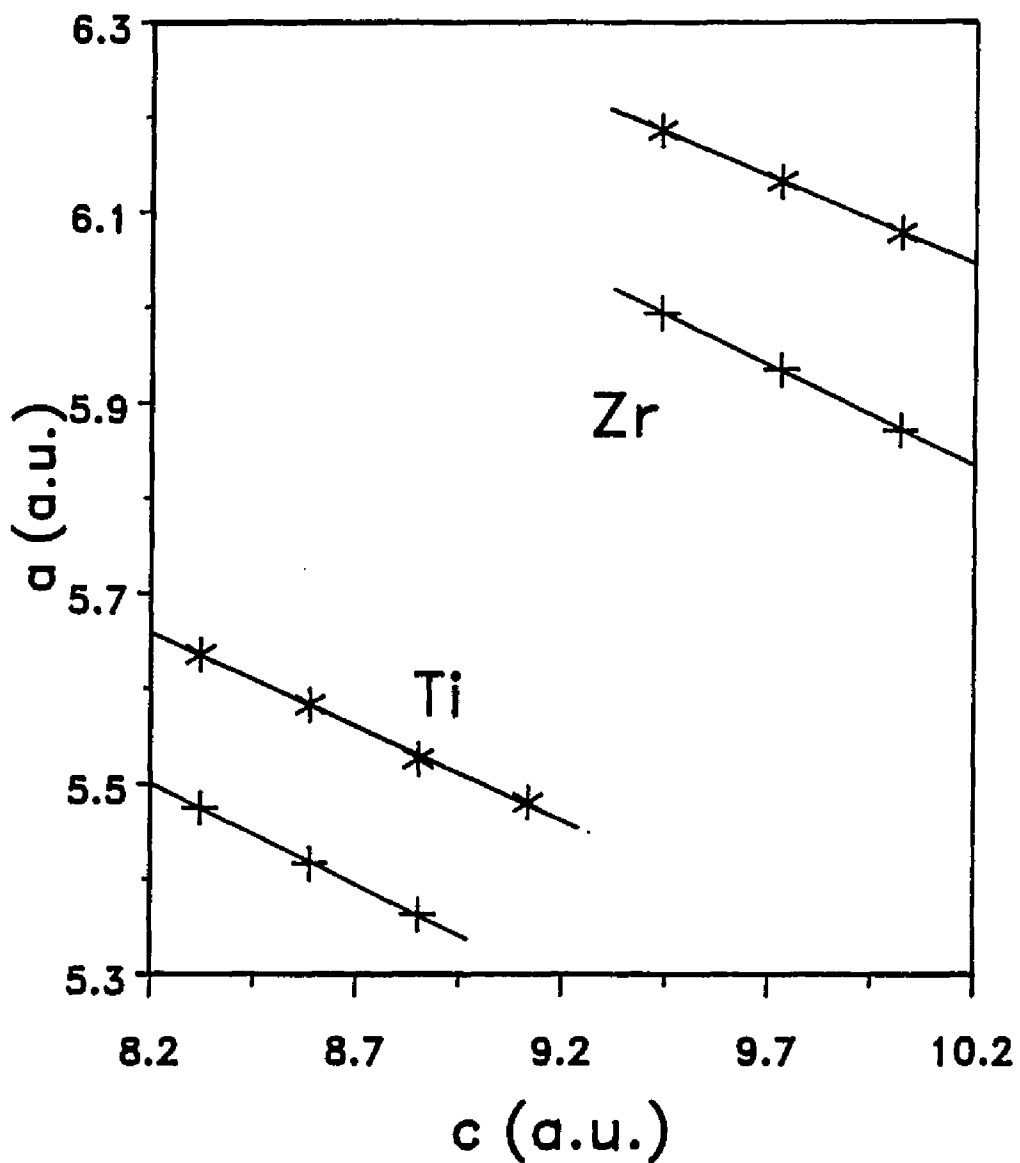


Figure 3.5 Linear relationship between  $c$  and  $a_{min}$  gives Poisson's ratio (see text). + for the HL, \* for the  $X\alpha$ .

$X\alpha$  XC potentials. Interestingly, the band structures thus obtained are almost identical, which are shown in fig. 3.6-3.7. Our band structure (see the large version Fig. 3.6) is very similar to that calculated by Jepsen(Jep75a), using a non self-consistent linear-muffin-tin-orbital method. In particular the crossings at the Fermi level are practically identical. Jepsen rather thoroughly reviewed and compared his results with earlier calculations, and he found that his Fermi surface was in agreement with the de Haas-van Alphen experiment of Kamm and Anderson(Kam74). Some differences between our band structure and his may be expected, since we used the  $X\alpha$  ( $\alpha=2/3$ ) and the HL XC potentials instead of the Slater ( $\alpha=1$ ) form. Besides, his calculation was not self-consistent. Noticeable differences are found along the  $T'$  and  $P$  directions. One of the energy levels was degenerate in his band structure, but not in ours. This is the 1 and 4 of  $T'$  band at the bottom and 1 and 2 of  $P$  at the bottom. It may have been just accidentally degenerate in his calculation, since in their Zr calculation(Jep75b) these bands were split. These bands were split in the self-consistent calculation of Feibelman *et al.* (Fei79), which was obtained using a linear combination of Gaussian orbitals approach and yielded a very similar band structures to the present result. Our calculated density of states ( $X\alpha$ ) (Fig. 3.8) is very similar to Jepsen's (Jep75a). The density of states at the Fermi level is 12.3 states/atom/Ry while his number was

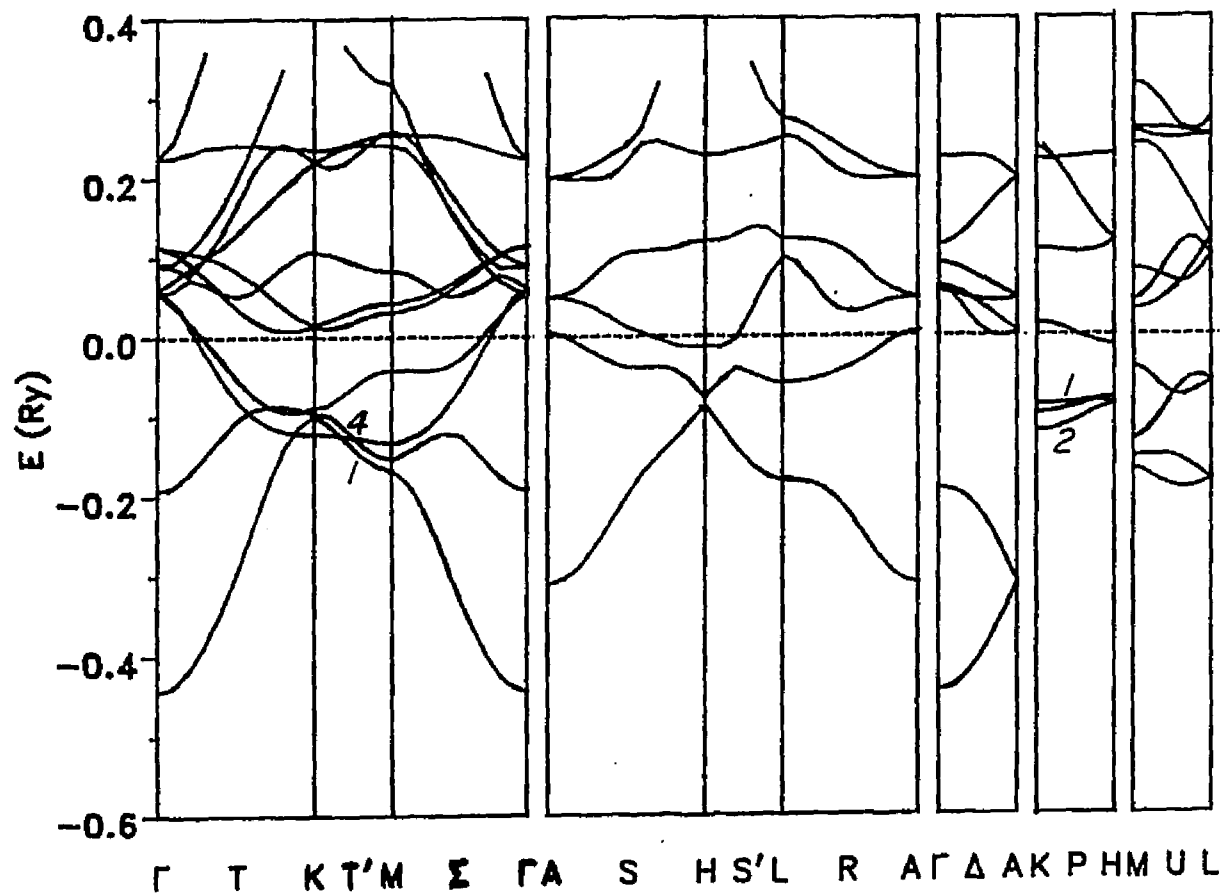


Figure 3.6 Band structure for Ti using the HL XC.

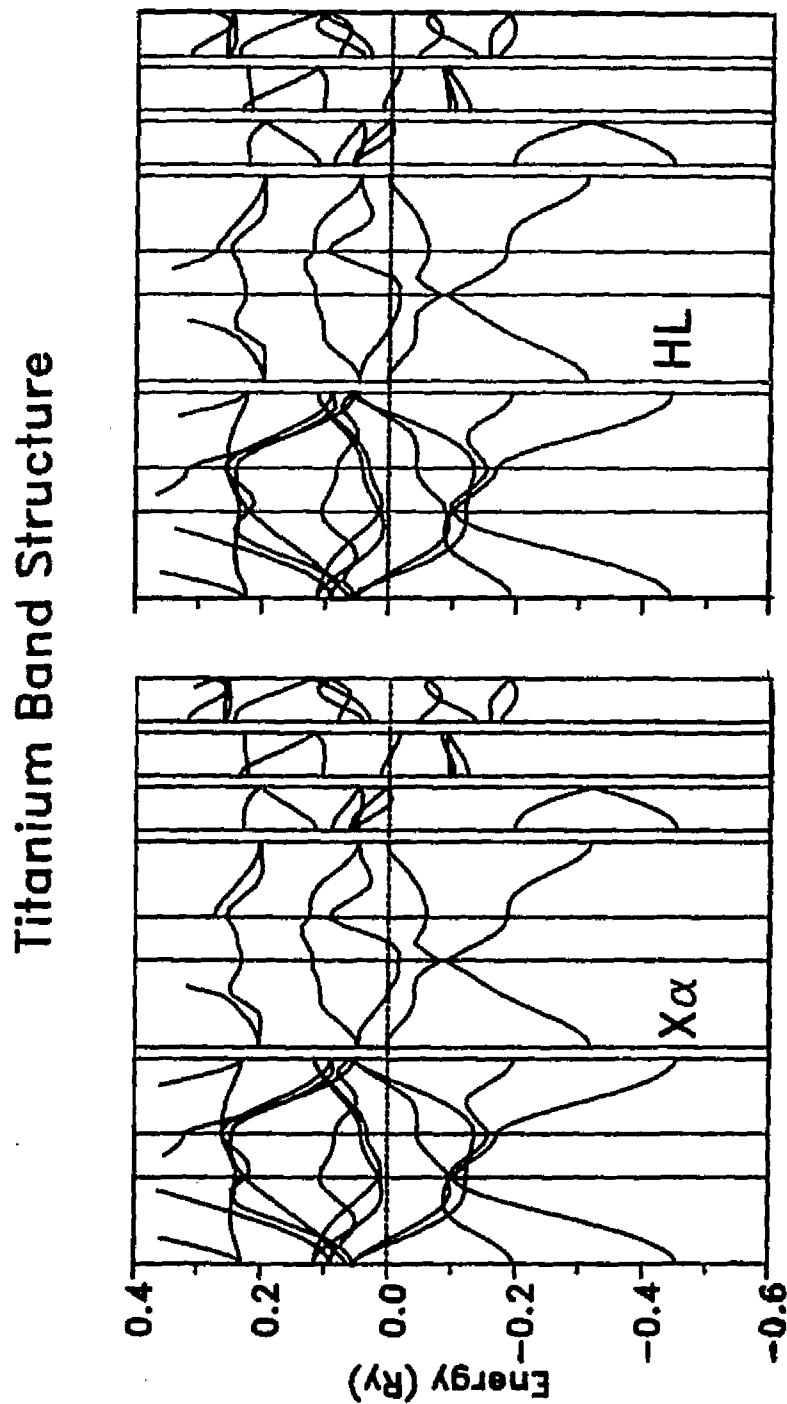


Figure 3.7 Band structure for Ti at equilibrium lattice constants using the  $X\alpha$  and the HL XC potentials are nearly identical; see Fig. 3.6 for labels.

12.4 states/atom/Ry. This is a very good agreement. The DOS is primarily  $d$ -like, the small peak just below the Fermi energy is due mostly to  $p$  electron contributions. In Fig. 3.9, we show the contour plot of the valence charge density of titanium on the hexagonal face, which reflects the symmetry of the lattice and bonds between atoms.

Table 3.7

Spin-polarized total energies for isolated atom Ti and Zr,  $E_{\text{atom}}$ , and minimum total energies for hcp Ti and Zr,  $E(V_0)$ .

	HL	$E_{\text{atom}}$ $X\alpha$	HL	$E(V_0)$ $X\alpha$
Ti	-1703.5061	-1700.0290	-1703.9780	-1700.4115
Zr	-7189.8768	-7182.8214	-7190.4207	-7183.2656

The band structure, density of states and charge density contour of Zr, are shown in Figs. 3.8, 3.10-12. As in the case of Ti, the band structures calculated using the HL and  $X\alpha$  XC potential are very similar. A few previous calculations of electronic structure of Zr have been reported (Alt58b, Lou67b, Jep75b, Iya76, cha84). We find that as for Ti our results for both the band structure and the density of states are very similar to those obtained by Jepsen *et al.* (Jep75b). The density of states ( $X\alpha$ ) is shown in Fig. 3.8. We find the density of states at the Fermi level is 11.3

states/atom/Ry, while the number in ref. Jep75b was 13.1 states/atom/Ry. We also show the contour plot of the charge density of zirconium (Fig. 3.12) which is very similar to that of Ti.

### 3.5 SUMMARY

We find that the calculated equilibrium volumes are underestimated using the HL XC potential, with deviations of about 8% for titanium and 6% for zirconium. The bulk moduli are found to be about 20% larger than the experimental values for both elements. The cohesive energies are overestimated as commonly found in the LDA calculations. The discrepancy between the experimental and the calculated values are 32% and 18% for titanium and zirconium respectively. The Poisson's ratios are about 20% larger than the measured values. We also find that there is considerable sensitivity to the XC potential by comparing with parallel calculations using the exchange-only  $X_{\alpha}$  form. We find that equilibrium volumes, lattice parameters,  $c/a$  ratios and bulk moduli are in very good agreement with experiment for both titanium and zirconium, in this case the cohesive energies also being brought better agreement with the experiment. Our band structures and densities of states are in good agreement with the earlier calculations of Jepsen (Jep75a) and Feibelman *et al.* (Fei79) for titanium and Jepsen *et al.* (Jep75b) for zirconium. The changes in the equilibrium



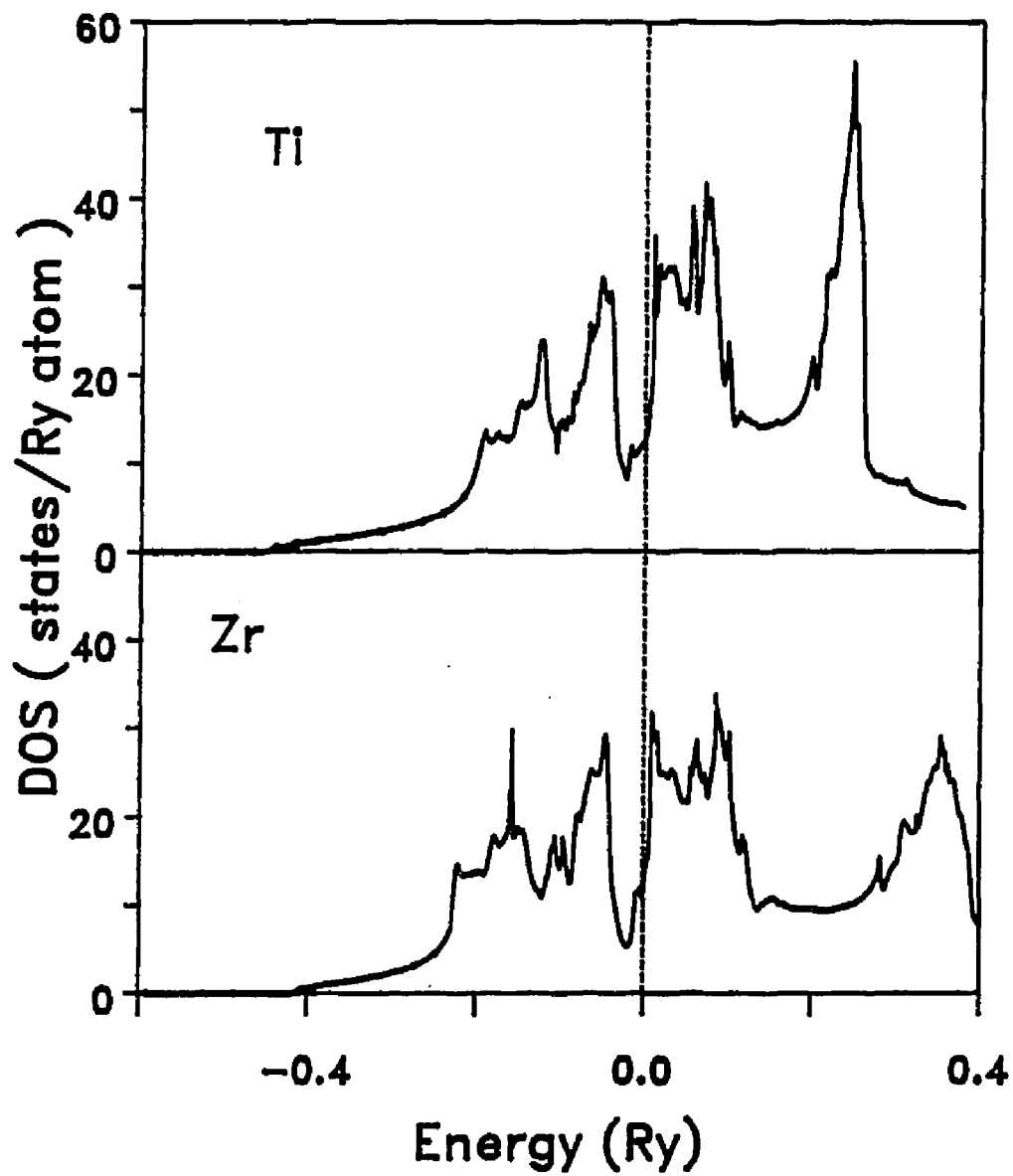


Figure 3.8. Density of states for Ti and Zr (the  $X\alpha$  potential). The Fermi energy is indicated by the dashed line.

# Titanium

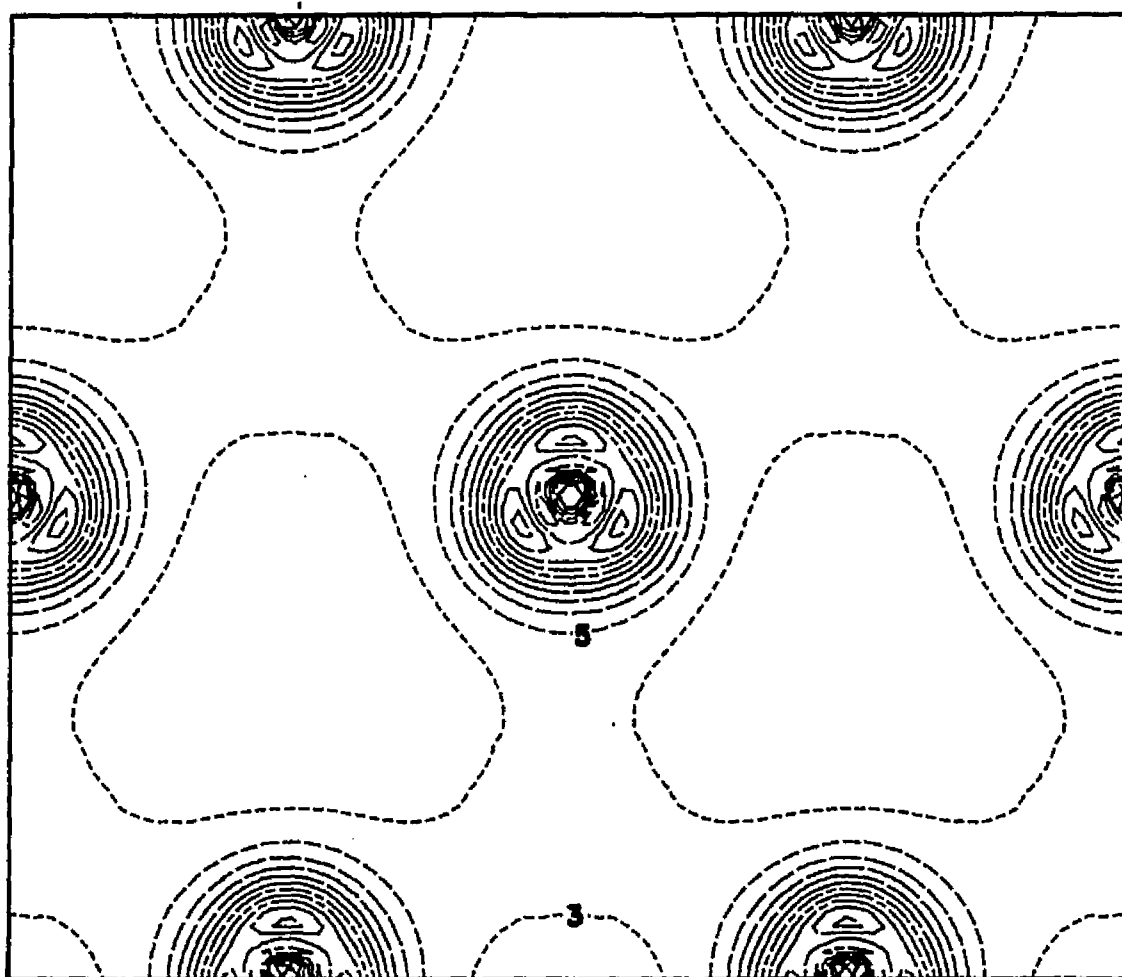


Figure 3.9 Contour plot of the valence charge density of Ti calculated using *the X $\alpha$*  potential. The charge density is given in units of  $10^{-2} e/a.u.^3$ ; the step size is 2.

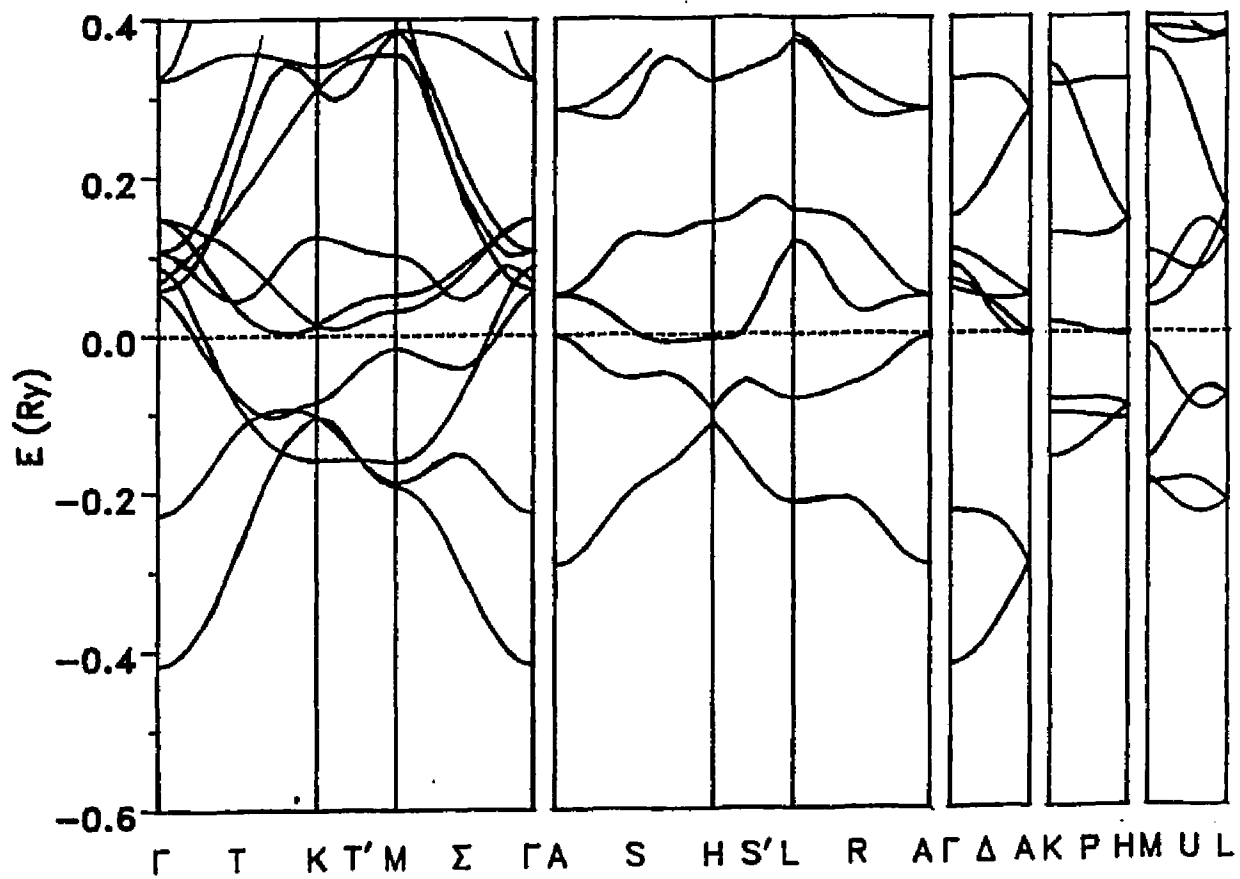


Figure 3.10 Band structure for Zr using the HL.

## Zirconium Band Structure

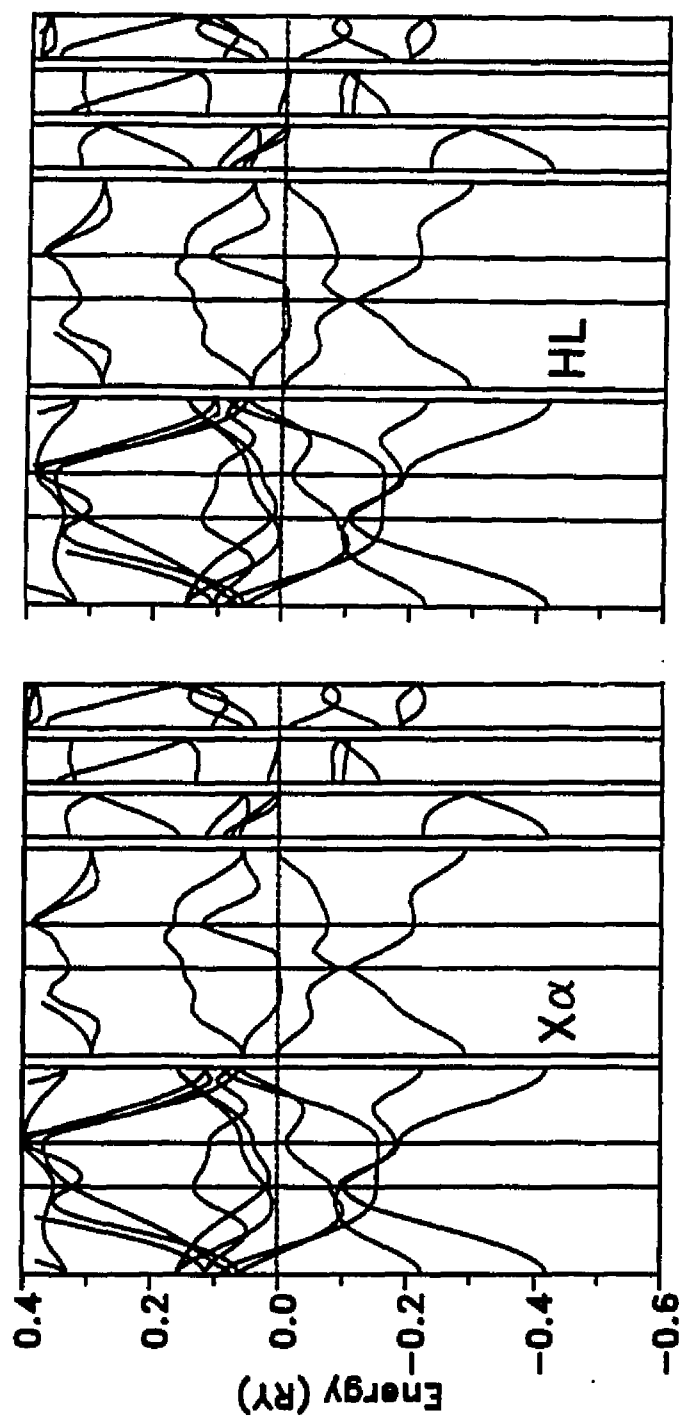


Figure 3.11 Band structure for Zr using the  $X\alpha$  and the HL at equilibrium lattice constants are very similar, see Fig. 3.10 for labels.

# Zirconium

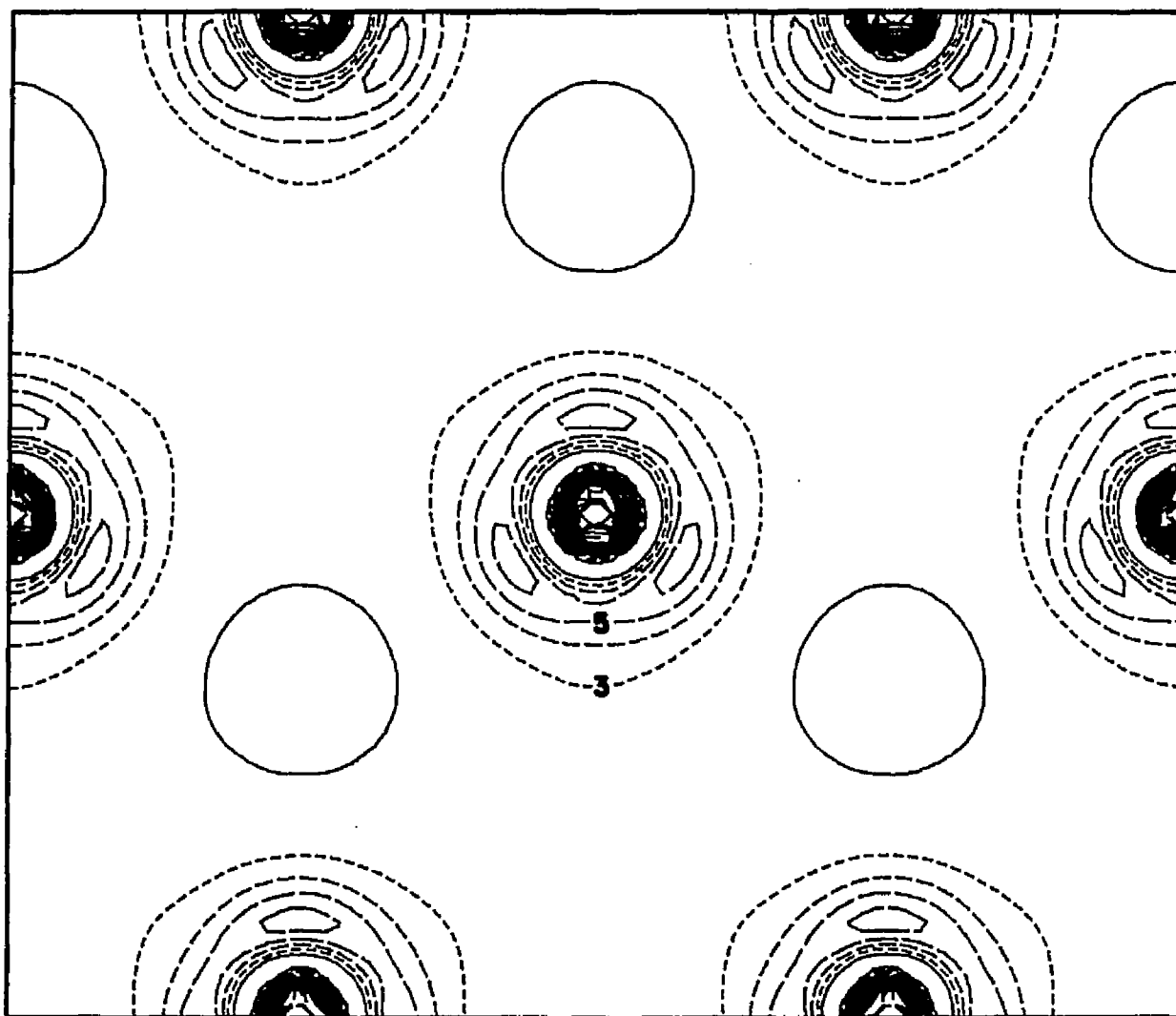


Figure 3.12 Contour plot of the valence charge density of Zr calculated using the  $X_{\alpha}$  potential. The charge density is given in units of  $10^{-2} e/a.u.^3$ ; the step size is 1.

volume due to the use of different XC potential ( $X\alpha$  vs HL) are found to be about 6%. We take this to be an indication of the intrinsic accuracy of the LDA for 3d and 4d transition metals.

## Chapter IV

### fcc and bcc Lanthanum

#### 4.1 INTRODUCTION

Lanthanum, because of its unusual physical properties, has received considerable attention in recent years. Lanthanum exists in three different phases at atmospheric pressure: double-hcp  $\alpha$  phase is the stable phase below 609 K; the fcc  $\beta$  phase is stable between 609 K and 1138 K, (however, the  $\beta$  phase can exist below 609 K in a metastable form); and bcc  $\gamma$  phase exists above 1138 K and below 1191 (the melting point). Compared with its 3d and 4d analogues scandium and yttrium, lanthanum has an anomalously low Debye temperature (Joh67) and high superconducting transition temperature (Bla75). Lanthanum's superconductivity is unusual that the transition temperature has a very high pressure derivative  $dT_c/dP \approx 0.1$  K/kbar (Bla75), which shows considerable structure at moderate pressures. In addition to its relatively high temperature superconductivity, lanthanum shows unusual behavior in the temperature dependence of its Knight shift (Blu60), its electronic specific heat (-Par50, Joh67) and thermal expansion (Eli64, And68). These unusual physical properties combined with an analysis of the

temperature dependence of the magnetic susceptibility(Loc57) which suggested effective localized moments of about  $\frac{1}{2}\mu_B$  had led to some controversy regarding the extent to which lanthanum is a *f*-band metal. More recently, band structure calculations(Pic80) have indicated that the 4*f* band in lanthanum lies above the Fermi energy and that the hybridization with the occupied states is therefore small. Thus, in addition to its intrinsic interest, lanthanum is of importance as a reference system for the chemically similar 4*f*-band metals.

Here we report the results of self-consistent LAPW calculations of total energies and electronic structures of fcc and bcc lanthanum, performed in order to establish the reliability of LDA-based calculations for this material by examining the sensitivity of our results to the particular form of the local exchange-correlation (XC) potential used and their agreement with experimental data, and also to calculate the energy difference between the high-temperature bcc structure and one of the low-temperature close-packed structures, which is of interest in seeking an understanding of the structural phase transition.

#### 4.2 DETAILS OF CALCULATION

In our calculations, three different forms of XC potential were used, i.e. the  $X_\alpha(\alpha=2/3)$  (Koh65), Wigner interpolation (WIG)(Wig34), and Hedin-Lundqvist(HL)(Hed71) XC



potential. Both the band states and core states are treated relativistically, the spin-orbit interaction for the band states being calculated from the scalar relativistic bands in a second variational step. The calculations were iterated to self-consistency, which was considered achieved when the total energies were stable to  $10^{-5}$  Ry. A lanthanum muffin-tin sphere radius of 3.281 a.u. was used with a basis-set cutoff,  $K_{\max}^2 = 7.524$  Ry. The unit cell and Brillouin zone for both the fcc and bcc structure are illustrated in Figure 4.1. The Brillouin zone summations over the valence states were performed using 110 special  $\bar{k}$ -points (Mon76) for fcc lanthanum and 40 special  $\bar{k}$ -points for the bcc phase. The rather extended lanthanum 5p core state was treated in a separate energy window using 10 (8) special  $\bar{k}$ -points for the fcc (bcc) phase. These samplings were found to yield total energies converged to the order of 0.5 mRy. A calculation in which the lanthanum 5p state was treated as a normal core state yielded a bulk modulus differing by a factor of 2 from the parallel two window calculation (see Table 4.1), underscoring the need to treat this state variationally. The densities of states were calculated using the tetrahedron method with 262 (202)  $\bar{k}$ -points in an irreducible wedge of the fcc (bcc) Brillouin zone.

#### 4.3. TOTAL ENERGY CALCULATIONS

Our principal results for the energetics of fcc La are

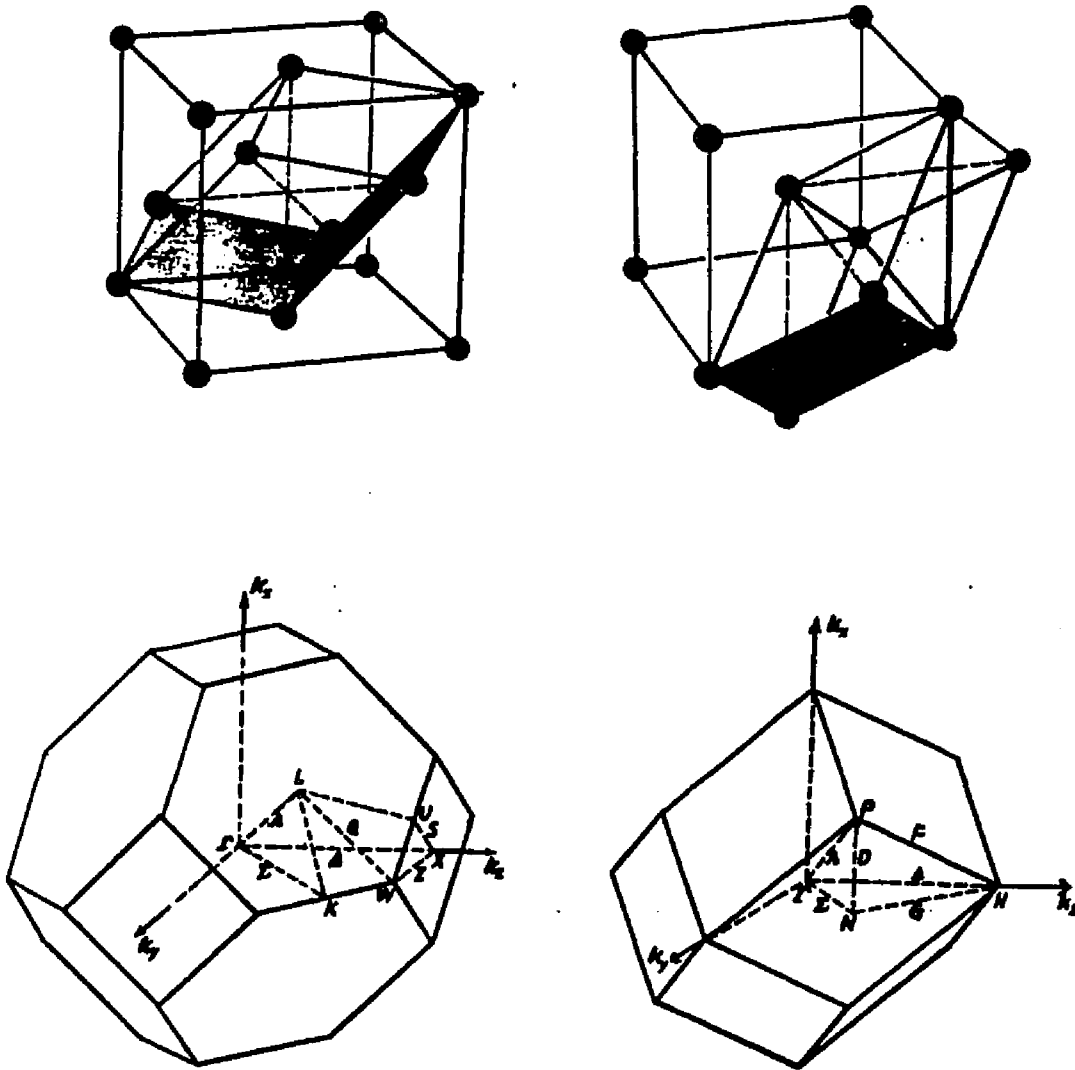


Figure 4.1 (a) unit cell for face centered cubic structure, (b) unit cell for body centered cubic structure, (c) first Brillouin zone for fcc, and (d) first Brillouin zone for bcc.

shown in Fig. 4.2, where the calculated total energies are plotted as a function of the volume of the unit cell for three different XC potentials, specifically the  $X_\alpha$  ( $\alpha=2/3$ ) form, the WIG form, and the HL form. The solid lines in Fig. 4.2 are fits to the Murnaghan equation of state which were used to extract the equilibrium volumes, the bulk moduli, and their pressure derivatives from the calculated total energies. The results of these fits are given in Tables 4.1 and 4.2, along with the results of previous linearized muffin-tin-orbital (LMTO) (Glö78, McM81a) calculations and experimental values (Sya75). It may be noted that there is a rather large dependence of the calculated structural properties on the particular form of the XC potential used. We take this to be an indication of the reliability of LDA based calculations for this material. One possible source of this large dependence is the combination of the softness of the material (i.e., the fact that only relatively small changes in the total energy differences are required to yield significant changes in the structural properties) and the fact that La has occupied valence  $d$ -states. The reasoning goes as follows. The  $d$ -bands and the interstitial  $s$ -derived states are in spatial regions with very different charge densities, and the volume-dependence of the density in these two spatial regions is quite different. The equilibrium structural properties are determined by an interplay of effects involving both these spatial

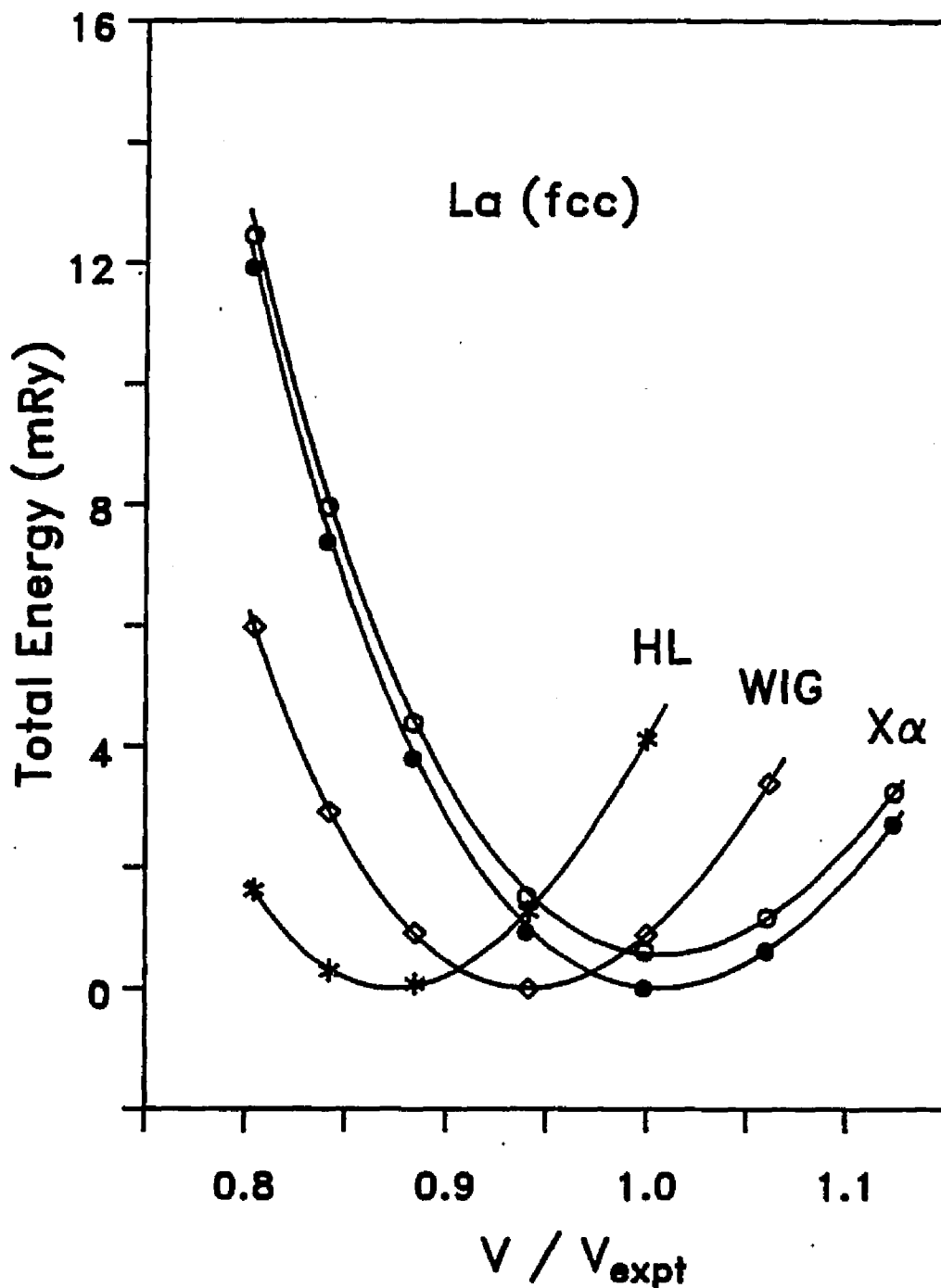


Figure 4.2 Calculated total energy -  $E_{\text{min}}$  vs. volume for fcc La for the  $X\alpha$ , WIG, and HL form respectively, the solid lines being their respective Murnaghan equation of state fit. For the  $X\alpha$  form, the lower curve was determined including the spin-orbit interaction, while the upper curve omits it.

regions(Gel83). Since the material is quite soft the observed sensitivity to the form of the local XC potential is not entirely unexpected. Similar dependencies of the structural properties on the particular form of XC potential have been observed in other materials. In particular, calculations using the  $X_{\alpha}$  form for Ti and Zr yielded larger lattice parameters and smaller bulk moduli than parallel Hedin-Lundqvist calculations as demonstrated in previous chapter. Similar trends have also been found for Cr(Che88) and Si (McM81b). This tendency for the  $X_{\alpha}$  form to yield larger lattice parameters in many materials than XC potentials which more accurately reproduce the results for the uniform electron gas may be related to the fact that it yields more extended valence wavefunctions in atomic calculations. (Note that the Wigner form is intermediate between  $X_{\alpha}$  and Hedin-Lundqvist forms.) Table 4.3 lists the atomic calculations for La using three different XC forms. It is apparent that the  $X_{\alpha}$  yields the most extended 5d and 6s orbital, while the HL has the smallest 5d and 6s orbitals. Furthermore, the HL has the smallest energy level difference  $E_{5s} - E_{6d}$ . Therefore, the HL has the strongest hybridization, as a result, it yields the smallest lattice constant and the largest cohesive energy.

Glötzel(GlÖ78) has reported a spin polarized self-consistent LMT0 calculation of the equilibrium properties of fcc lanthanum using the von Barth-Hedin XC potential(Bar72)

which is a generalization for spin polarized calculations of the Hedin-Lundqvist form. He obtained an equilibrium lattice parameter about 4% smaller than the experimental value consistent with our results, but with a smaller bulk modulus in better agreement with experiment. McMahan *et al.* (McM81a) used a similar approach to study the extreme high-pressure equation of state for this material, obtaining an equilibrium lattice parameter about 2.4% smaller than the experimental value.

TABLE 4.1

Calculated and experimental lattice constants and bulk moduli for fcc La.

	Lattice constant (Å)	Bulk modulus (kbar)	dB/dP
LMTO <sup>a</sup>	5.11	240.	3.0
LMTO <sup>b</sup>	5.17	280.	
X $\alpha$ <sup>c</sup>	5.20	139.	
X $\alpha$ <sup>d</sup>	5.32	261.	2.78
WIG	5.20	293.	2.66
HL	5.08	311.	2.99
expt. <sup>e</sup>	5.310	248.	2.8

<sup>a</sup>Ref. Glö78.

<sup>b</sup>Ref. McM81a.

<sup>c</sup>Present result, 5p treated as a core state.

<sup>d</sup>Present result, 5p treated variationally in a separate energy window.

<sup>e</sup>Ref. Sya75, room temperature data.

TABLE 4.2

Calculated total energy minimum  $E_{\min}$  and corresponding lattice parameter  $a_{\min}$  for three different XC potentials, the  $X\alpha$ , WIG, and HL form.

	$a_{\min}$ (Å)	$E_{\min}$ (Ry)
fcc La $X\alpha$	5.32	-16971.48874
fcc La Wigner	5.20	-16977.58850
fcc La H-L	5.08	-16982.10784
bcc La $X\alpha$	4.26	-16971.47908
bcc La Wigner	4.17	-16977.57799
bcc La H-L	4.07	-16982.09640

Table 4.3

Calculation for isolated La atom with three different XC potentials.

	$X\alpha$	WIG	HL
$R_{6s}$ (a.u.)	4.50	4.40	4.38
$R_{5d}$ (a.u.)	3.05	3.00	2.97
$-E_{6s}$ (eV)	2.31	3.33	3.37
$-E_{5d}$ (eV)	3.00	3.94	3.89
$E_{6s} - E_{5d}$ (eV)	0.69	0.61	0.52
$-E_{\text{atom}}$ (Ry)	16971.200	16977.242	16981.753
$E_{\text{coh}}$ (eV)	3.93	4.72	4.83

In view of the sensitivity of the results for fcc La to the particular XC potential used, it was of interest to perform calculations on bcc lanthanum for two reasons. First, to determine the total-energy difference between the two structures which must be overcome by the higher entropy of the bcc phase at the transition temperature and, secondly, to determine whether the calculated equilibrium properties of lanthanum in this structure display the same sensitivity to the form of the XC potential as found in the fcc phase.

As mentioned, the calculations for the bcc structure were carried out as much as possible in the same way as those for the fcc structure. The calculated total energies as a function of the volume are plotted in Fig. 4.3 along with fits to the Murnaghan equation of state. The resulting equilibrium properties are given in Table 4.4 along with the experimental lattice parameter at 1160K(Spe61). As far as we are aware, there have been no measurements of the bulk modulus of bcc lanthanum. From the results in Table 4.4 one might conclude that, as for the fcc phase, the agreement with experiment is best for the  $X\alpha$  calculation. We note, however, that the thermal correction, which is not included in our calculation, may, in fact, worsen this apparent agreement and improve the agreement with the results obtained using the other XC potentials. In any case, our results demonstrate that the degree of sensitivity to the



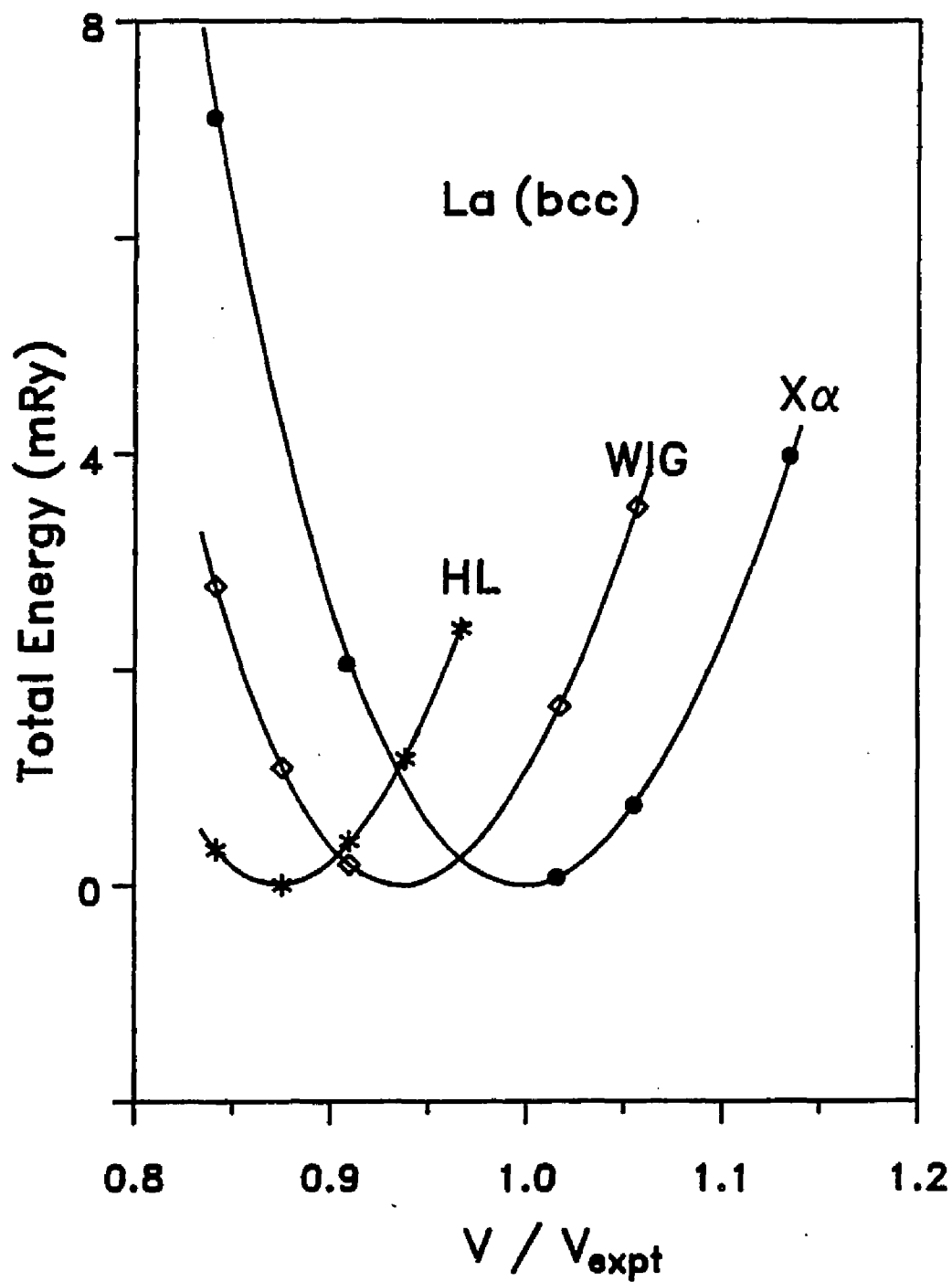


Figure 4.3 Calculated total energy -  $E_{\text{min}}$  vs. volume for bcc La and the Murnaghan equation of state fit.

particular choice of XC potential is very similar for the two phases. Following the argument given above for the sensitivity of the calculated properties of the fcc structure to the form of the XC potential, this is consistent with the very similar bulk moduli, atomic volumes, and  $d$  occupancies of La in these two structures. The calculated energy differences between the total-energy minima for the bcc and fcc phases are 9.1, 10.6, and 11.5 mRy for the  $X\alpha$ , Wigner, and Hedin-Lundqvist XC potentials, respectively. This implies an entropy difference in the range  $1.25 k_B$  to  $1.6 k_B$  at the transition temperature (with no temperature correction). The experimental value for this entropy change at transition temperature is  $0.67 k_B$  (Jay65), implying an energy difference of about 5 mRy between the two structures. We do not understand the source of this discrepancy.

TABLE 4.4

Calculated and experimental lattice constants and bulk moduli for bcc La.

	Lattice constant (Å)	$B_0$ (kbar)	$dB/dP$
$X\alpha$	4.26	272.	2.29
WIG	4.17	290.	2.64
HL	4.07	311.	2.91
expt. <sup>a</sup>	4.26		

<sup>a</sup>Ref. (Spe61), at 1160K.

#### 4.4 BAND STRUCTURE AND DENSITY OF STATES

The scalar-relativistic band structure of fcc lanthanum at the experimental lattice parameter calculated using the  $X\alpha$  XC potential is presented in Fig. 4.4 with the corresponding density of states (fully relativistic) in Fig. 4.5. This band structure is very similar to that obtained by Pickett *et al.* (Pic80), who also used an LAPW method with the  $X\alpha$  XC potential. The largest differences of about 16 mRy are in the  $f$ -band positions, which are listed with the widths in Table 4.5. The Fermi level lies near a  $d$ -like peak in the density of states, which we speculate may be related to the instability of the fcc structure to the dhcp structure at low temperature. The large peaks arising from the  $f$  bands lie 2-3 eV above the Fermi level, which agrees well with Pickett *et al.* (Pic80). In a pseudopotential calculation, which neglected the  $4f$  states, Wang *et al.* (Wan86) obtained phonon frequencies in good agreement with experiment, concluding that these states play, at best, a minor role in determining the properties of La. This is supported by the results of our calculation, which shows that the  $f$  bands are unoccupied and lie well above the Fermi energy. The density of states at the Fermi level is given in Table 4.6 along with the results of previous calculations (Glö78, Tak79, Pic80). In Figure 4.6, we show the charge density contour of fcc La calculated with the  $X\alpha$  potential at the experimental volume and compressed volume. One may notice

that the bonding charge is fairly small, which reflects the fact that La is soft.

TABLE 4.5

Band structure parameters (mRy) as defined in Pickett *et al.* (Pic80) for fcc La at  $a=10.0348$  a.u.

	Pickett	present
$C_F(\Gamma)$	159.	149.
$C_F(X)$	168.	152.
$W_F(\Gamma)$	86.	84.
$W_F(X)$	37.	36.

As far as we are aware, there have been no previous band structure calculations for bcc La. In Fig. 4.7 and 4.8, we show the semirelativistic band structure and the fully relativistic density of states of bcc La at the calculated equilibrium volume using the  $X\alpha$  XC potential. As in the fcc structure, the  $f$  bands lie about 2-3 eV above the Fermi energy, and thus have little influence on the structural properties. It may be noted from the band structure, that, unlike fcc lanthanum, in bcc lanthanum there are  $d$ -like bands with minima just below the Fermi energy at the  $N$  point and along the  $\Lambda$ -symmetry line. These give rise to a large peak in the density of states near the Fermi energy, and the nesting feature may lead to soft phonons near the  $H$  point (note the flat band just below  $E_F$  along the  $PN$ -symmetry line). Although there reportedly have been some

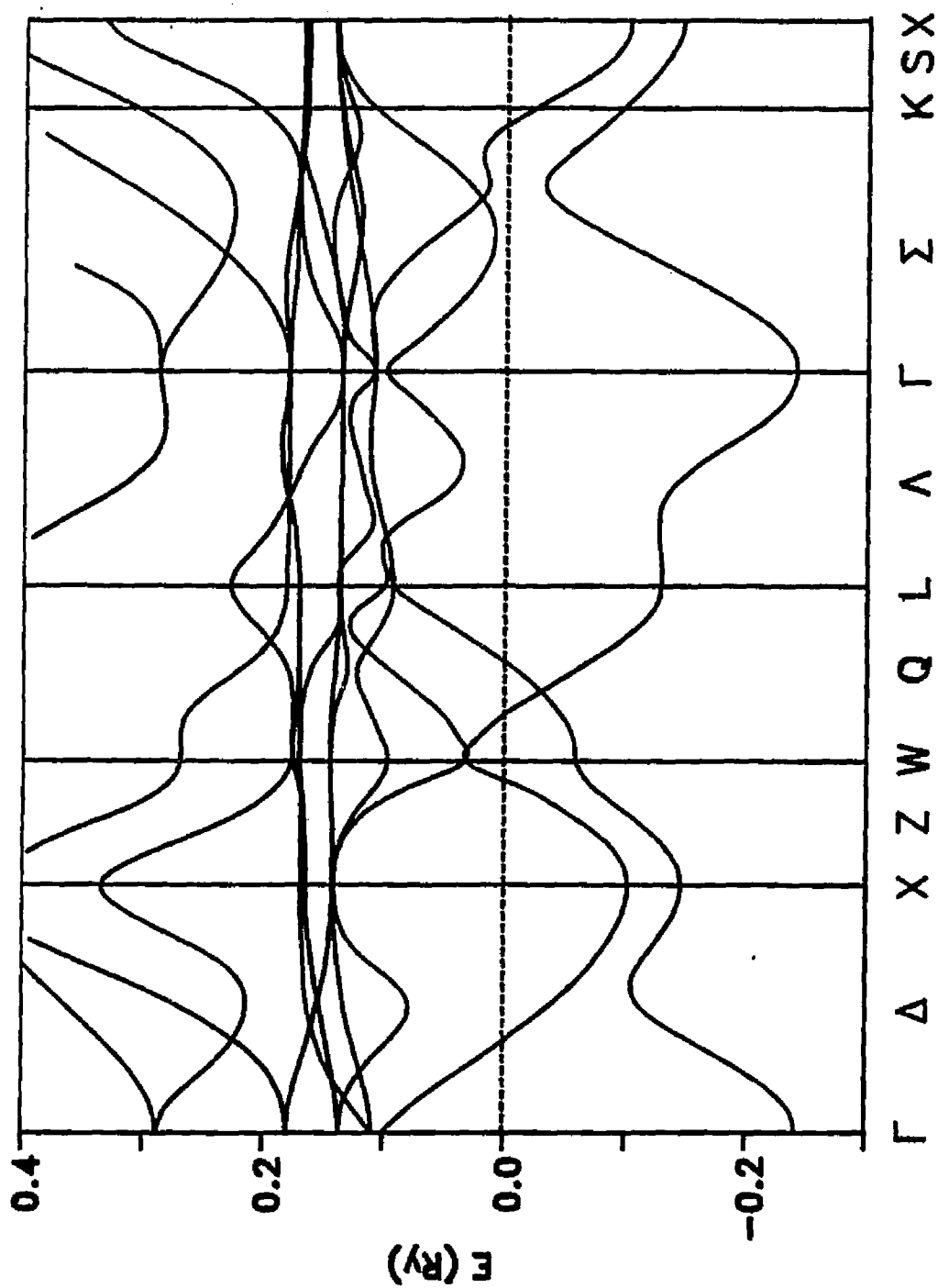


Figure 4.4. Semirelativistic band structure of fcc La at  $a=10.0348$  a.u. using  $X\alpha$  XC potential.

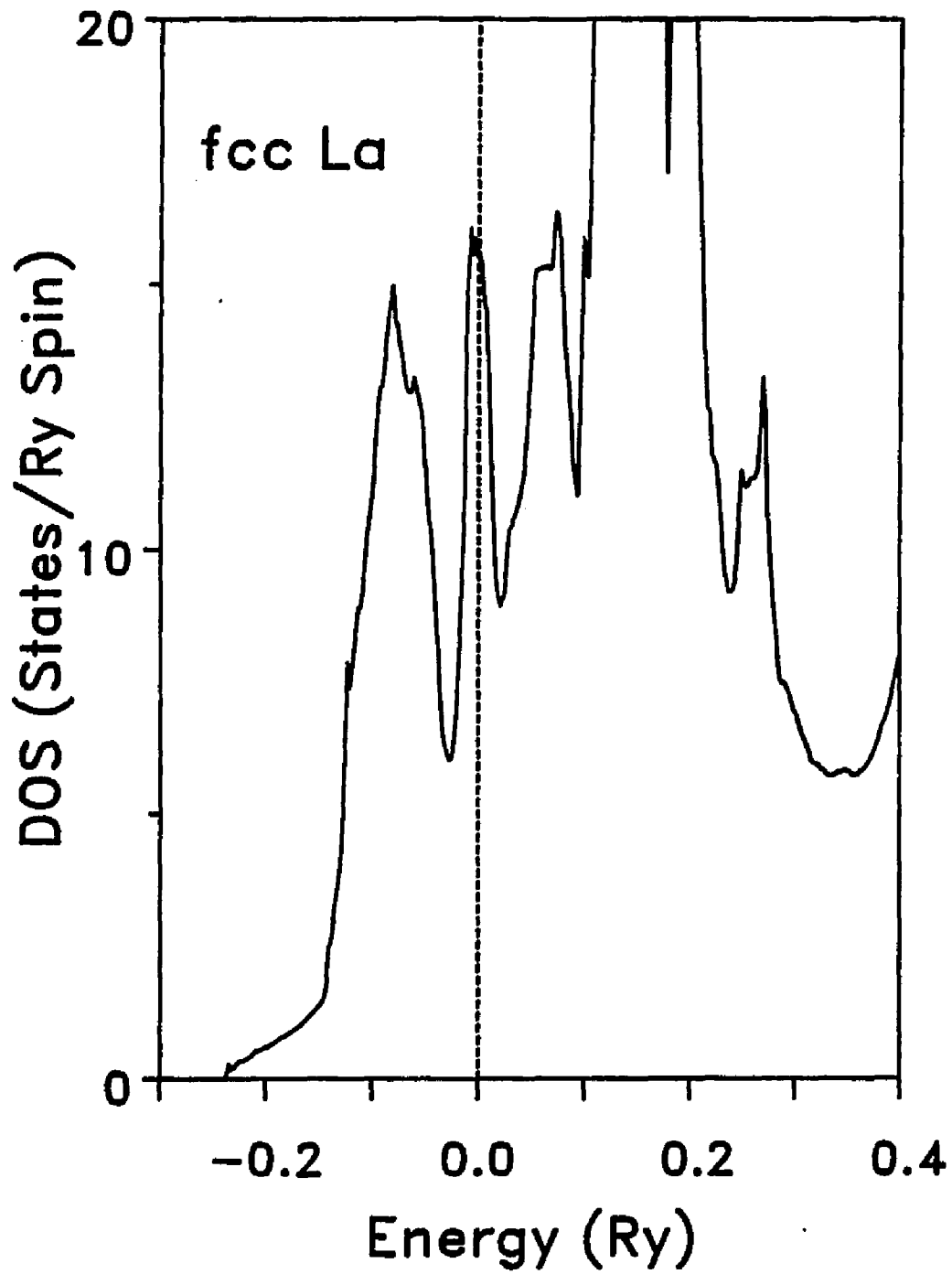


Figure 4.5 Density of states of fcc La at  $a=10.0348$  a.u. .

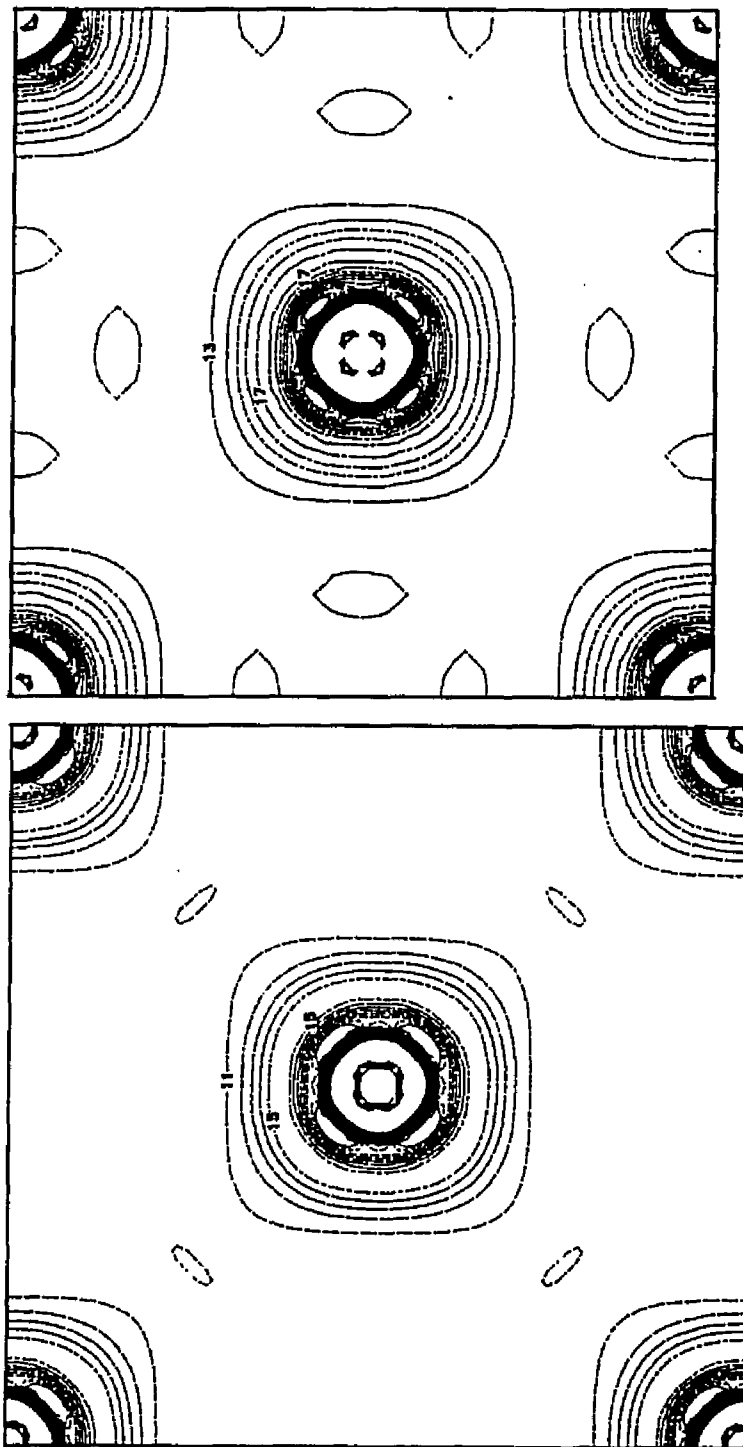


Figure 4.6 Charge density contours for fcc La ( $a=10.0348$  a.u. and  $a=9.476$  a.u.) calculated with the  $X\alpha$  XC potential in units  $10^{-3} e/a.u.^3$ ; the step size is 1.

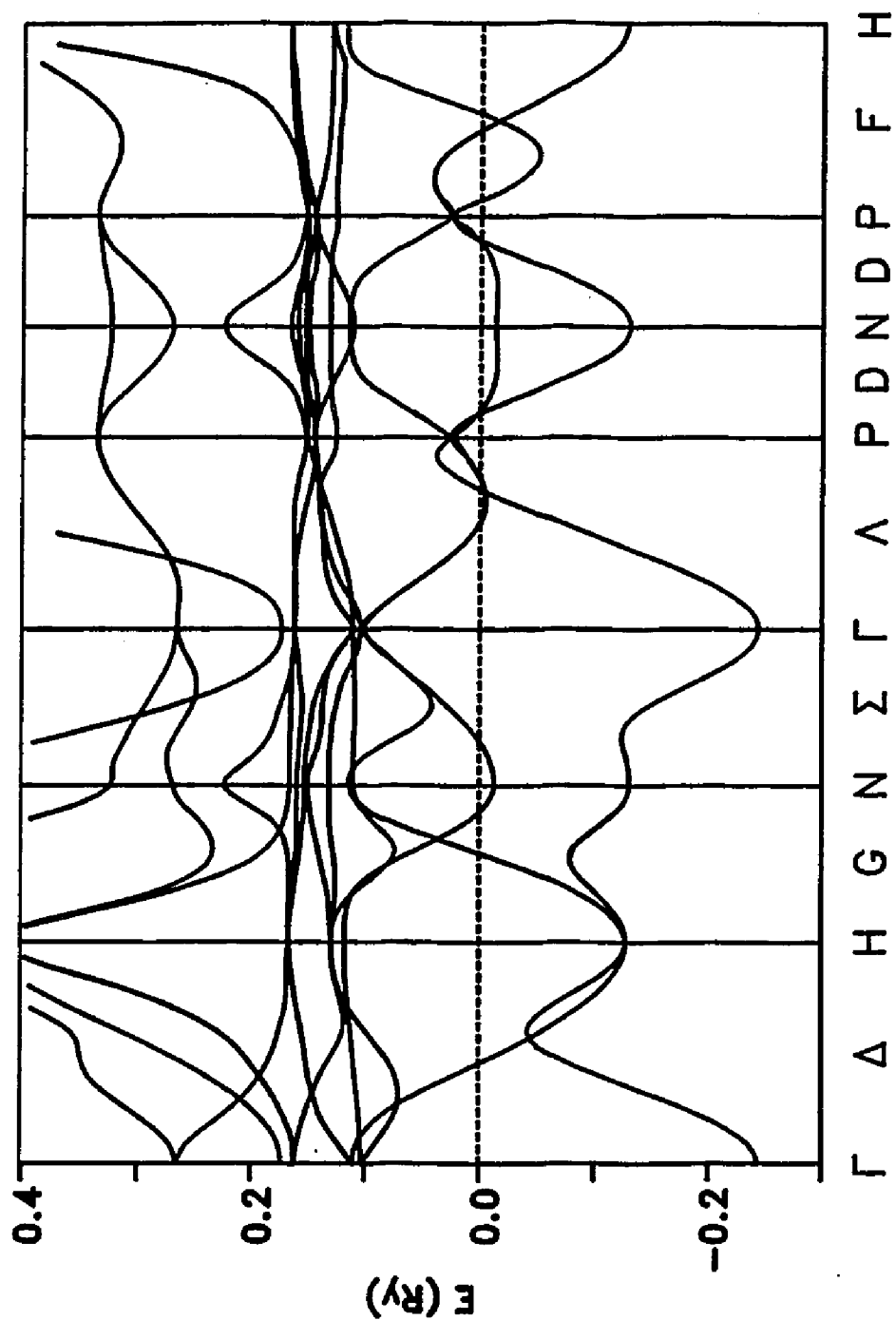


Figure 4.7 Semirelativistic band structure of bcc La at  $a=8.050$  a.u. using  $X\alpha$  XC potential.



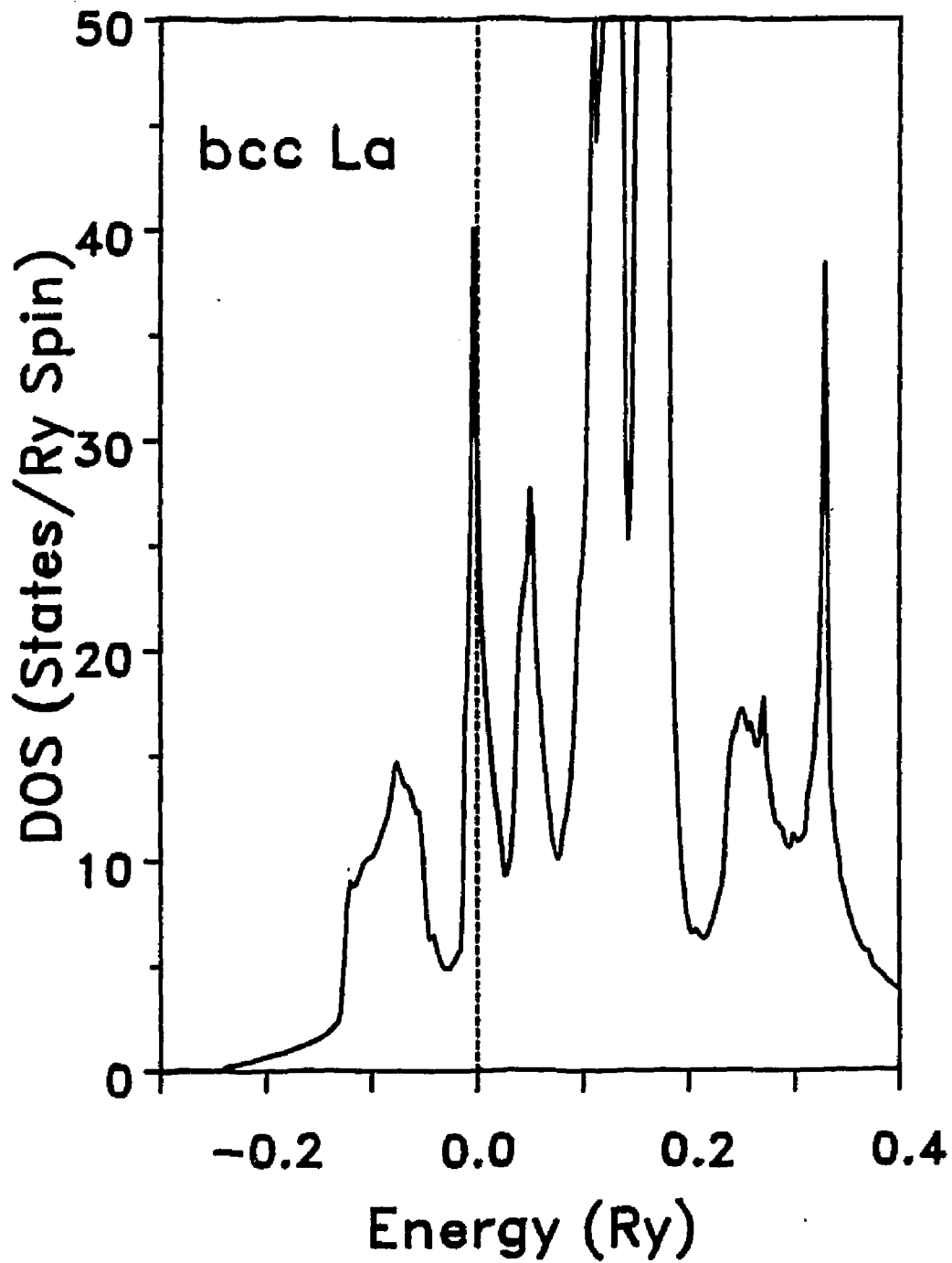


Figure 4.8 Density of states of bcc La at  $a=8.050$  a.u. (Note the change in the vertical scale from the fcc DOS).

neutron-scattering measurements(Sta84) of phonon frequencies along this direction, as far as we are aware no soft phonon has been observed at the  $H$  point. It seems plausible that this peak in the density of states of bcc La is responsible for its instability, and also that the related soft phonons are responsible for its higher entropy, leading to the phase transition at elevated temperatures. A similar phase transition (hcp to high-temperature bcc) is found in Zr. Chen *et al.* and Ye *et al.*(Che85,Ye87) have shown that in Zr strong interactions between the soft  $T_1$   $N$  point phonon and other low-lying (110) vibrational modes stabilize the high-temperature bcc phase. It would be of interest to perform total-energy calculations for the corresponding phonons in lanthanum in order to clarify this issue.

TABLE 4.6

Density of states ( states/Ry atom ) of fcc La at  $a=10.0348$  a. u. at Fermi Level  $N(E_F)$ .

	LMTO <sup>a</sup>	LAPW <sup>b</sup>	LAPW <sup>c</sup>	Present
$N(E_F)$	31.6	26	27.47	31.2

<sup>a</sup>Ref. Glö78.

<sup>b</sup>Ref. Tak79, at  $a=10.11$  a.u.

<sup>c</sup>Ref. Pic80.

#### 4.5 SUMMARY

We have reported total-energy and band structure calculation for fcc and bcc La. We find that the structural properties display considerable sensitivity to the particular exchange-correlation potential used. Among the three different forms we used, the  $X\alpha$ , Wigner, and Hedin-Lundqvist forms, the  $X\alpha$  form gives the best agreement with experiment for fcc La, the Wigner and Hedin-Lundqvist forms yielding smaller lattice parameters and larger bulk moduli.

## Chapter V

### LDA study of LaS and SmS

#### 5.1 INTRODUCTION

As a result of its computational tractability, the local density approximation (LDA) has made feasible accurate *ab initio* calculations of the structural and dynamical properties of a wide variety of real materials. In spite of the large number of applications in which LDA based methods have proved reliable there are indications that this approximation may not be adequate in some *f*-electron systems. In particular recent total energy calculations by Min *et al.* (Min86a) do not find any indication of the experimentally observed  $\gamma$ - $\alpha$  isostructural phase transition in Ce. This transition is believed to be a localization-delocalization transition of the *f*-electrons. In addition in Ce as well as in Eu and Yb (Min86b) accurate LDA based techniques have yielded equilibrium lattice constants considerably smaller than those observed. Calculations in which *f*-electron hybridization is suppressed yield values in better agreement with experiment implicating these states in the failure of the LDA.

Mixed valent SmS exhibits a strongly first order iso-structural phase transition(Jay70) at modest pressure ( 6.5 kbar ) which is believed to result from the delocalization and hence participation in bonding of the *f*-electrons under pressure. Thus this system may be a good one for characterizing the above mentioned failure of the LDA. While there have been some self-consistent band structure calculations(Str84,Lóp86a,Lóp86b) for SmS as far as we are aware there has been no detailed study of the applicability of the LDA to this material. Here we report LDA based calculations of the total energy of SmS as a function of the lattice parameter using a highly accurate general potential LAPW method. Parallel calculations were carried out with the Sm *f*-electrons treated in an atomic-like approximation thus suppressing their participation in the bonding in order to study the role these states play in the observed failure of the LDA.

## 5.2 STRUCTURAL PROPERTIES

The calculations reported here were carried out using a general potential LAPW method which has been discussed earlier. Both the valence and core electrons are treated relativistically (including spin orbit effects). In our calculation, we used the Hedin-Lundqvist(Hed71) exchange correlation potential. Because the 5*p* core states are quite extended in the rare earths it was necessary to treat these

as valence states in a separate energy window. Thus two energy windows were used, one for the valence electrons of Sm (La) and S and the other for the extended Sm (La) 5p core states. In order to establish the accuracy of our method in the absence of *f*-electrons a parallel calculation for the chemically similar compound LaS, which like SmS has a rock-salt structure, was carried out. In Fig. 5.1, we show the calculated total energy vs. volume for LaS, the solid line being a fit to the Murnaghan equation of state (Mur44). It is found that the calculated equilibrium lattice constant of 5.812 Å is within 1% of the experimental value of 5.860 Å (Vil85), the bulk modulus being 0.978 Mbar; as far as we are aware there have been no experimental measurements of the bulk modulus of LaS. The calculation revealed that the choice of the La *l*=1 linearization energy parameter in the valence window is rather important. We placed it around S 3s energy level. Placing this energy parameter near the Fermi level yielded a contracted equilibrium lattice constant (by more than 4%). This is because in this material the sulfur 3s state is fairly extended and has a significant *p*-like weight when expanded about the lanthanum site. Choosing an energy parameter near the Fermi energy expels this charge from the lanthanum spheres yielding an increase in the ionicity and therefore a contraction in the lattice parameter.

The calculations for SmS were carried out as much as

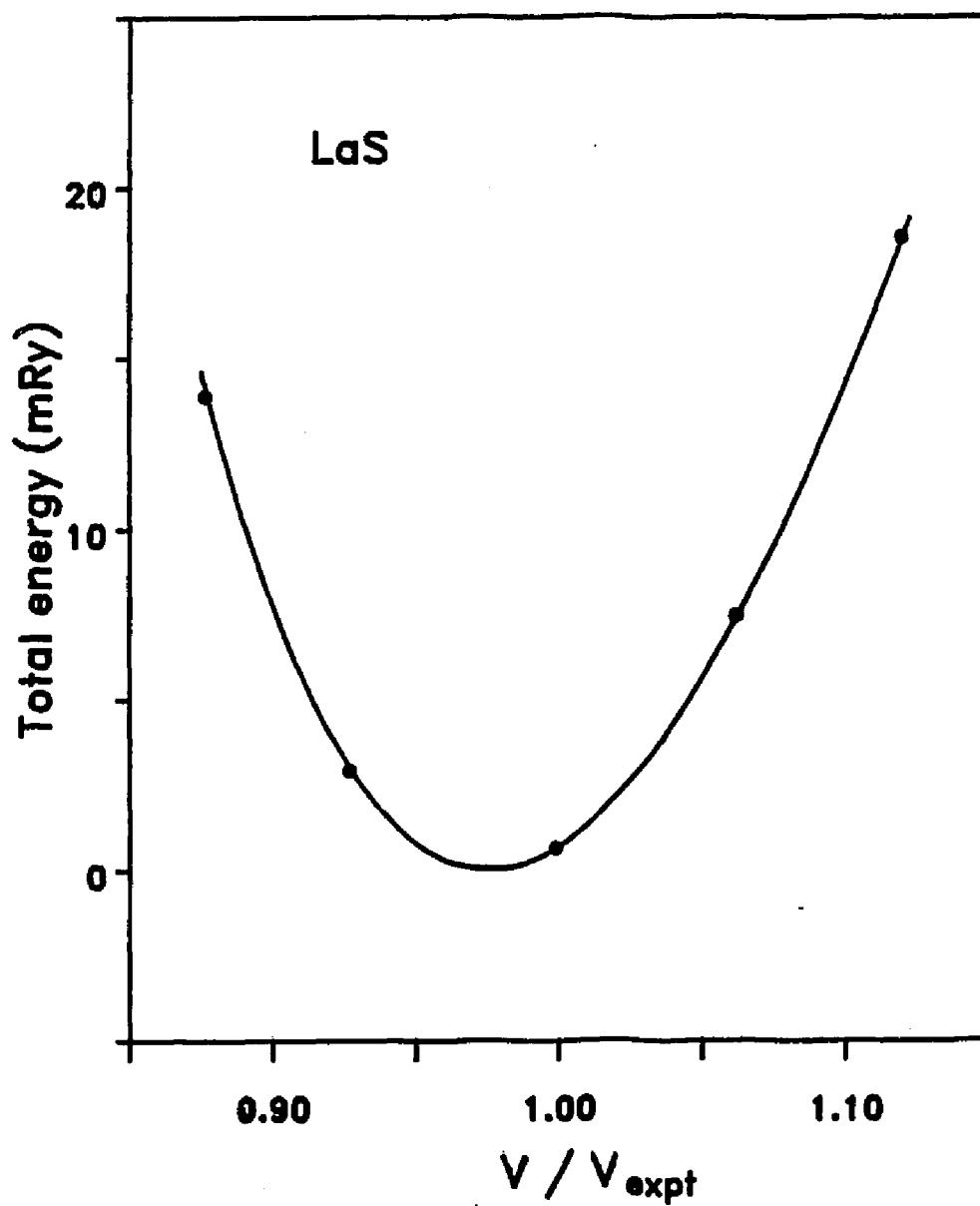


Figure 5.1. Calculated total energy + 17778.43550 Ry versus volume for LaS. The solid line is a fit to the Murnaghan equation of state.

possible parallel to those for LaS. The muffin tin radii used in the calculations are listed in table 5.1.

Table 5.1

Muffin-tin radii used in the calculations for S, La and Sm.

	S	La	Sm
$R_{\text{MT}}$ (a.u.)	2.20	3.00	2.50

We treated the Sm 5p states as band states in a second energy window. We placed the  $l=1$  linearization energy parameter  $E_l$  in the valence window around S 3s energy level as was done for LaS. Sixty special  $\bar{K}$ -points (Mon76) were used in performing the Brillouin zone summations yielding a total energy convergence of the order of  $10^{-4}$  Ry with respect to the number of  $\bar{K}$ -points. For LaS we used a basis set corresponding to  $RK_{\text{max}} = 8.6$ , where  $R$  is the smaller radius of that of the La's or S's; in this case, it is the S muffin tin radius; and  $K_{\text{max}}$  is the plane wave cutoff. For the volume range studied this cutoff yields between 280 and 380 basis functions. For SmS 290 to 700 LAPW basis functions were used corresponding to  $RK_{\text{max}} = 9.0$ . Calculations were performed using other basis set cutoffs in order to check the convergence of the calculations and it was found that the total energies were converged to within 1 mRy. The self-consistency was considered to be achieved when the



total energy was stable to  $10^{-5}$  Ry.

The total energy of SmS as a function of volume is shown in Fig. 5.2 and tabulated in Table 5.2. It may be noted that the calculated total energy of SmS is a smooth function of the volume with no evidence of two energy minima or even of an anomalous softening. Thus, there is no indication of the experimentally observed semiconductor to metal (black to gold) isostructural phase transition, which takes place at 6.5 kbar (Jay70) or at about 90% of the equilibrium volume, even though we have performed calculations at expanded volumes for which the d-f hybridization vanishes. The failure to predict this phase transition in SmS using LDA was also noted by Strange (Str84), though his calculation was not sufficiently self-consistent to yield reliable total energies. It is also consistent with the failure of LDA based calculations for Ce (Min86a), where no evidence of the experimentally observed  $\alpha$ - $\gamma$  was found.

The calculated total energy minimum in Fig. 5.2 occurs at a volume about 20% smaller than the experimental equilibrium volume. As shown in Table 5.3, the Murnaghan equation of state fit which was performed excluding the two points at highly expanded volumes yields an equilibrium lattice constant 7.6% smaller than the experimental value and a bulk modulus over 50% larger than the experimental value (Hai84) of 0.503 Mbar.

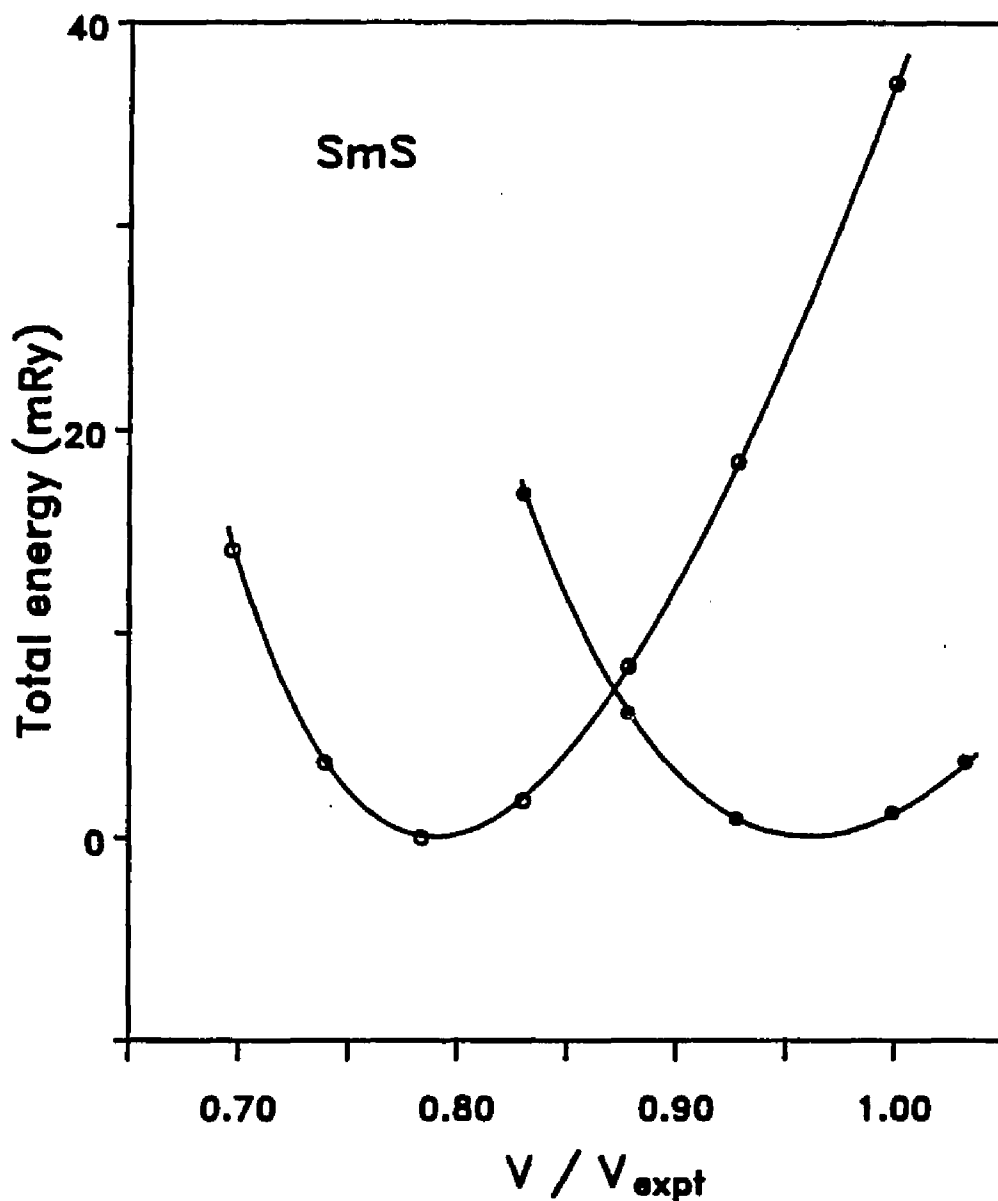


Figure 5.2 Calculated total energy -  $E_{\text{min}}$  Versus volume for SmS, open circles are for  $f$ -electrons treated as valence electrons  $E_{\text{min}} = -21650.71103$  Ry, while filled circles are for  $f$ -electrons treated as core electrons  $E_{\text{min}} = -21650.56872$  Ry (see text). The solid lines are fits to the Murnaghan equation of state.

TABLE 5.2

Calculated total energies + 21650 Ry versus lattice parameter for SmS ( $a_{\text{expt}} = 11.289$  a.u. ).

$a$ (a.u.) $f$ as valence	$E(a)$ (Ry)	$a$ (a.u.) $f$ as core	$E(a)$ (Ry)
10.000	-0.69688	10.600	-0.55191
10.200	-0.70733	10.800	-0.56260
10.400	-0.71100	11.000	-0.56780
10.600	-0.70918	11.276	-0.56751
10.800	-0.70260	11.400	-0.56502
11.000	-0.69253		
11.276	-0.67393		
12.400	-0.56754		
13.400	-0.46345		

TABLE 5.3

Equilibrium properties of SmS.

	SmS $f$ as valence	SmS $f$ as core	expt.
$a_0$ (Å)	5.515	5.887	5.974
$B_0$ (kbar)	843.	608.	503.
$B_0'$	4.9	4.2	2.4

Norman and Koelling (Nor87) have reviewed the band structure calculations for mixed valent systems. They point out that LDA based total energy calculations predict contracted lattice constants, indicating that the LDA overestimates  $f$  bonding. The LDA substantially overestimates the bulk modulus for  $\alpha$ -Ce (Glö83, Min86a) and TmSe (Jan85), but is in accord with experiment for  $UPt_3$  (Sti85). The present calculation demonstrates that the LDA significantly underestimates the lattice parameter and overestimates the bulk modulus for SmS.

As mentioned, it is thought that the underestimation of the equilibrium lattice constants in these systems is due to the LDA overestimating the extent of  $4f$ -bonding. Even though the calculated lattice parameter is closer to that expected for the metallic phase (Extrapolating the equation of state for metallic SmS of Ref. Jay70 to zero pressure yields an equilibrium volume about 11% smaller than that of the semiconducting state as compared to the LDA result of -20%) the LDA cannot be said to be describing this mixed valent state correctly. This is because a correct description of the mixed valent phase requires a correct description of the highly correlated  $f$ -electrons which the LDA fails to provide. This is reflected in the relatively poor equilibrium lattice parameter. It has been shown in Ce (Min86a), Eu and Yb (Min86b) that when the  $4f$  electrons are treated as core electrons, the calculated equilibrium lat-

tice constants (otherwise severely underestimated) are quite close to experiment. In order to determine whether this is also the case in SmS, we performed a total energy calculation with the 4f electrons treated as core electrons, i.e., we suppressed the 4f hybridization. The resulting total energies are listed in Table 5.1 and displayed in Fig. 5.2. This calculation yields an equilibrium lattice constant of 5.89 Å which is much closer to the experimental value of 5.97 Å. The calculated bulk modulus  $B=0.607$  kbar is only about 20% larger than experiment.

### 5.3 BAND STRUCTURE

Our calculated relativistic band structure for LaS at the experimental lattice parameter is shown in Fig. 5.3. The corresponding density of states (DOS), shown in Fig. 5.4, is similar to that obtained by Vlasov *et al.* (Vla85) using an independent self-consistent LAPW method. There is a low-lying S-3s band about 1 Ry below the Fermi energy,  $E_F$ , a higher S-3p band about 0.3 Ry below  $E_F$ , and a partially occupied La-5d band near  $E_F$ . The unoccupied La-4f bands lie above  $E_F$ . The calculated band structure and corresponding DOS for SmS at the experimental lattice parameter are shown in Figs. 5.5 and 5.6 respectively. An expanded view of the DOS near  $E_F$  is shown in Fig. 5.7. The S-3s and S-3p bands are similar to those in LaS, but the 4f-bands of Sm are now partially occupied. The band structure and DOS at a com-

pressed lattice parameter of 10.4 a.u. (which is near the calculated energy minimum of Fig. 5.1) is shown in Figs. 5.8 and 5.9. Comparing Figs 5.5 and 5.8, it is seen that as the volume is reduced the  $d$ - and  $f$ -bands become increasingly hybridized, and the  $f$ -bands become broader. Scalar relativistic calculations indicate that the spin-orbit interaction can alter the  $f$ -band positions by as much as 20 mRy. As mentioned, our total energy results implicate the  $d$ - $f$  hybridization in the isostructural phase transition, since we have shown that suppressing this hybridization yields an equilibrium lattice parameter near that of the semiconducting phase. The LDA results tend to overestimate the amount of hybridization, resulting in a contracted lattice parameter and no localization-delocalization transition. In view of this failure to correctly describe the  $f$ -electrons in SmS, the bands in Figs. 5.5 and 5.8 cannot be expected to provide reliable quasiparticle energies or dispersions.

It may be noted from Figs 5.5 and 5.8 that there is a considerable amount of  $d$ - $f$  hybridization even at the equilibrium volume. In order to investigate whether the LDA incorrectly predicates a phase transition when this hybridization diminishes at very large volumes we performed total energy calculations at two highly expanded volumes. We take the energy difference between the flat occupied  $f$ -band and the bottom of the  $d$ -band at the  $X$ -point as an indication of the amount of  $f$ - $d$  overlap. This "overlap" (Fig. 5.11) is

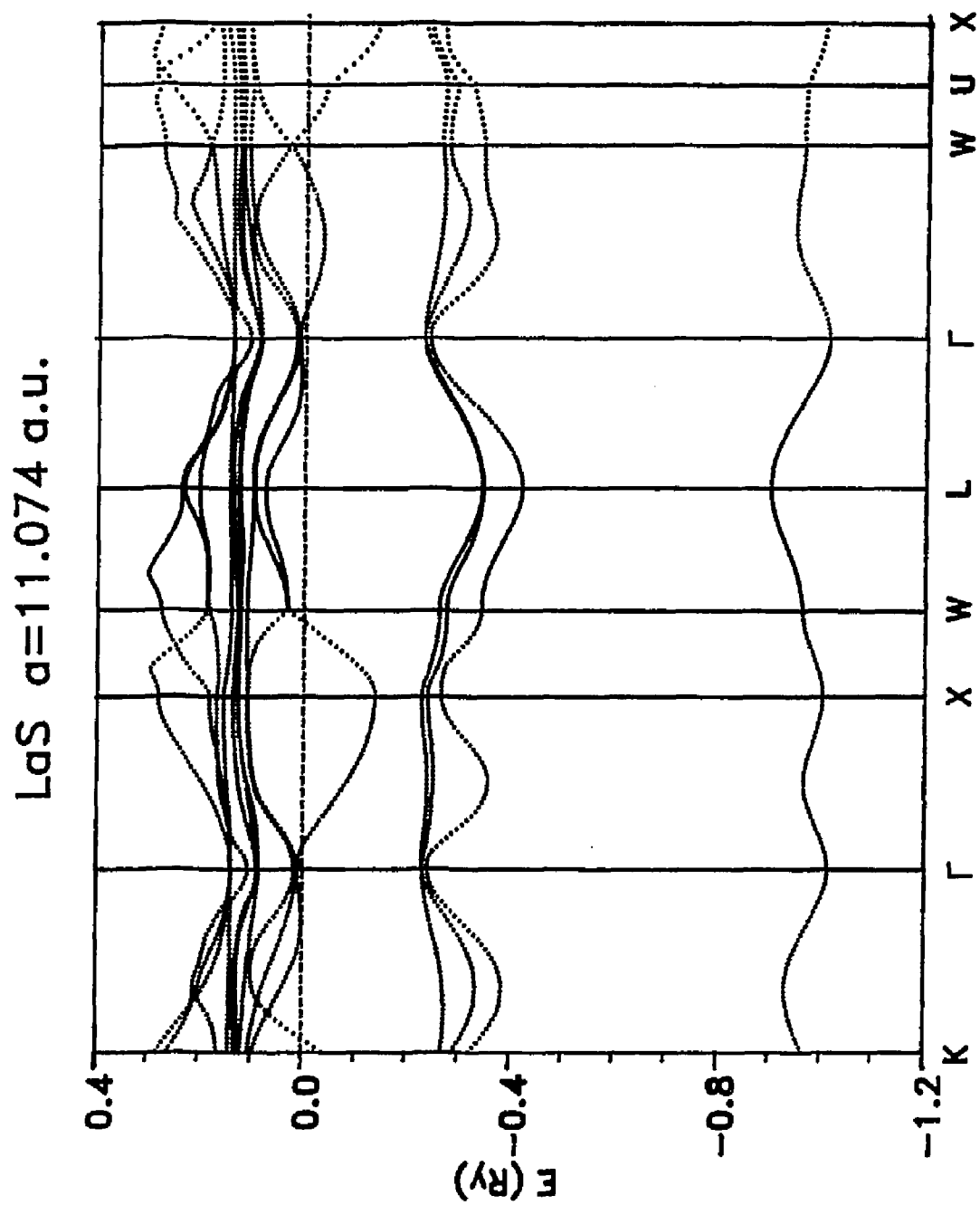


Figure 5.3 Band structure of LaS at the experimental volume, dashed line indicates the Fermi level.

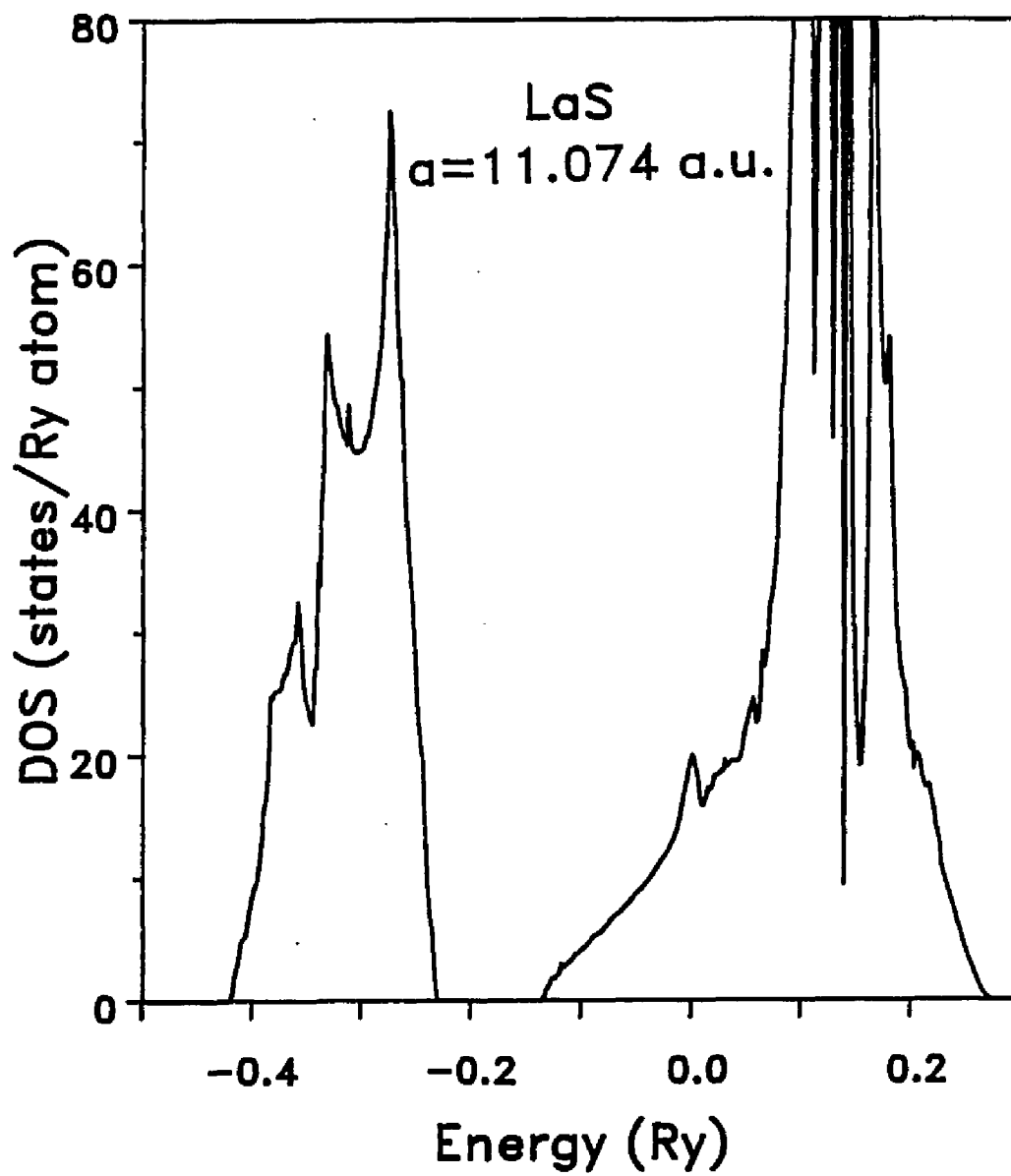


Figure 5.4 Density of states of LaS at the experimental volume.



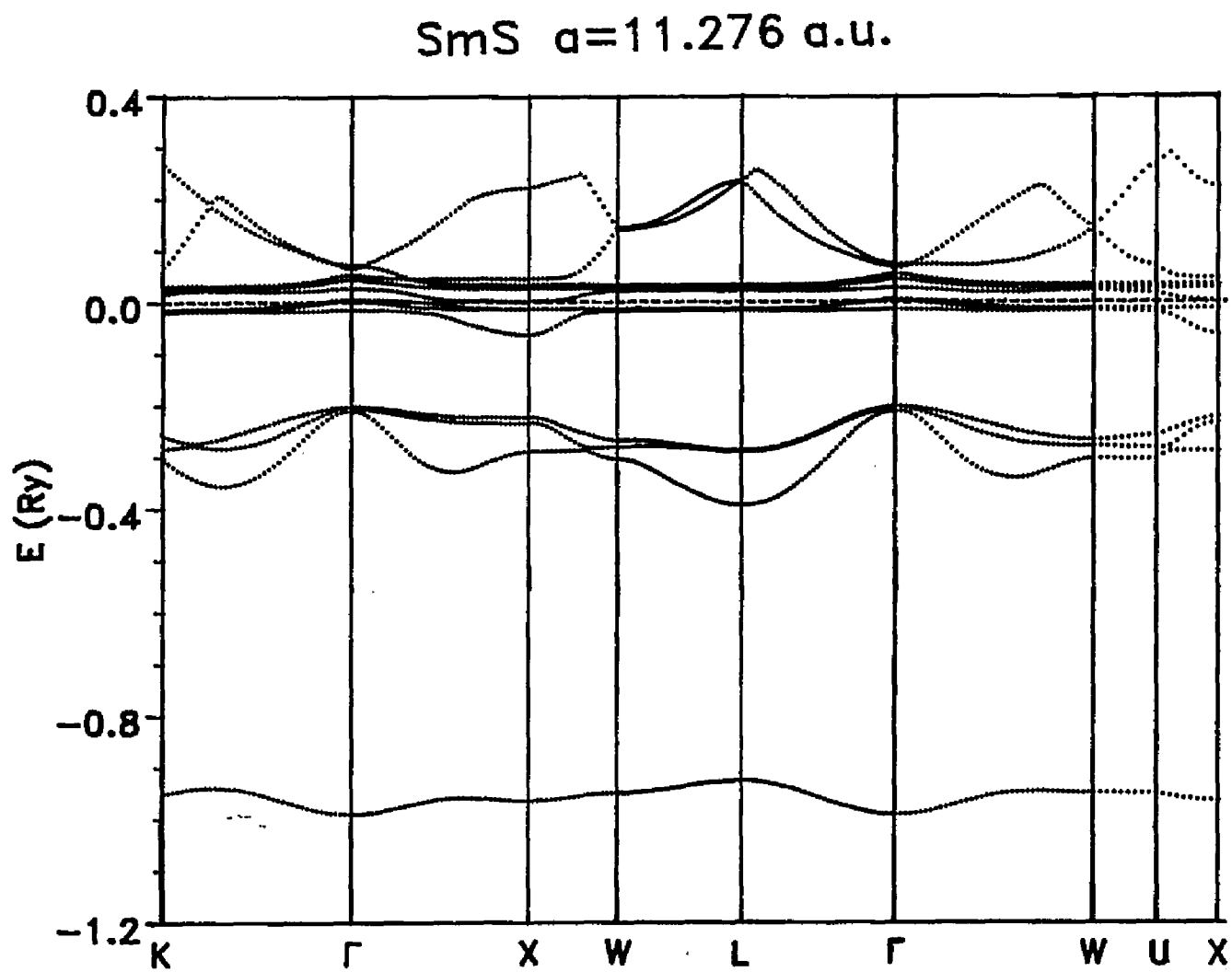


Figure 5.5 Band structure of SmS at the experimental volume.

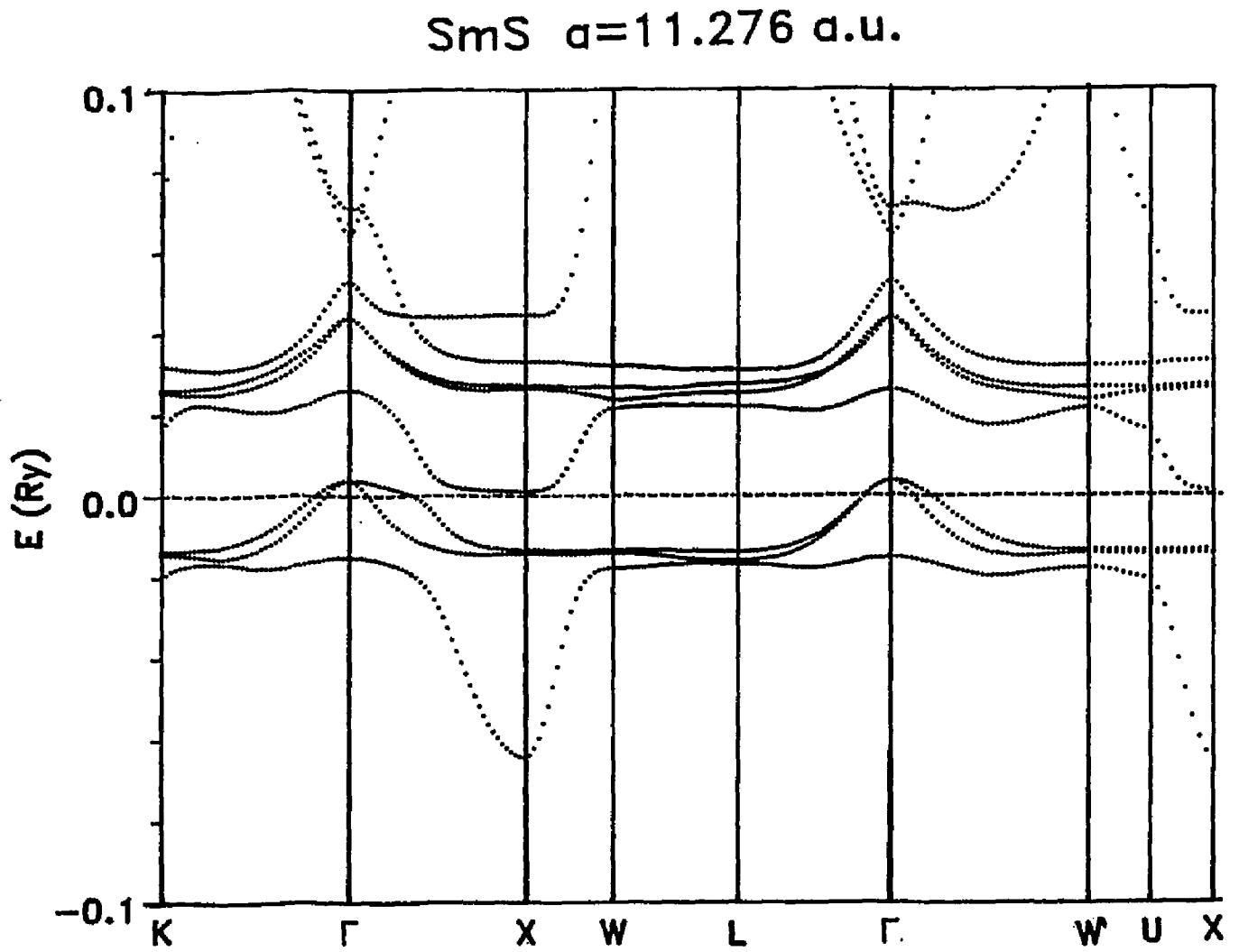


Figure 5.6 A detailed view of the band structure about the Fermi energy.

SmS  $a=11.276$  a.u.

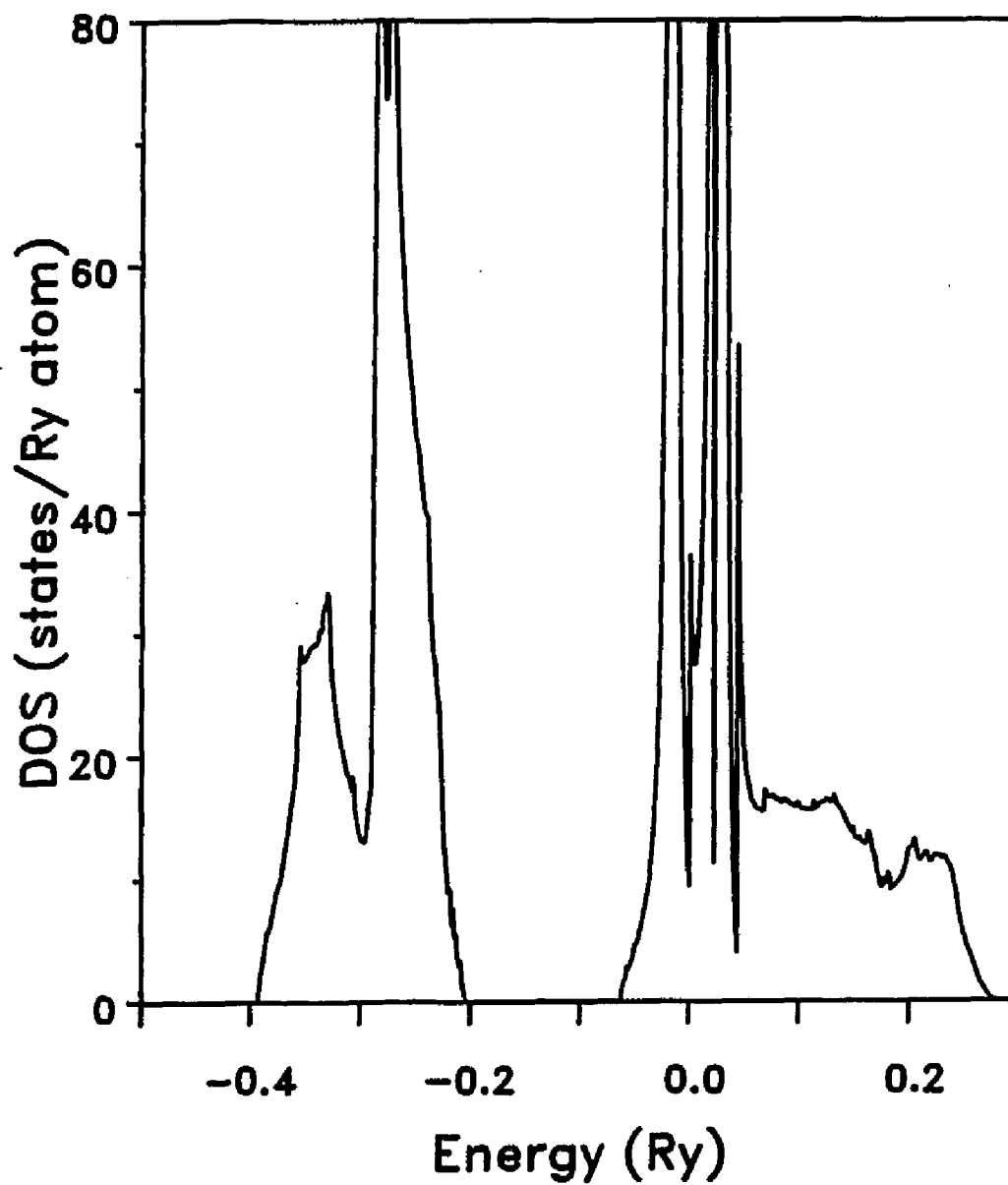


Figure 5.7 Density of states of SmS at the experimental volume.

SmS  $a=11.276$  a.u.

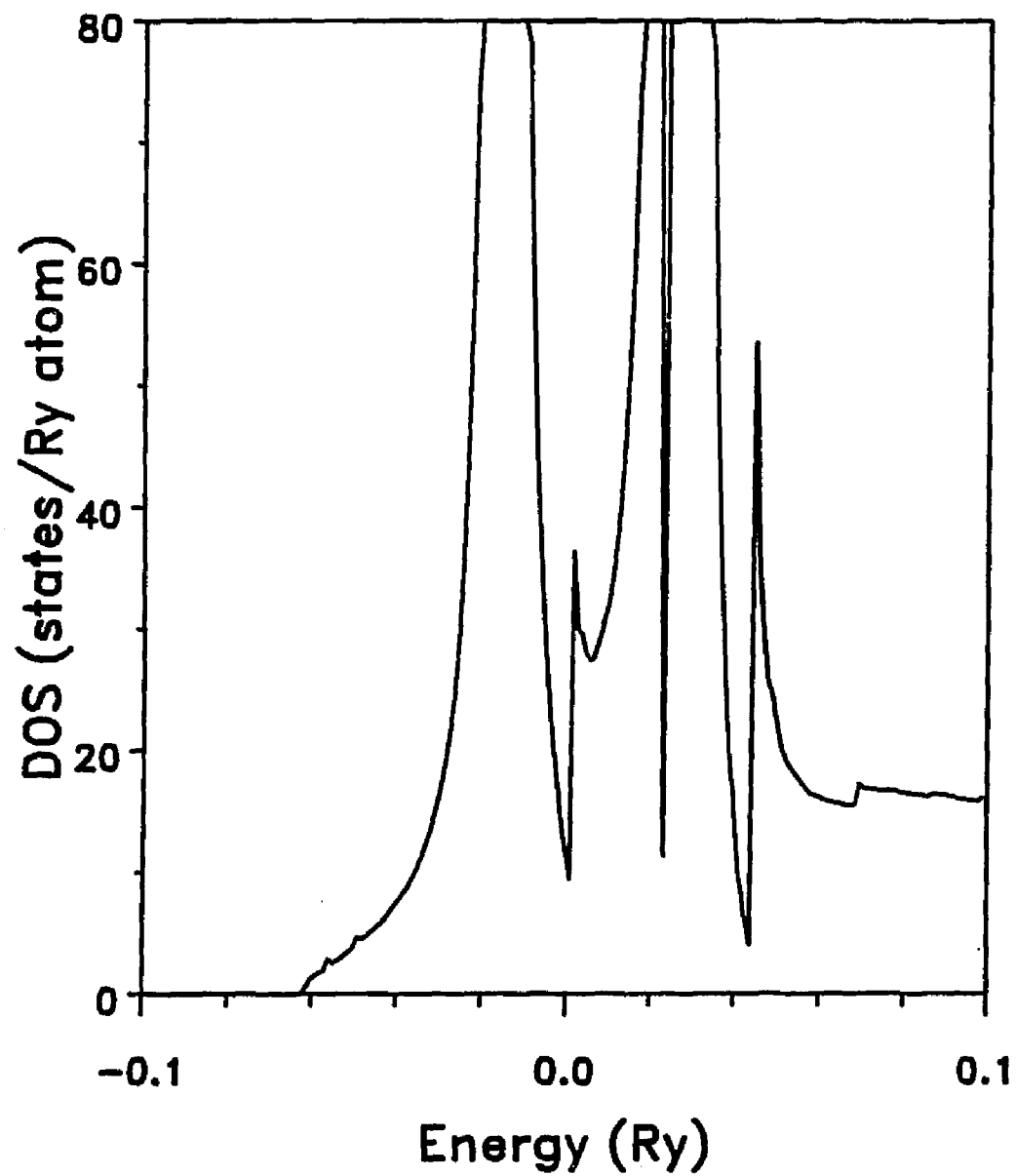


Figure 5.8 Detailed view of Fig. 5.6 about the Fermi energy.

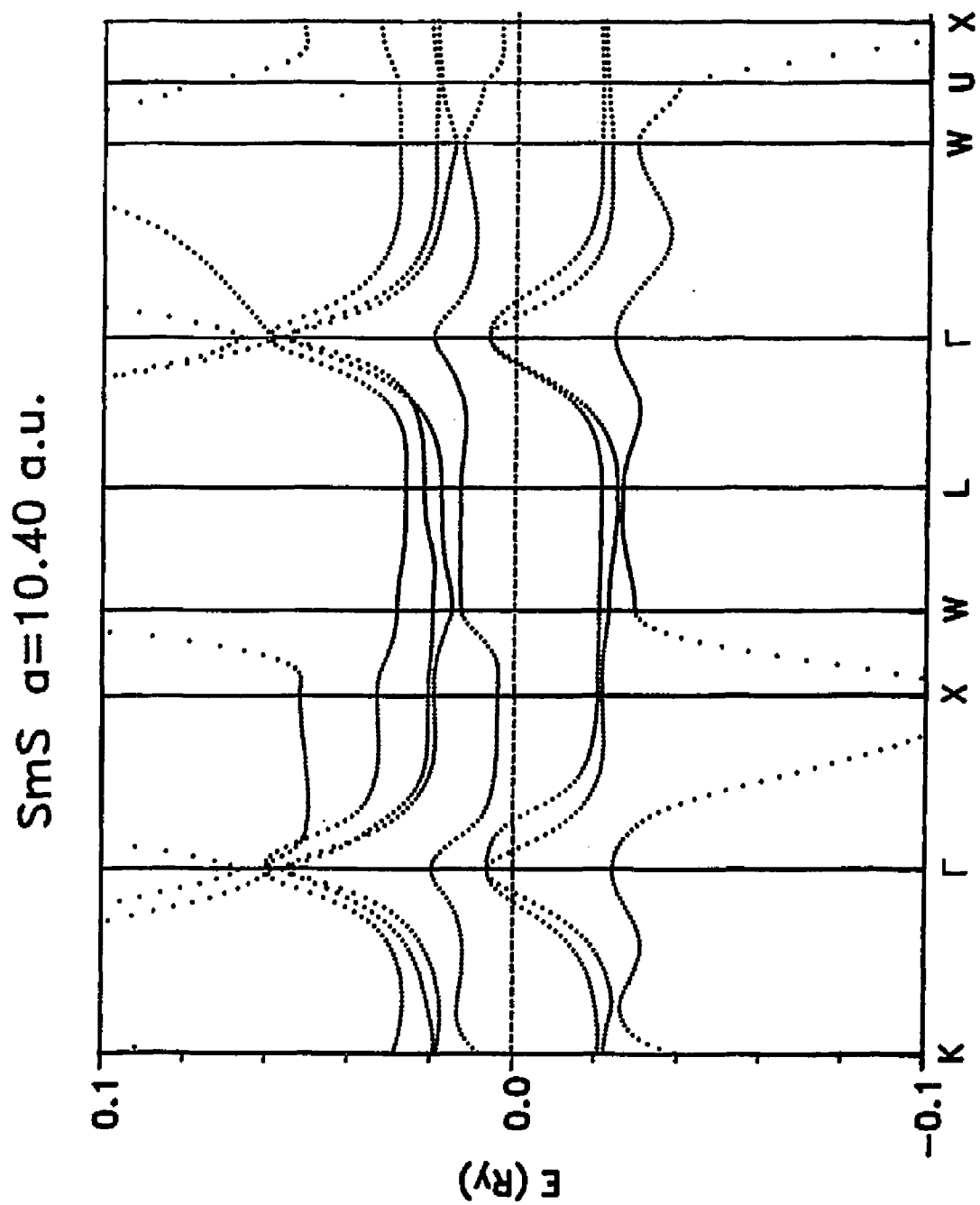


Figure 5.9 Detailed view of the band structure of SmS at  $a=10.40$  a.u..

SmS  $a=10.40$  a.u.

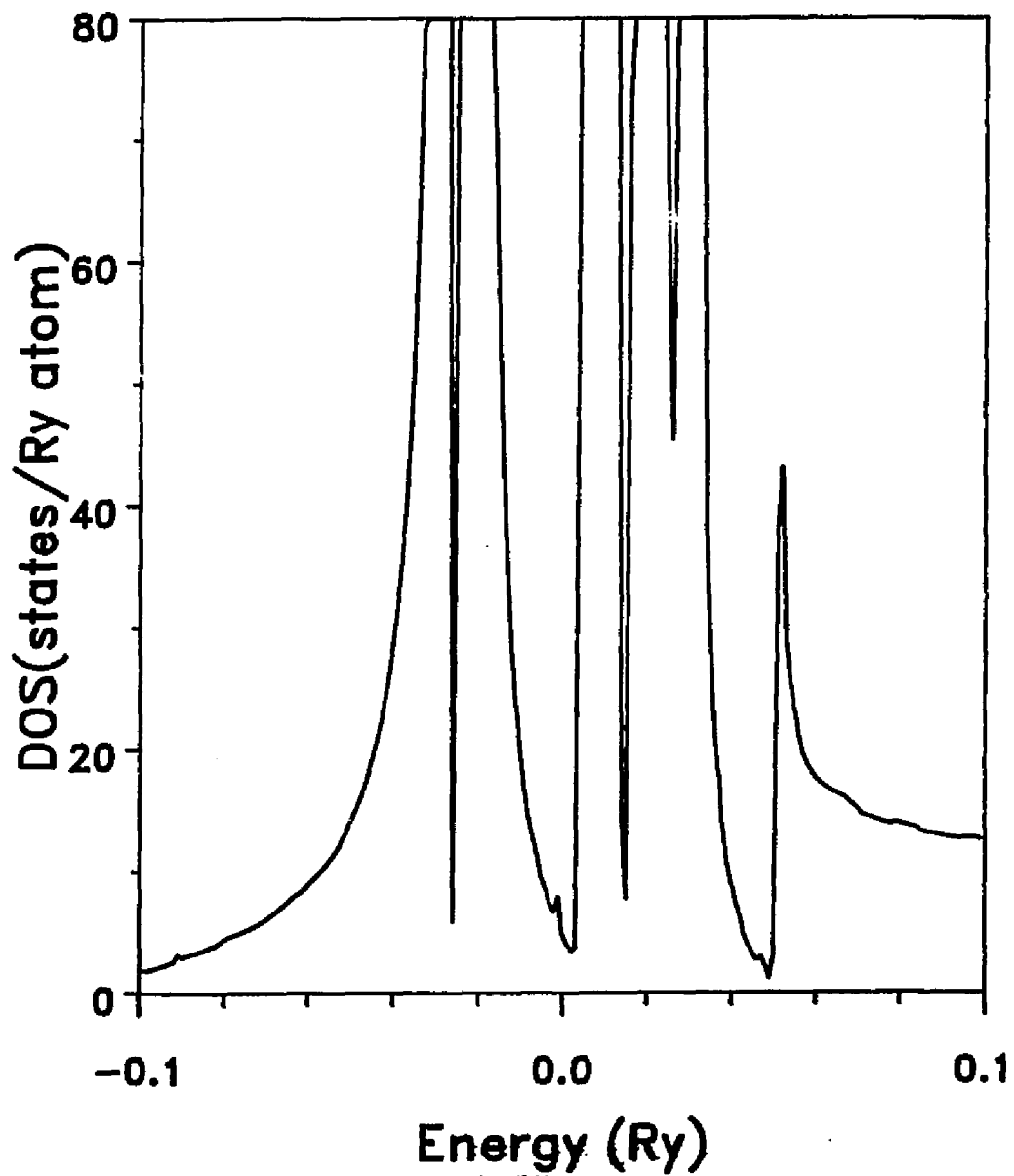


Figure 5.10 Detailed view of DOS about the Fermi energy at  $a=10.40$  a.u..

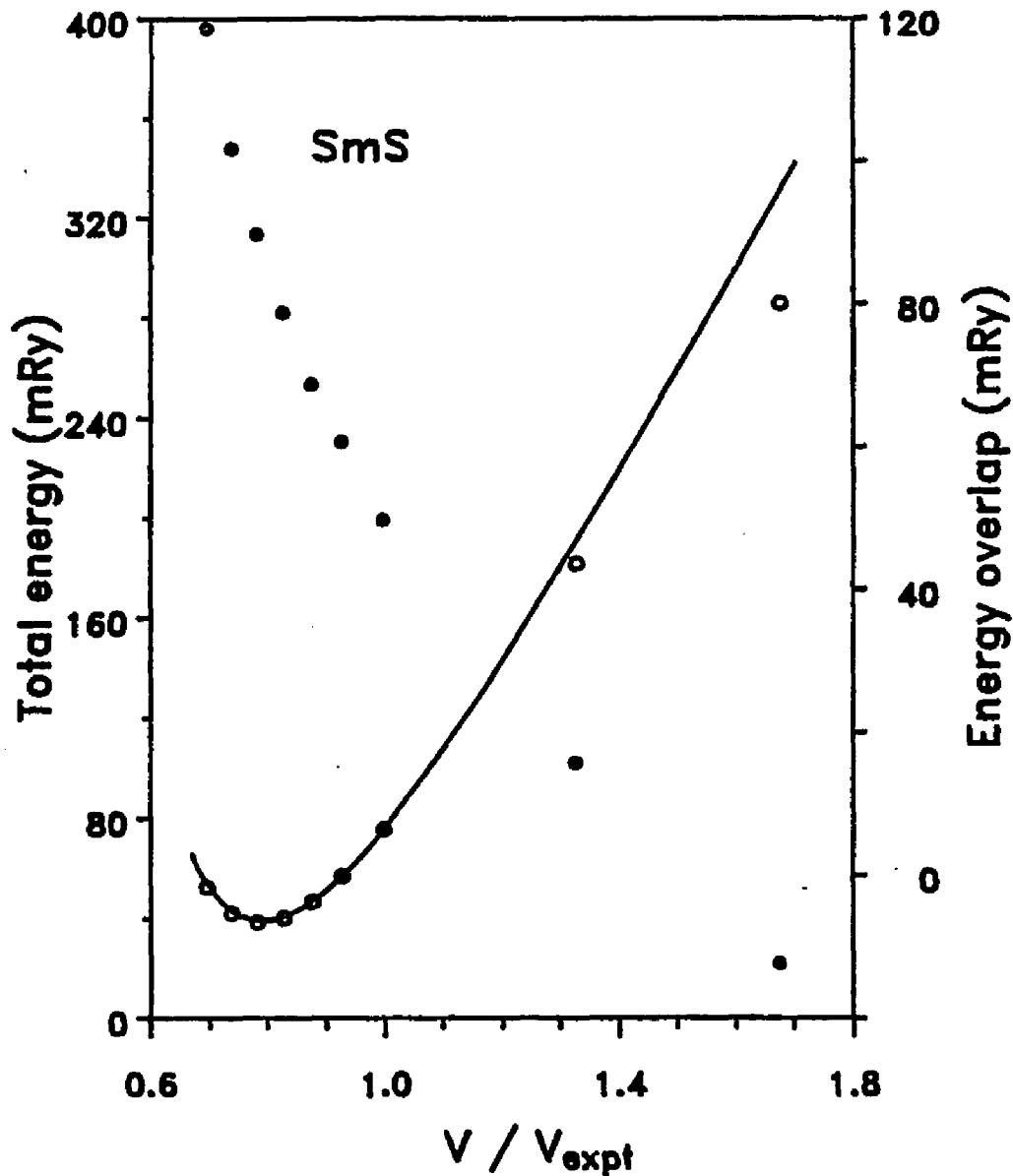


Figure 5.11 Variation of  $d-f$  overlap with volume as defined in the text. Total energy softens at larger volume but no indications of phase transition. The solid curve is the fit to the Murnaghan equation of state around the equilibrium volume and its extrapolation to large volume. The filled circles are for the overlap, the open circles are for the calculated total energy + 21650.75000 Ry.

plotted alongwith the total energies at large volumes and the Murnaghan equation of state fit ( See Fig. 5.2 ). At the largest volume studied this "overlap" vanishes, but there is still no indication of a phase transition.

#### 5.4 SUMMARY

We have reported total energy calculations on LaS and SmS using an LDA based LAPW method. We found that the LDA successfully predicts the equilibrium lattice constant of the non-*f*-electron system LaS. For SmS, the LDA underestimates the lattice parameter by 7.6%. Furthermore, we find no evidence for the experimentally observed isostructural phase transition in the calculated total energy curve. When calculations are carried out treating the localized 4*f* electrons as core electrons, thus suppressing the hybridization of 4*f* electrons, the equilibrium lattice constant is much closer to experiment and the otherwise severely overestimated bulk modulus is within 10% of the experimental value. This confirms that LDA overestimates the *f*-electron hybridization in this material.

Thus, we conclude that the LDA provides an inadequate description of the *f*-electrons in SmS.



## Chapter VI

### Total Energy Study of the Equation of State of HgTe and HgSe

#### 6.1 INTRODUCTION

The mercury chalcogenides, HgSe and HgTe, while having the same zero pressure structure as their zinc and cadmium analogues, differ from those materials in some important ways. As mentioned, at zero pressure both the mercury compounds and the corresponding zinc and cadmium compounds occur in a 4-fold coordinated zinc blende structure. Unlike the Zn and Cd chalcogenides which are semiconductors, the Hg compounds are semimetals. Moreover they transform at modest pressures to semiconducting 6-fold coordinated cinnabar phases (Mil81,For82). Under increasing pressure further transformations to metallic NaCl (6-fold coordinated) and  $\beta$ -Sn-like (6-fold coordinated) phases are observed (Wer83,-Hua83,Hua84). In the case of HgTe a distorted CsCl (8-fold coordinated) phase may also occur (Hua84). This sequence is in contrast to that usually found in zinc blende materials where the insulating 4-fold coordinated phase transforms to a 6-fold coordinated metal under pressure.

For these and other reasons, the Hg chalcogenides have been the subject of several recent experimental and theoret

ical investigations, and understanding what role the Hg-5d electrons play in determining the properties of these materials has been one of the important concerns. Photoemission experiments (She73, Ley74) indicate that the Hg, Cd, and Zn chalcogenides have a cation d-band in the valence band, and recent all-electron band structure calculations (Cad85, Wei88) yield a fully occupied d-band about 7-11 eV below the valence-band maximum. Wei and Zunger (Wei88) have noted the presence of important effects on the electronic and structural properties of the Hg, Cd, and Zn chalcogenides due to the cation d-band. The incomplete screening of the core by the d electrons is thought to be the origin of the very different properties of the IIB-VI compounds relative to the IIA-VI compounds.

Recent LDA based pseudopotential total-energy calculations (Yin80, Fro83) for group-IV semiconductors and for III-V compounds have accurately predicted their ambient pressure properties and the relative stability of the possible phases as a function of volume. However, a recent pseudopotential calculation for HgTe (Has87), in which the cation d-bands were ignored by assuming them to be a part of the chemically inert cores, has very large errors in the structural and cohesive properties, much bigger than the errors anticipated due to the use of the LDA or the convergence errors in the calculation. Here, we report the results of first-principle all-electron total energy calculations using the self-con-

sistent LAPW method. We calculate the energetics of ZnS, NaCl and  $\beta$ -tin structures and the phase transition pressures for both HgTe and HgSe. We also examine the extent to which the Hg d-electrons play a role in the pressure induced phase transitions by examining changes in the band structure, electronic density of states, and valence charge density.

## 6.2 CALCULATIONAL DETAILS

The Hedin-Lundqvist exchange-correlation potential was used. The calculations were iterated to self-consistency, which was considered achieved when the total energies were stable to  $10^{-5}$  Ry for the cubic zinc-blende and rocksalt structures, and to about  $5 \times 10^{-5}$  Ry for the body centered tetragonal  $\beta$ -Sn structure. For HgTe, the calculations were performed using muffin-tin sphere radii of 2.70 a.u. and 2.40 a.u. for mercury and tellurium respectively. A basis set cutoff of  $K_{\max}^2 = 13.44$  Ry was used. For HgSe, muffin-radii of 2.35 a.u. and 2.20 a.u. were used for mercury and selenium respectively with  $K_{\max}^2 = 16.00$  Ry. The Brillouin zone summations for HgTe (HgSe) were performed using 60 (28) special k-points (Mon76) for the semiconducting zinc-blende phase, 182 (60) special k-points for the metallic rocksalt structure and 240 (159) special k-points for the high pressure  $\beta$ -Sn structures of HgTe (HgSe). The total energies were converged to better than 1 mRy for zinc-blende and rocksalt phases with respect to  $K_{\max}$  and the Brillouin zone

sampling for both compounds, and to within about 2 mRy for the  $\beta$ -Sn phase. The densities of states were calculated using the tetrahedral method (Kle83,Jep84), using 195 uniformly distributed ab initio k-points for both ZnS and NaCl structures, and 244 for the  $\beta$ -Sn structure.

### 6.3 STRUCTURAL PROPERTIES

Calculations were performed for three different structures, namely, the equilibrium phase zinc-blende structure and the high pressure rocksalt and  $\beta$ -tin structures. No calculations were performed for the second semiconducting phase (hexagonal cinnabar structure), which exists in the range 14-80 kbar for HgTe (Mil81 ,Wer83) and 7.5-160 kbar for HgSe (For82,Hua84). It is straightforward to study the total energy change with respect to volume for the cubic phases (ZnS and NaCl) by varying the lattice constant. For the  $\beta$ -Sn structure, it was necessary to calculate the total energy as a function of both the c and a lattice constants. The similar procedure as in the case of hcp Ti and Zr was used. At a fixed volume, the total energy was calculated as a function of the c/a ratio, and then fitted to a quadratic or cubic to determine c/a at that volume. The total energy at this calculated c/a ratio was then taken as the energy at the volume in question, and these were used to obtain the equation of state. The sequence of the calculated total energy curves for the ZnS, NaCl, and  $\beta$ -Sn structures of both

HgTe and HgSe are displayed in Figure 6.1, and are in agreement with the experimental observations (Wer83,Hua84).

(a) ZINC BLENDE PHASE

The equilibrium structural properties were obtained by fitting to the Murnaghan equation of state, and are listed in Table 6.1 along with the results of previous LAPW (Wei88), linear muffin-tin orbital (LMTO) (Cad85) and pseudopotential (Has87) calculations and experiment (Cot74,Kum75,Mar82). The results of the all-electron calculations (LAPW and LMTO) generally agree with each other as well as with experiment. The cohesive energies were calculated by comparing the total energies of the solid and the results of spin polarized atomic calculations using the von Barth and Hedin exchange-correlation potential. Our calculated cohesive energy for HgTe is in better agreement with experiment than the earlier LAPW calculation (Wei88). The cohesive energies were overestimated by about 0.3 eV for HgTe and 0.8 eV for HgSe. This is attributed to the fact that the LDA underbinds atoms. The present calculations confirm that the spin-orbit interaction has little effect upon the structural and cohesive properties of HgTe ( $\Delta a < 0.002 \text{ \AA}$ ,  $\Delta B_0 < 10 \text{ kbar}$ , and  $\Delta E_c < 0.15 \text{ eV}$ ) in agreement with the results of earlier LAPW calculation by Wei and Zunger (Wei88). This contradicts the LMTO results of Cade and Lee (Cad85) who found that spin-orbit effects substantially reduce the lattice constant

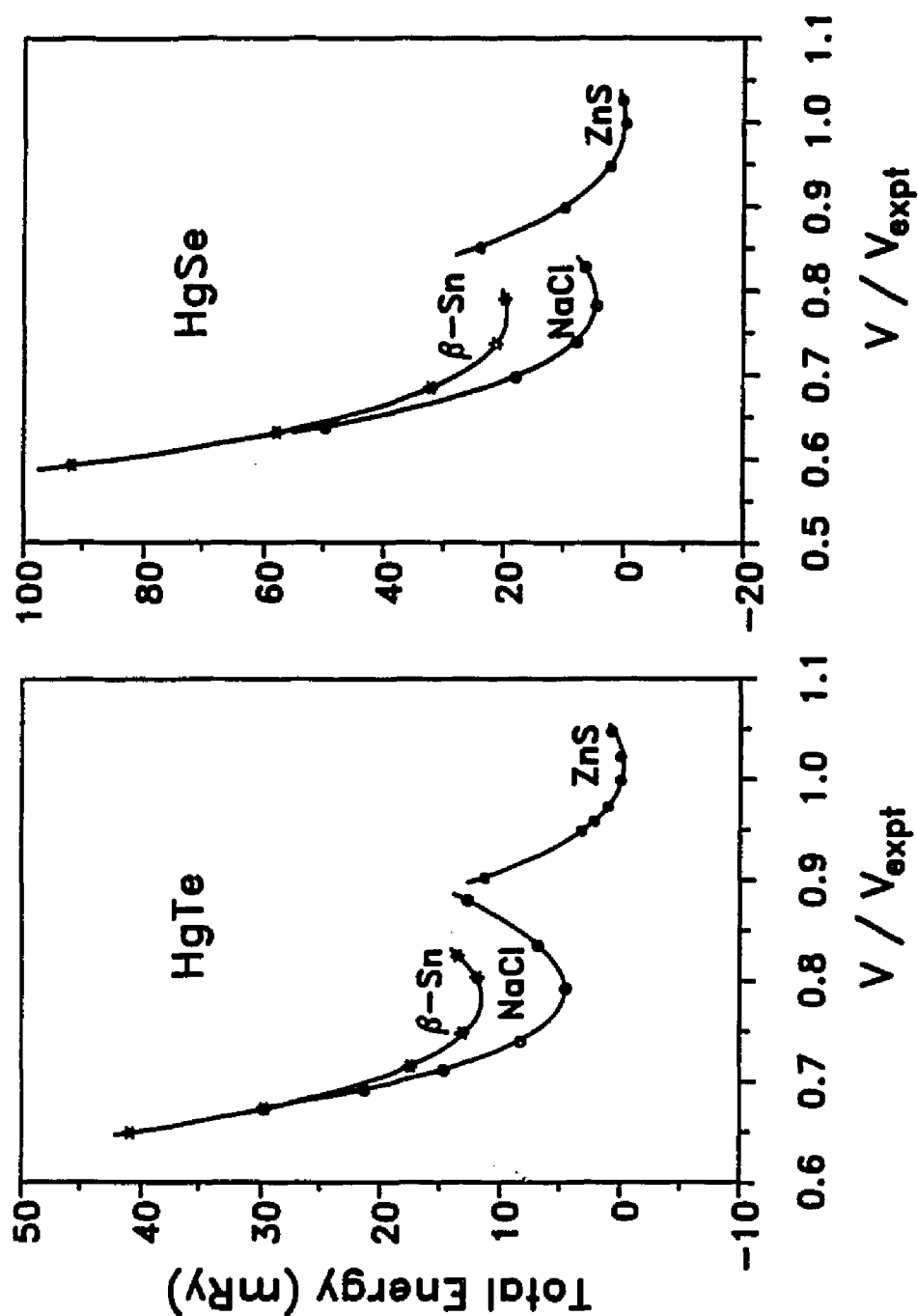


Figure 6.1 Fully relativistic total energy -  $E_{\text{min}}$  for HgTe and HgSe respectively, where  $E_{\text{min}}$  is the minimum energy of zinc-blende phase (-52884.14470 Ry for HgTe and -44155.92946 Ry for HgSe respectively).  $V_{\text{expt}}$  is the experimental equilibrium volume of 454.57 a.u.<sup>3</sup> for HgTe and 380.02 a.u.<sup>3</sup> for HgSe.

by 0.08 Å and increase the bulk modulus by 100 kbar. An earlier pseudopotential calculation (Has87) fails to accurately predict the structural and cohesive properties of HgTe, presumably because it ignored the Hg d-electrons, assuming them to be a part of the chemically inert atomic cores.

Table 6.1

Ground state (ZnS phase) properties of HgTe and HgSe.

HgTe					
Property	LAPW <sup>a</sup>	LAPW <sup>b</sup>	LMTO <sup>c</sup>	PS <sup>d</sup>	expt.
a (Å)	6.486	6.490	6.49	5.616	6.461 <sup>e</sup>
B <sub>0</sub> (kbar)	484.	456.	525.	47.	476. <sup>f</sup>
dB/dP	5.79		4.0		
E <sub>c</sub> (eV/pair)	3.50	4.57		7.05	3.22 <sup>g</sup>
HgSe					
a (Å)	6.091				6.084 <sup>e</sup>
B <sub>0</sub> (kbar)	590.				576. <sup>h</sup>
dB/dP	4.88				
E <sub>c</sub> (eV/pair)	4.17				3.37 <sup>g</sup>

<sup>a</sup>Present result.

<sup>b</sup>Ref. Wei88.

<sup>c</sup>Ref. Cad85.

<sup>d</sup>Ref. Has87.

<sup>e</sup>Ref. Mad82.

<sup>f</sup>Ref. Cot75.

<sup>g</sup>Quoted from Ref. Wei88.

<sup>h</sup>Ref. Kum75.

(b) HIGH PRESSURE PHASES

As in the case of the equilibrium ZnS phase, the calculated total energies as a function of volume were fit to the Murnaghan equation of state, the resulting parameters being given in Table 6.2. The similarities between HgTe and HgSe are apparent. Similar specific volumes of the total energy minimum 0.79 (0.79) for the NaCl structure and 0.78 (0.77) for  $\beta$ -Sn structure for HgTe (HgSe) and similar trends in the bulk moduli, and the pressure derivatives of the bulk moduli are found. The larger bulk modulus and energy difference between the minima for the two phases in HgSe is consistent with the fact that HgSe transforms from the NaCl to the  $\beta$ -Sn structure at about twice the pressure of the same transition in HgTe (Wer82,Hua84).

Table 6.2

Equation of state fits for the high pressure phases of HgTe and HgSe,  $E_{\min}$  are relative to that of the ZnS phase,  $V_{\text{expt}}$  are the equilibrium volumes of both materials.

	HgTe		HgSe	
	NaCl	$\beta$ -Sn	NaCl	$\beta$ -Sn
$V_{\min}$ (a.u. <sup>3</sup> )	359.69	355.33	299.47	293.84
$V_{\min}/V_{\text{expt}}$	0.79	0.78	0.79	0.77
$B_0$ (kbar)	663.	580.	804.	748.
$dB/dP$	5.21	4.82	4.80	4.96
$E_{\min}$ (meV)	4.54	11.5	4.56	19.3



Experimentally, semimetallic HgTe (HgSe) first transforms to a semiconducting cinnabar phase at 14 kbar (7.5 kbar), and then further transforms into a metallic NaCl structure at 80 kbar (160 kbar). The calculated transition pressures from the ZnS to the NaCl phases are about 5 kbar for both materials. These pressures are even smaller than the experimental transition pressure from the ZnS structure to the lower pressure cinnabar structure. In order to make the calculated transition pressures consistent with this, it would be necessary to increase the energy difference between the NaCl and ZnS minima by at least 10 mRy, much greater than our estimated convergence error of about 2 mRy. We do not understand the source of this discrepancy. Thermal effects, which we have not included in our calculations, could play a role, since the experiments were performed at room temperature, and our calculation is for zero temperature. Thermal effects, for example, lead to a decrease in the bulk modulus of HgTe (Mil81,Cot75) and HgSe(For82,Kum75) by 13% and 11% respectively as the temperature is raised from 0 K to room temperature. Still, this is a surprisingly large discrepancy. The calculated transition pressures from the NaCl structure to the  $\beta$ -Sn structure on the other hand, are in fairly good agreement with experiment. Table 6.3 gives the calculated transition pressures, experimental values (Wer83,Hua83,Hua84) and specific volumes of the both

NaCl phase and  $\beta$ -phase. For HgTe, a transition pressure of 134 kbar is obtained, which is within the experimental range of 120-170 kbar (Hua83). The calculated transition pressure was found to be rather sensitive to the convergence of the Brillouin zone sampling. For the  $\beta$ -Sn phase of HgTe, the total energy curve moves down almost uniformly by 2.5 mRy, when the number of special k-points was increased from 159 to 240, changing the transition pressure from 164 kbar to 134 kbar. Therefore the error for the transition pressure is about 30 kbar for HgTe. For HgSe, we used only 159 k-points. Assuming similar behavior, the calculated transition pressure may be in error by about 30 kbar based on the similarity between HgSe and HgTe.

Table 6.3

Transition pressure from the NaCl to the  $\beta$ -Sn phase for HgTe and HgSe and corresponding specific volumes (with respect to the equilibrium volumes).

	HgTe		HgSe	
	Calculated	Expt.	Calculated	Expt.
$P_t$ (kbar)	134.	120.-170. <sup>a</sup>	355.	280-330 <sup>b</sup>
$V_{\text{NaCl}}$	0.69	0.73 <sup>c</sup>	0.63	
$V_{\beta\text{-Sn}}$	0.67	0.73 <sup>c</sup>	0.61	

<sup>a</sup>Ref. Hua83.

<sup>c</sup>Ref. Wer83.

<sup>b</sup>Ref. Hua84.

Fig. 6.2 shows the calculated c/a ratio as a function

of volume for both HgTe and HgSe. The  $c/a$  ratio is found to change almost linearly with the volume for HgTe; the smaller the volume, the bigger the  $c/a$  ratio. However, unlike HgTe, the  $c/a$  ratio of HgSe is only weakly volume dependent and is approximately equal to 0.54. The calculated  $c/a$  ratios agree with experiment (Hua84) very well. At 28 °C, the  $c/a$  ratio for HgTe (at 170 kbar) is 0.538, and 0.532 for HgSe (at 404 kbar).

#### 6.4 Electronic Properties

The calculated scalar relativistic band structures for HgSe and HgTe in the equilibrium zinc blende structure are given in Fig 6.3, both at the experimental volume,  $V_{\text{expt}}$  and at a reduced volume of  $0.90 V_{\text{expt}}$ . The band structures contain a low lying chalcogen-s derived band about 12-14 eV below the valence band maximum (VBM), a fairly narrow set of Hg-d derived bands 7-8 eV below the VBM, which broaden slightly under pressure, and a set of "valence" bands derived primarily from bonding and antibonding combinations of Hg-s and chalcogen-p states. The fully relativistic densities of states (DOS), corresponding to these band structures, are given in Fig. 6.4. It may be noted from these that the Hg-5d bands broaden somewhat when the spin-orbit interaction is included. In Fig. 6.5 chalcogen-p and Hg-d projections of the fully relativistic DOS of Fig. 6.4 are presented. From the DOS it is apparent that there is a significant amount of Hg-d chalcogen-p hybridization all the

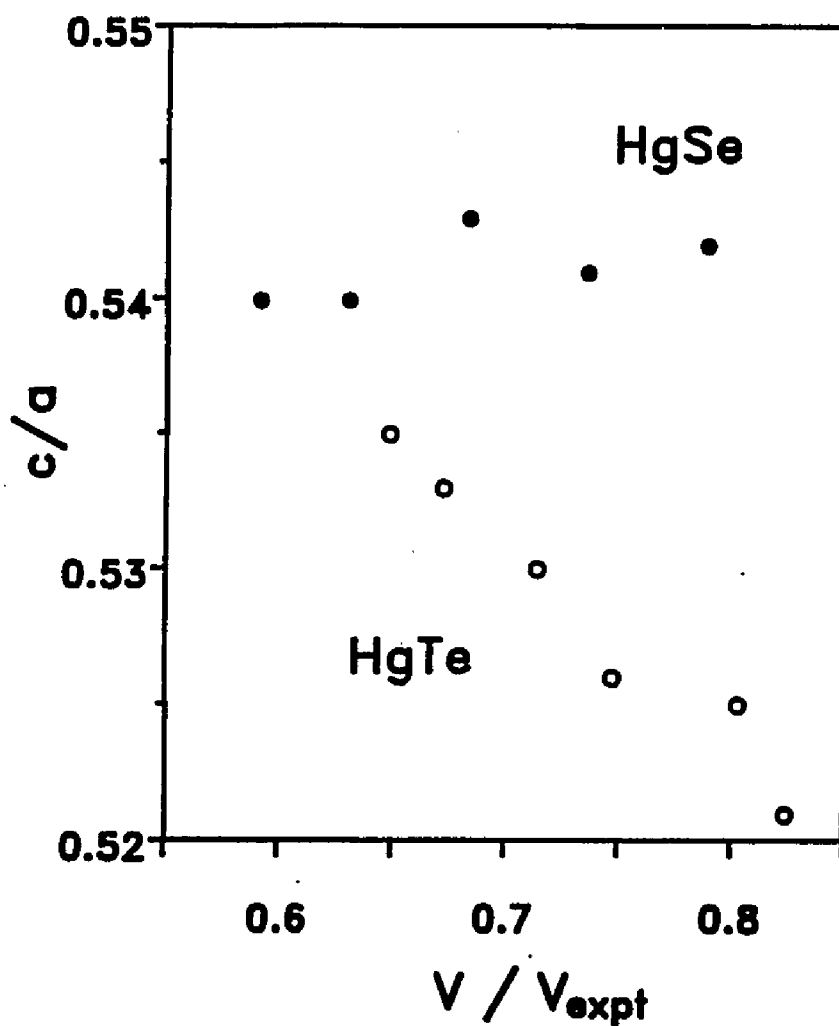


Figure 6.2 The volume dependence of the  $c/a$  ratio for the high pressure  $\beta$ -Sn structure. The  $c/a$  ratio of HgTe decreases almost linearly with volume, while for HgSe, it is almost a constant.

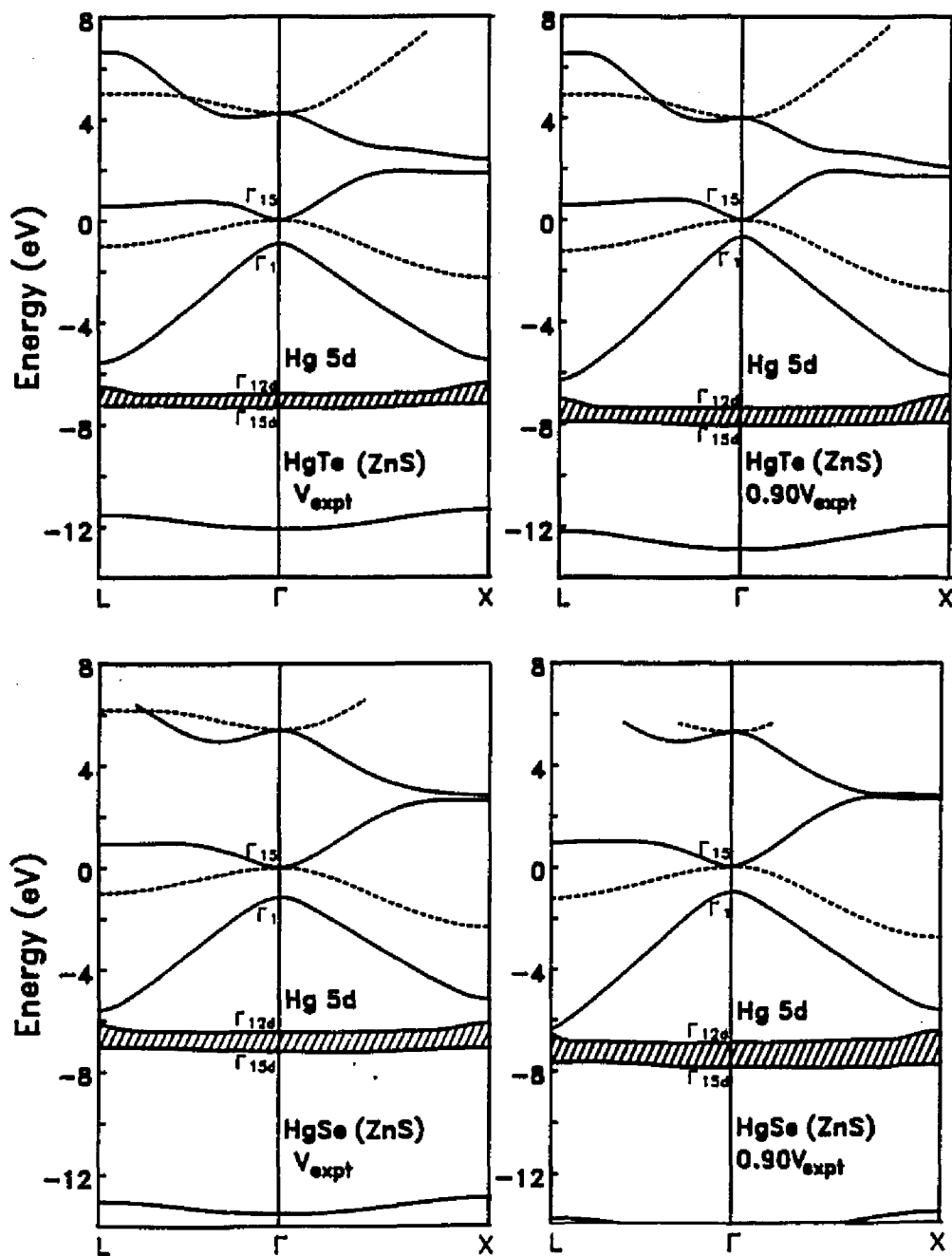


Figure 6.3 Scalar relativistic band structure for ZnS structure HgTe and HgSe at equilibrium volume and 90% of equilibrium volume. Dashed lines denote doubly degenerate states.

way up to the VBM. In view of this it is not surprising that the pseudopotential calculation of Hass and Vanderbilt (Has87) yielded results in relatively poor agreement with experiment since in that calculation the possibility of hybridization with the Hg-d states was excluded from the outset. The role of the Hg-d states should not be exaggerated however. As may be noted from the NaCl-structure scalar relativistic band structures of Fig. 6.6 and the DOS and projected DOS of Figs. 6.7 and 6.8 there are only relatively minor changes in the d-bands in going from the zinc blende structure to the NaCl structure. In particular it may be noted that there is little change in the d-band DOS through the transition apart from a slight broadening attributable to the smaller volume in the NaCl phase. The calculated electronic DOS for the high pressure  $\beta$ -Sn phase (see Figs. 6.9 and 6.10) demonstrates that even at these high compressions the d-band peak remains well below the Fermi energy, broadening only moderately. The extent of p-d hybridization also appears to be relatively unchanged through the various phase transitions. The d-bands are therefore relatively passive participants. While they play an important role through their hybridization with the chalcogen-p states which in turn determine the crystal structure, the d-bands themselves are relatively inert through the sequence transitions. It may be noted that the chalcogen-s states remain well separated from the other bands under pressure,

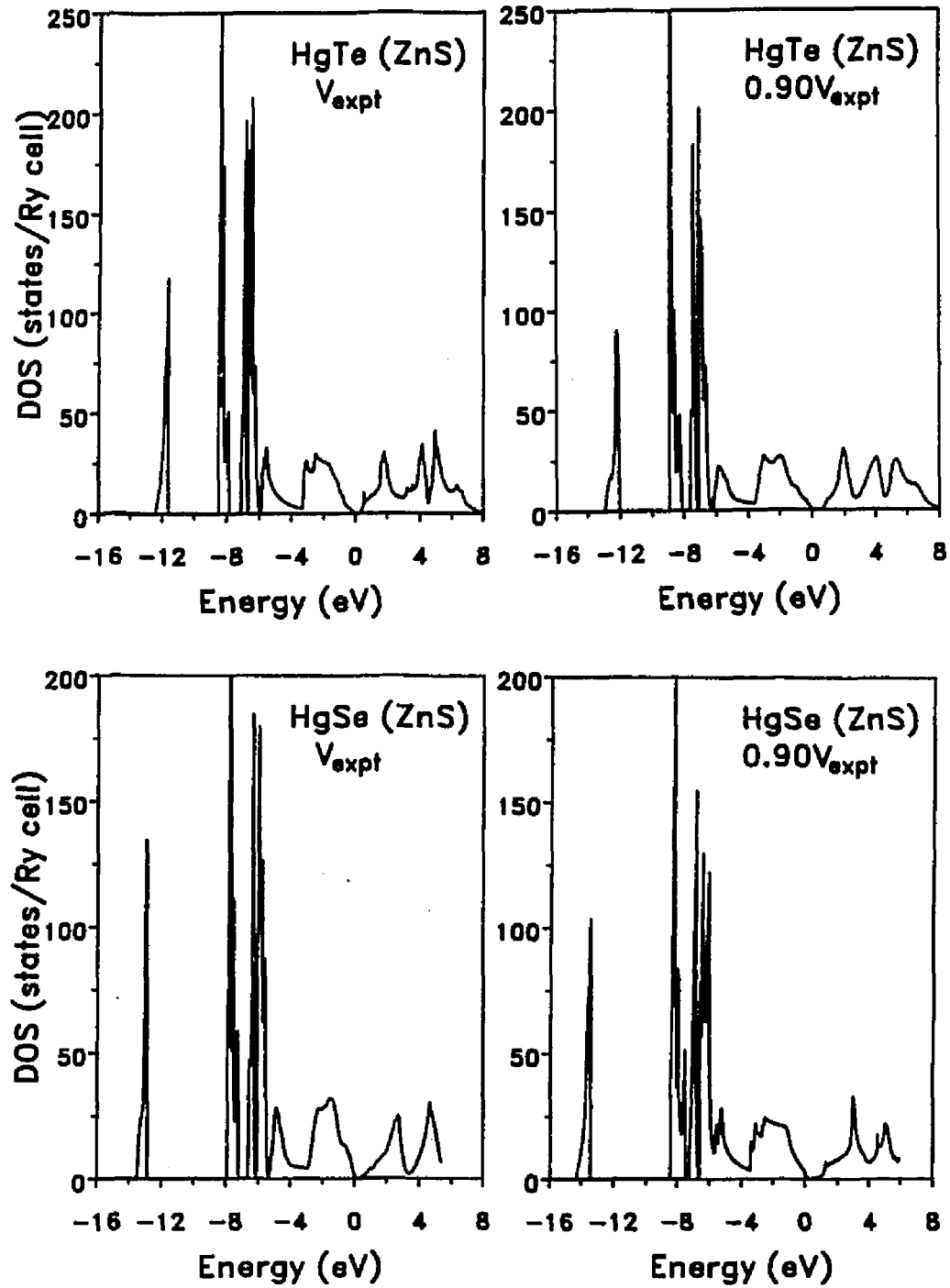


Figure 6.4 Fully relativistic density of states of ZnS structured HgTe and HgSe.

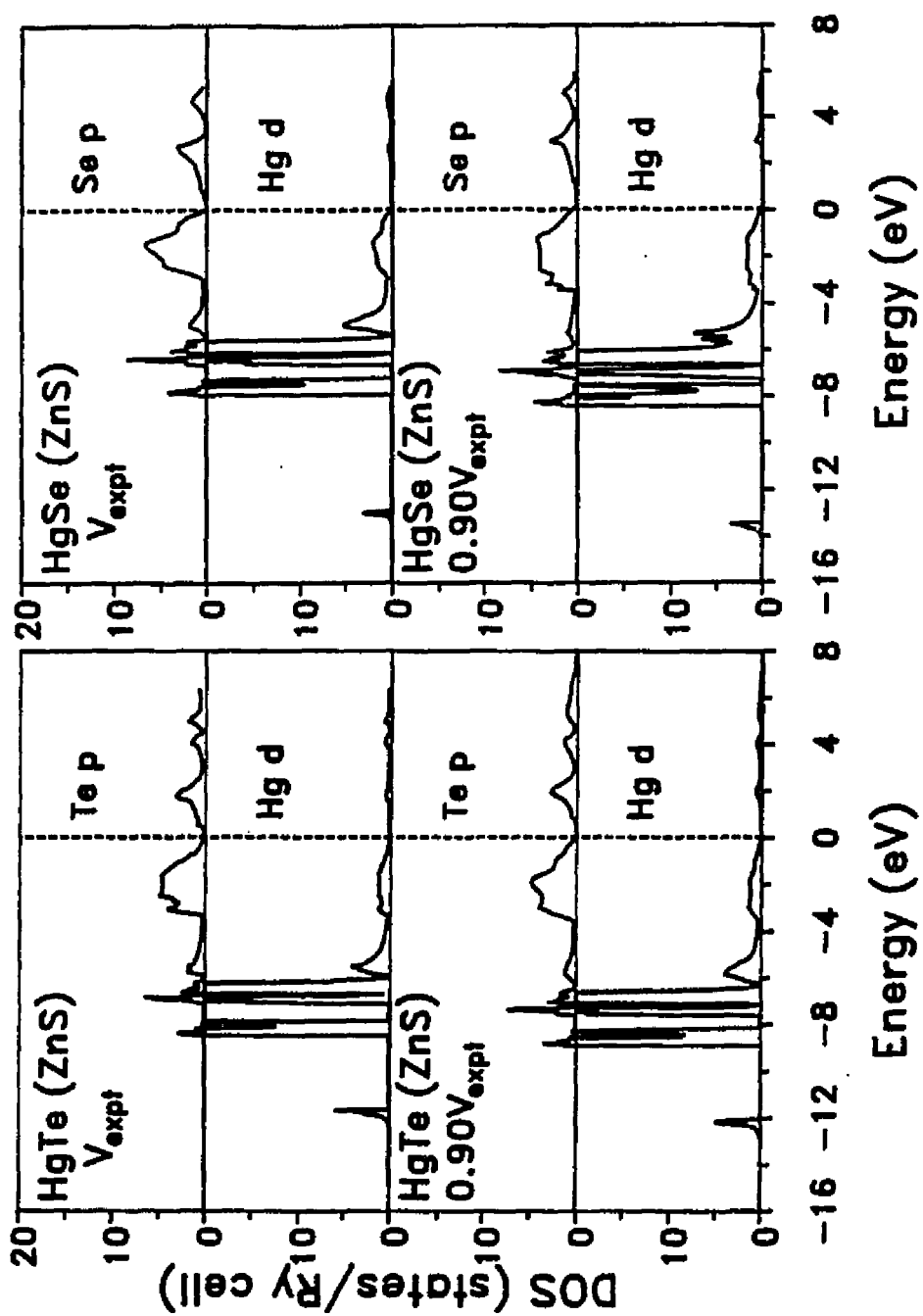


Figure 6.5 Fully relativistic partial density of states of HgTe and HgSe at different volumes for the ZnS structure.



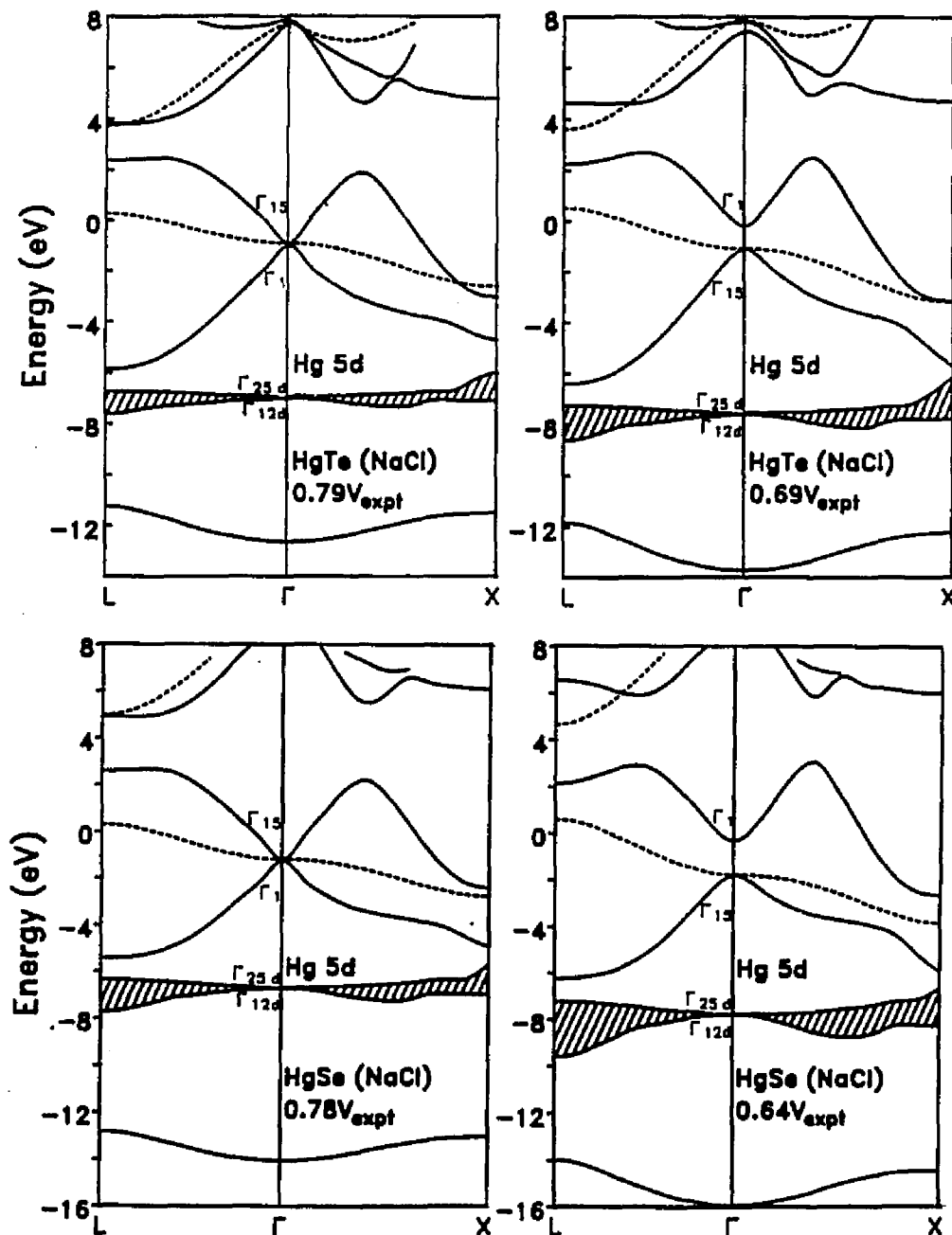


Figure 6.6 Scalar relativistic band structures of NaCl structure HgTe and HgSe. The dashed lines denote doubly degenerate states. The d band width at X and L increases at higher pressure.

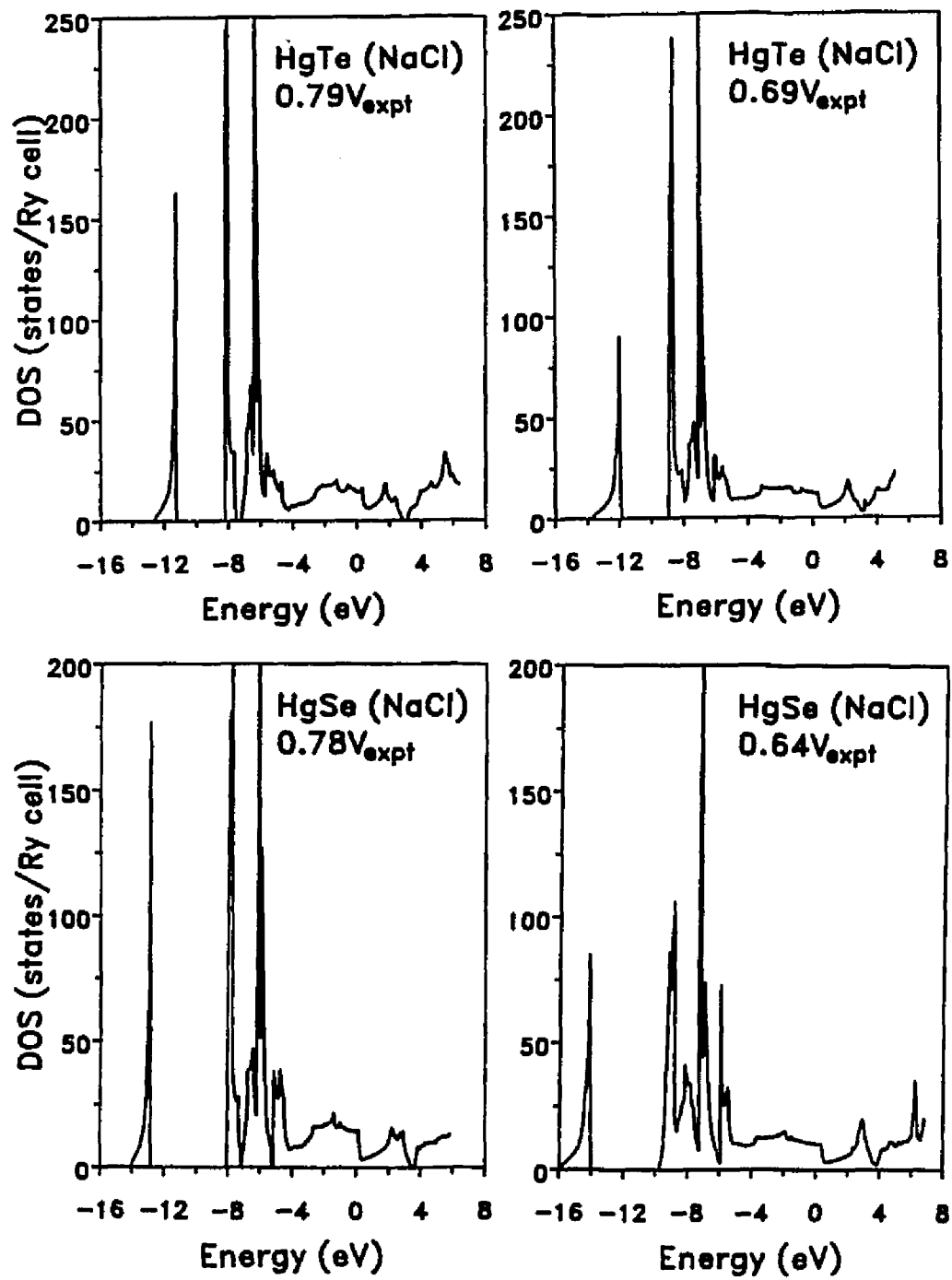


Figure 6.7 Densities of states of NaCl structured HgTe and HgSe calculated fully relativistically.

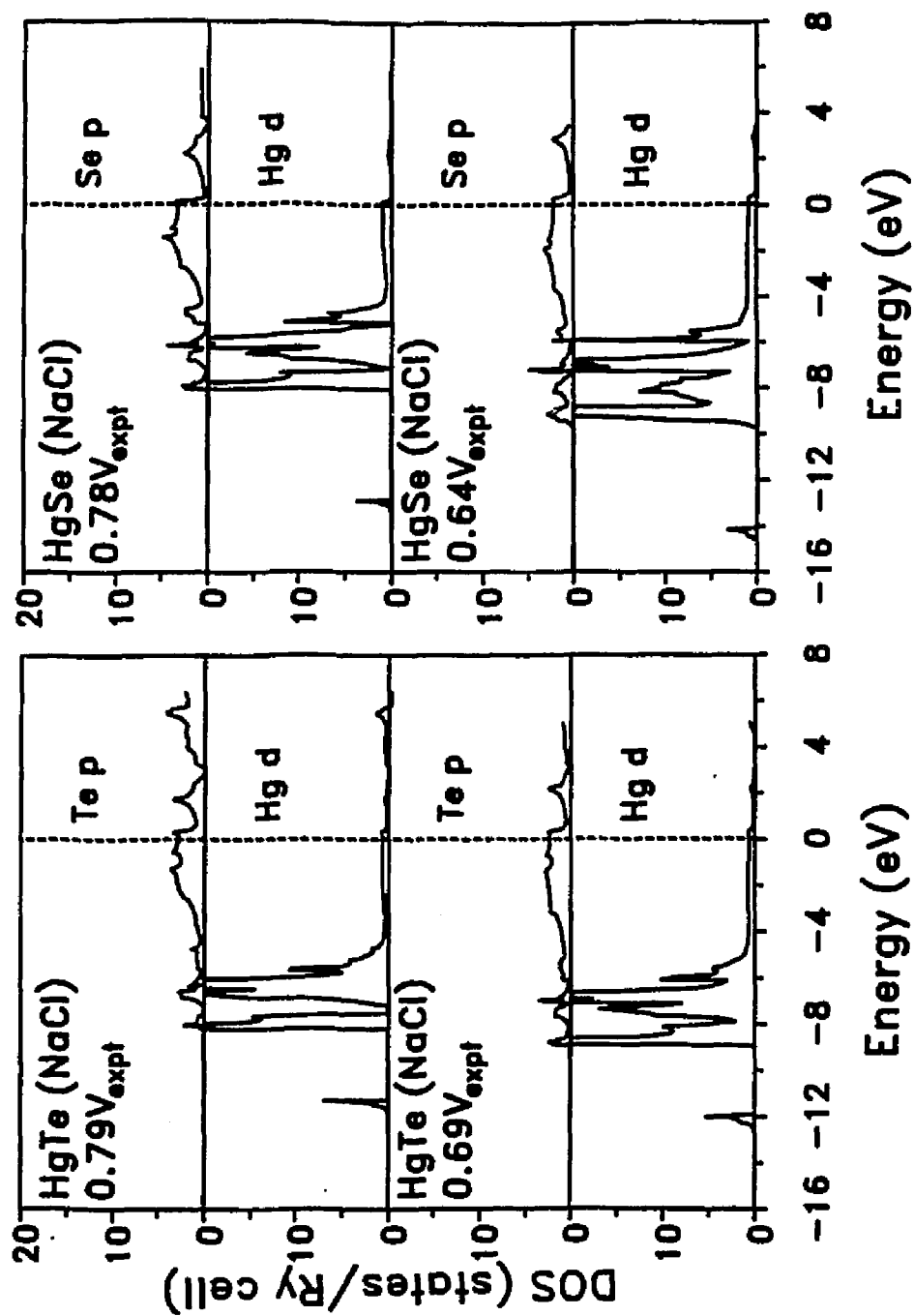


Figure 6.8 Fully relativistic partial density of states of HgTe and HgSe at different volumes for the NaCl structure.

the only effect of pressure on them being to broaden the corresponding peak in the DOS.

The calculated band gaps, d-band energies and spin-orbit splittings for the equilibrium zinc blende phase at  $\Gamma$  and L are compared with the observed values (She73, Ley74, Car63, Sco64, Gul73, Mor73, Ami81) and with previous calculations (Cad85, Wei88) in Table 6.4. For HgTe our results are in good agreement with the LAPW calculation of Wei and Zunger (Wei88), though, as may be expected in LDA based calculations, there are significant discrepancies between the calculated and experiment gaps for both HgSe and HgTe.

Table 6.4

Calculated band gaps  $E_g$  (eV) both scalar-relativistically (SR) and fully relativistically (R), center of d-band  $\epsilon_d$ , spin-orbit splittings of valence bands at  $\Gamma(\Delta_0)$  and L( $\Delta_1$ ), and Hg d bands  $\Delta_d$ , for HgTe and HgSe.

	LMTO <sup>a</sup>	LAPW <sup>b</sup>	HgTe		HgSe	
			LAPW <sup>c</sup>	Expt.	LAPW <sup>c</sup>	Expt.
$E_g$ (SR)		-0.99	-0.93		-1.17	
$E_g$ (R)	-1.06	-1.27	-1.21	-0.30 <sup>d</sup>	-1.28	-0.20 <sup>e</sup>
$\epsilon_d$	-7.38	-7.18	-7.44	-8.44 <sup>f</sup>	-6.96	-8.05 <sup>f</sup>
$\Delta_0$	0.90	0.78	0.77	1.08 <sup>g</sup>	0.25	0.45 <sup>e</sup>
$\Delta_1$	1.31	0.53	0.53	0.62 <sup>h</sup>	0.18	0.30 <sup>e</sup>
$-\Delta_d$	1.7	1.68	1.85	1.85 <sup>f</sup>	1.89	1.80 <sup>f</sup>

<sup>a</sup>Ref. Cad85.

<sup>b</sup>Ref. Wei88.

<sup>c</sup>Present results.

<sup>d</sup>Ref. Gul73.

<sup>e</sup>Ref. Sco64.

<sup>f</sup>Ref. She73.

<sup>g</sup>Ref. Mor73 and Ami81.

<sup>h</sup>Ref. Car63.

The valence charge densities of HgTe and HgSe in the zinc blende structure are shown in Fig. 6.11. The Hg-d electrons in both materials have very similar spatial ranges and similar nearly spherical shapes consistent with their relative inertness. The less prominent bond charge feature in HgSe's charge density is indicative of somewhat weaker covalent bonding in this material consistent with the lower transition pressure for the zinc blende to cinnabar transition as compared to HgTe. In both materials the bond charge features are smeared out under pressure, as may be noted from the valence charge densities at  $0.90 V_{\text{expt}}$  shown in Fig 6.11. Normally, the zinc blende structure in semiconductors is stabilized by a semiconducting gap(Fro83) produced by the arrangement of the electrons into bonding orbitals. In negative gapped HgSe and HgTe the antibonding orbitals are partially occupied, explaining both the relatively weak bond charge features in the charge densities and the low transition pressures. The valence charge density of NaCl structure HgTe is shown in Fig. 6.12 at  $0.79 V_{\text{expt}}$  as well as at  $0.69 V_{\text{expt}}$ . The valence charge densities of HgSe are qualitatively similar. It may be noted that the spatial extent and shape of the Hg-d electrons does not change significantly with pressure, and in fact is quite similar to that found for the zinc blende structure. This is consistent with the inertness of these states indicated by the band structures and thus supports the view that the Hg-d electrons are fairly inactive.

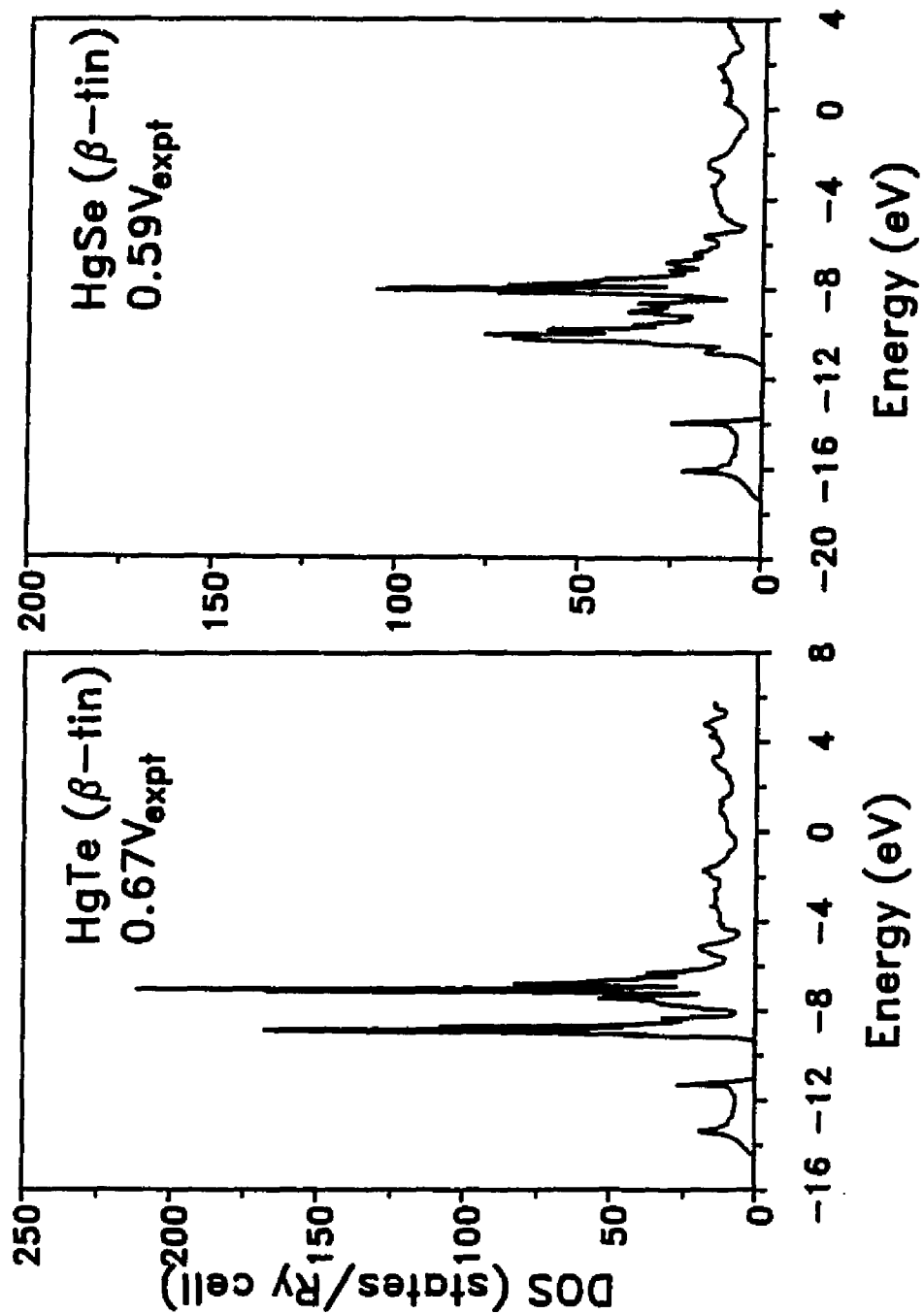


Figure 6.9 Fully relativistic density of states for HgTe and HgSe in the  $\beta$ -Sn structure.

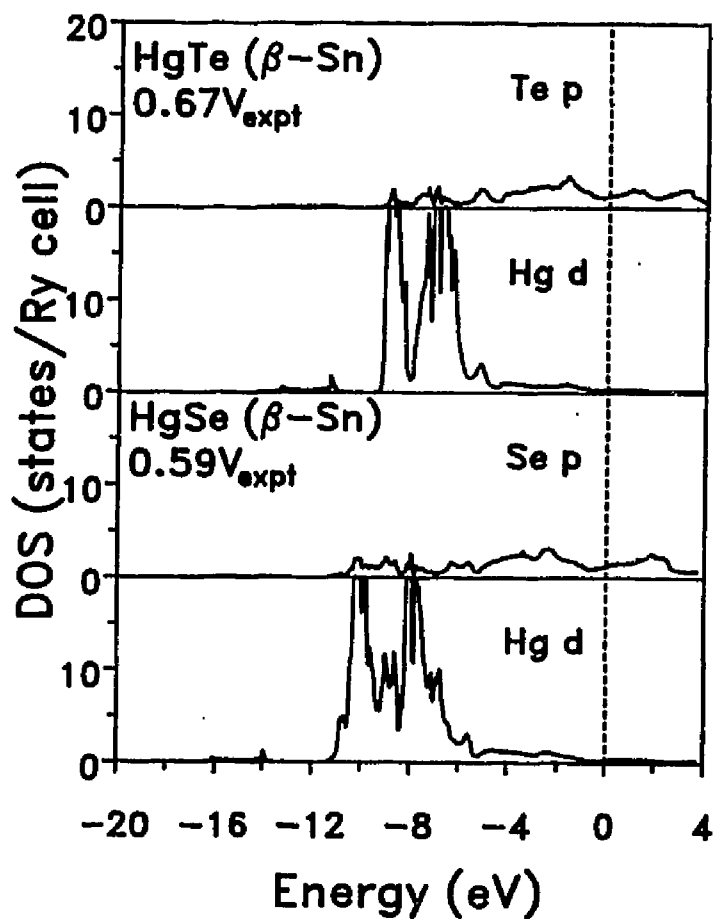


Figure 6.10 Fully relativistic partial density of states of HgTe and HgSe in the  $\beta$ -Sn structure.

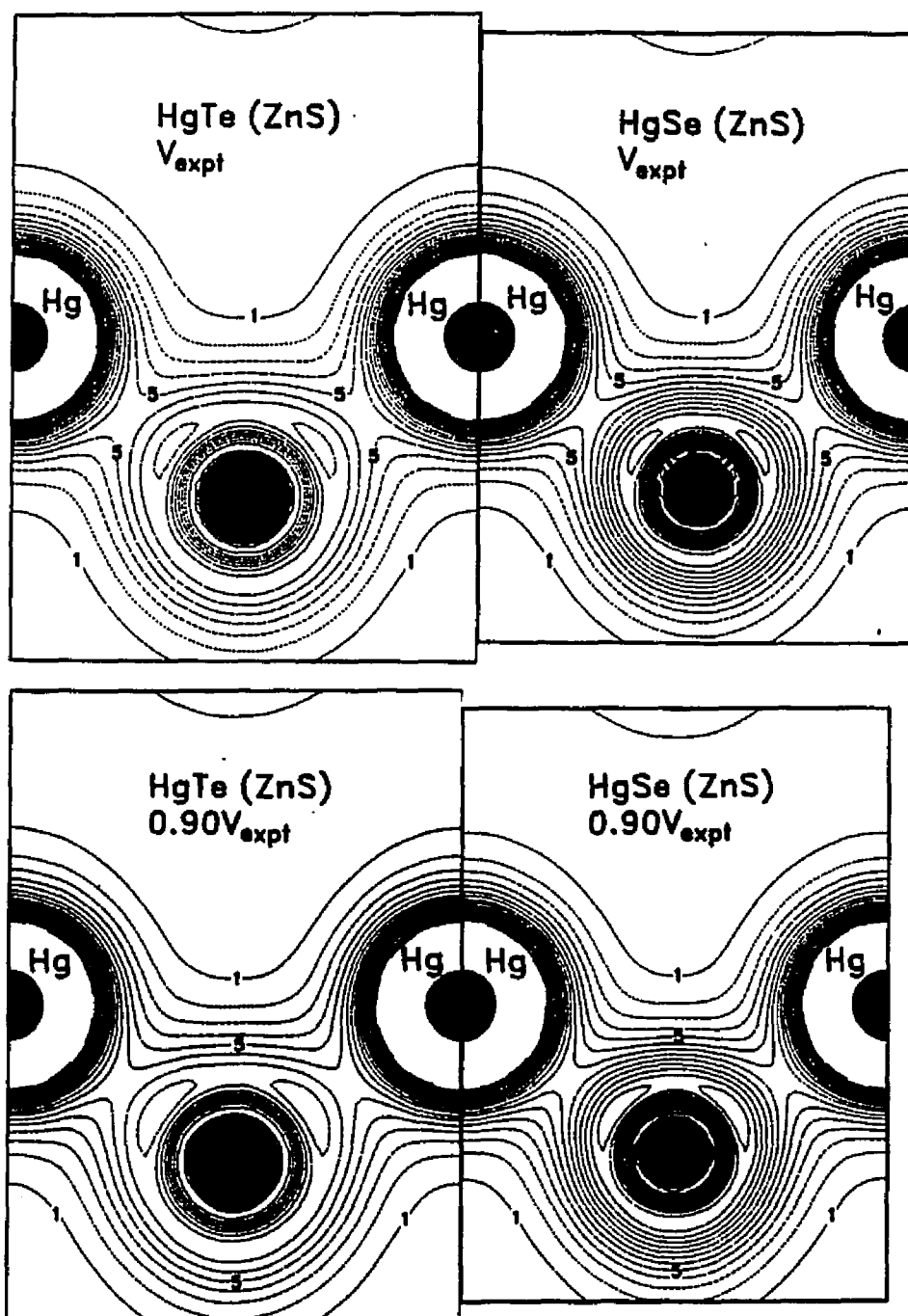


Figure 6.11 Valence charge densities of HgTe and HgSe in a (110) plane at experimental equilibrium volume  $V_{\text{expt}}$  and  $0.90 V_{\text{expt}}$ . The charge density is given in units of  $10^{-2} e/\text{a.u.}$ ; adjacent contours are separated by 1 unit.



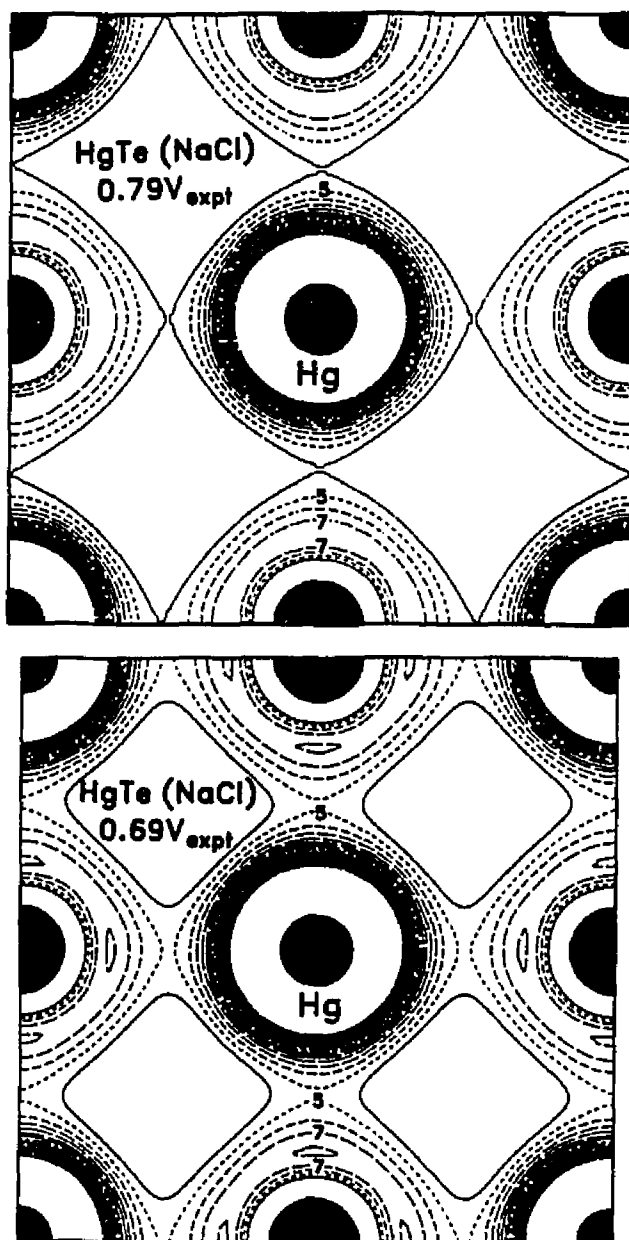


Figure 6.12 The valence charge densities of NaCl structure HgTe of a (100) plane. The units are in  $10^{-2} e/a.u.^3$  adjacent contours are separated by 1 unit.

## 6.5 SUMMARY

We have calculated the phase stabilities of HgTe and HgSe using an LDA based total energy approach. The calculated ground state properties for both materials are in good agreement with experiment as are the orderings of the phases under pressure, but the calculated transition pressures from the ZnS structure phase to the NaCl phase are much lower than the experimental transition pressures from the cinnabar structure phase to the NaCl phase for both HgTe and HgSe. In contrast, the calculated transition pressures from the NaCl phase to the  $\beta$ -Sn phase are in good agreement with experiment.

Significant Hg-d - chalcogen-p hybridization is evident all the way up to the Fermi energy and plays an important role in determining the crystal structure. However, we find that this p-d hybridization appears to be relatively unchanged through the various phase transitions, and that the d-bands themselves are relatively inert.

## Chapter VII

### Pd(111) Surface Relaxation

#### 7.1 INTRODUCTION

The palladium surfaces, as well as the surfaces of other column VIII transition-metals (Ni,Pt,...) have attracted a great deal of experimental and theoretical investigation in recent years. This is due to the fact that Pd is an active catalyst and has a large atomic hydrogen solubility. Experimentally, Pd(111) is found to be rich in surface electronic structure, and many surface states (resonances) exist (Ebe83). There are also many studies of hydrogen (Ebe81, Ebe83) and CO (Oht87) adsorption on Pd (111) surface, which seem to favor the three fold hollow site. A recent low energy electron diffraction (LEED) experiment (Oht87) indicates that the Pd(111) is close to the ideal structure, with possibly small hydrogen-induced deviations for the interlayer spacings (~2%). Louie has examined the electronic states and adsorbate-induced photoemission structure of the Pd(111) surface (Lou78) and the interaction of hydrogen with a Pd(111) surface (Lou79a) using a self-consistent mixed-basis pseudopotential method. Bisi and Calandra (Bis79) have calculated the electronic

structure of Pd(111) using parameterized linear combination of atomic orbitals (LCAO) approach. Larsson and Nilsson (Lar81) have reported the calculation of the inverse photoemission spectra and Hora and Scheffler (Hor84) have presented the calculation of the angle-resolved photoemission spectra for Pd(111). Koukal *et al.* (Kou89) has interpreted the unoccupied surface states observed by very-low-energy electron diffraction (VLEED) and inverse photoemission (IPES). However, all the above calculations were nonrelativistic.

Here, we report the electronic structure of Pd(111) using a general potential relativistic linearized augmented plane wave (LAPW) method. The total energy of the system is evaluated as a function of the top layer spacing, which enables us to study the surface relaxation effects.

## 7.2 Details of Calculations

The fcc (111) surface may be obtained by slicing an infinite crystal perpendicular to the [111] crystal axis. This produces layers parallel to the surface in which the atoms are arranged with hexagonal symmetry. There are three types of layers and repeat in an ABCABC... fashion along the [111] direction. For a thin film, there is an inversion center which lies at the atom in the central layer for the odd number of layers, and lies at a point midway between the two central layers and directly below an atom of the third

type of layer. The (111) crystal structure is illustrated in Fig. 7.1, along with the two dimensional reciprocal lattice. The space group for a (111) film is just the triangle group  $C_{3v}(3m)$  times the inversion. The character tables for the high symmetry points  $\bar{\Gamma}$ ,  $\bar{K}$ , and  $\bar{M}$  are listed by Caruthers et al. (Car74).

The calculations were iterated to self-consistency, which was considered achieved when the total energies were stable to about  $10^{-5}$  Ry. The radius of the Pd muffin-tin sphere was 2.15 a.u. A basis set cutoff of  $R_{mt}K_{max} = 8.0$  was used and a basis set cutoff of  $R_{mt}K_{max}=8.8$  was also tested for bulk fcc Pd, which gives nearly the same result as the  $R_{mt}K_{max}=8.0$  case. Hence, the  $R_{mt}K_{max}=8.0$  was used in the surface calculations. The spin-orbit interaction was found to have a negligible effect upon the structural and cohesive properties for bulk fcc Pd. Therefore, the surface calculation was done only scalar relativistically. The Brillouin zone summations for bulk fcc Pd were performed using 60 special k-points in the irreducible wedge of the Brillouin zone, and 10 special k-points in the irreducible wedge of the two-dimensional Brillouin zone for Pd(111) surface. In the Pd(111) calculation, a seven-layer slab of Pd is placed in a periodic superlattice with the slabs separated by a distance equivalent to four atomic layers of Pd. The densities of states were calculated using the tetrahedral

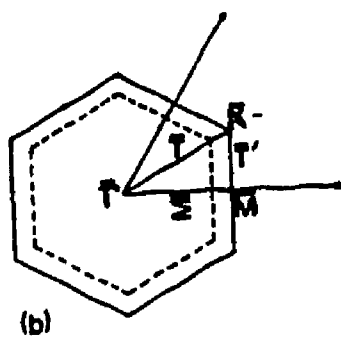
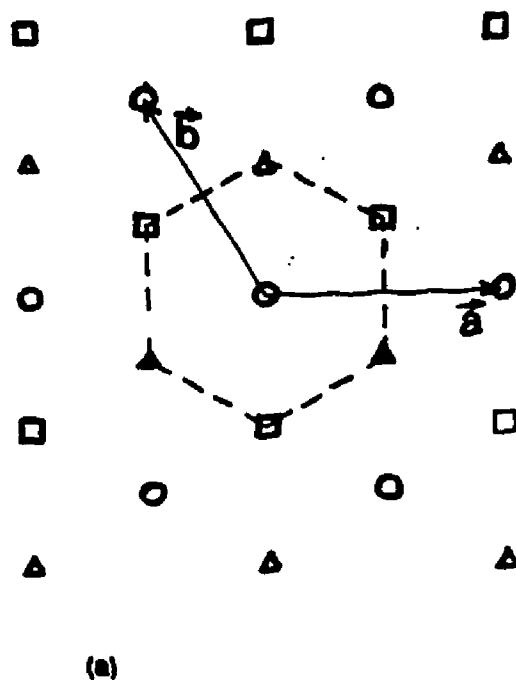


Figure 7.1 (a) Crystal structure of the (111) face of face-centered-cubic Pd. Circles denote the atoms in A layers; squares denote atoms in B layers; triangles denote atoms in C layers. The length of  $\vec{a}$  and  $\vec{b}$  are  $a/2^{\frac{1}{2}}$ , where  $a$  is cubic edge length. The distance between successive layers is  $a/3^{\frac{1}{2}}$ . (b) The two-dimensional reciprocal lattice for fcc (111) face.

method, using 195 uniformly distributed ab initio k-points for the bulk Pd and 30 for the Pd(111) surface.

### 7.3 Bulk fcc Pd

We first performed calculations on bulk Pd. There has been many electronic structure calculations on fcc Pd. Our calculated band structure is in good agreement with the previous non self-consistent relativistic APW (RAPW) result of Andersen (And70), non self-consistent relativistic APW (RAPW) calculation of Christensen (Chr76), and LAPW calculation of MacDonald et al. (Mac81). The scalar relativistic band structure is shown in Figure 7.2. Table 7.1 lists the eigenvalues (with spin-orbit interaction) at high symmetry points  $\Gamma$  and L along with the previous calculations and experimental results (Him78). We also tabulate the calculated (fully relativistic) density of states at the Fermi energy in Table 7.2. The density of states (Figure 7.2) is very similar to the previous calculations. The total energy shown in Figure 7.3, yields the equilibrium structural properties by fitting the total energy to the Murnaghan equation of state. The results are in good agreement with experiment as shown in Table 7.3. The lattice constant is underestimated by about 1%, the bulk modulus is overestimated by about 15%, and the cohesive energy is overestimated by 1.3 eV. (which is expected for the LDA based calculation due to the fact that LDA underbinds atoms.) The differences

between our LAPW calculation and that of the non-relativistic KKR calculation (Mor78) is  $\Delta a=0.08\text{\AA}$ ,  $\Delta B_0=0.53$  Mbar, and  $\Delta E_c=1.49$  eV. These relativistic effects were also observed in Au by Wei *et al.* (Wei87). Our calculation indicates that the spin-orbit interaction plays a negligible role in the structural and cohesive properties.

Table 7.1

Energy eigenvalues relative to the Fermi energy at the symmetry points  $\Gamma$  and L, and comparison with the previous calculations and experiment.

Band No.	LAPW <sup>a</sup>	LAPW <sup>b</sup>	RAPW <sup>c</sup>	PP <sup>d</sup>	KKR <sup>e</sup>	expt. <sup>f</sup>
1	-535	-528	-515			
2	-221	-223	-205	-188	-197	-188±11
$\Gamma$ 3	-221	-223	-205	-188	-197	-188±11
4	-198	-200	-183	-188	-197	-188±11
5	-88	-90	-86	-89	-90	-85±7
6	-88	-90	-86	-89	-90	-85±7
1	-396	-395	-370			
2	-228	-229	-219	-196	-204	-176±15
L 3	-203	-204	-193	-196	-204	-176±15
4	-7	-9	-10	-7	-4	-29±15
5	3	5	4	-7	-4	-7±7
6	70	78	70		98	

<sup>a</sup>Present calculation.

<sup>b</sup>Ref. Mac81.

<sup>c</sup>Ref. Chr76, non self-consistent calculation, which is almost identical to the earlier non self-consistent RAPW calculation of Andersen(And70).

<sup>d</sup>Ref. Lou79, Pseudopotential calculation, nonrelativistic.

<sup>e</sup>Ref. Mor78, nonrelativistic.

<sup>f</sup>Ref. Him78.



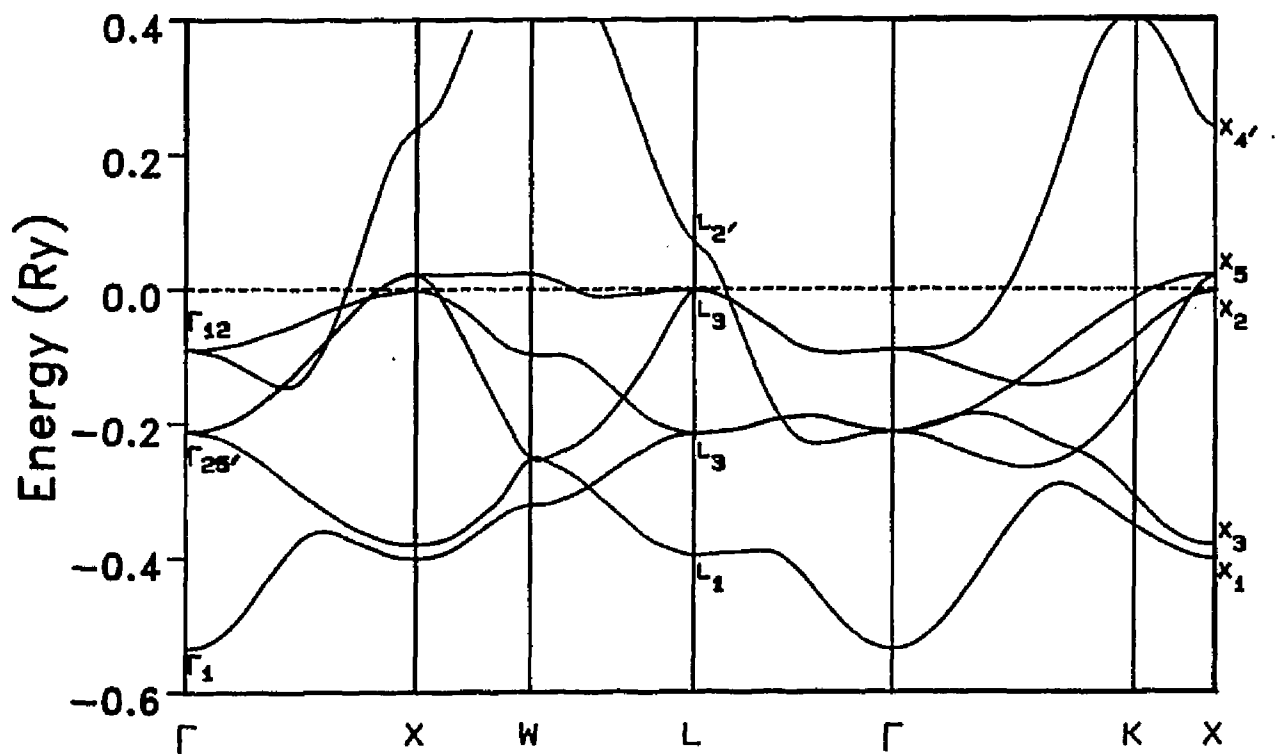


Figure 7.2 Scalar relativistic band structure of Pd at the experimental lattice constant ( $a=3.887 \text{ \AA}$ ).

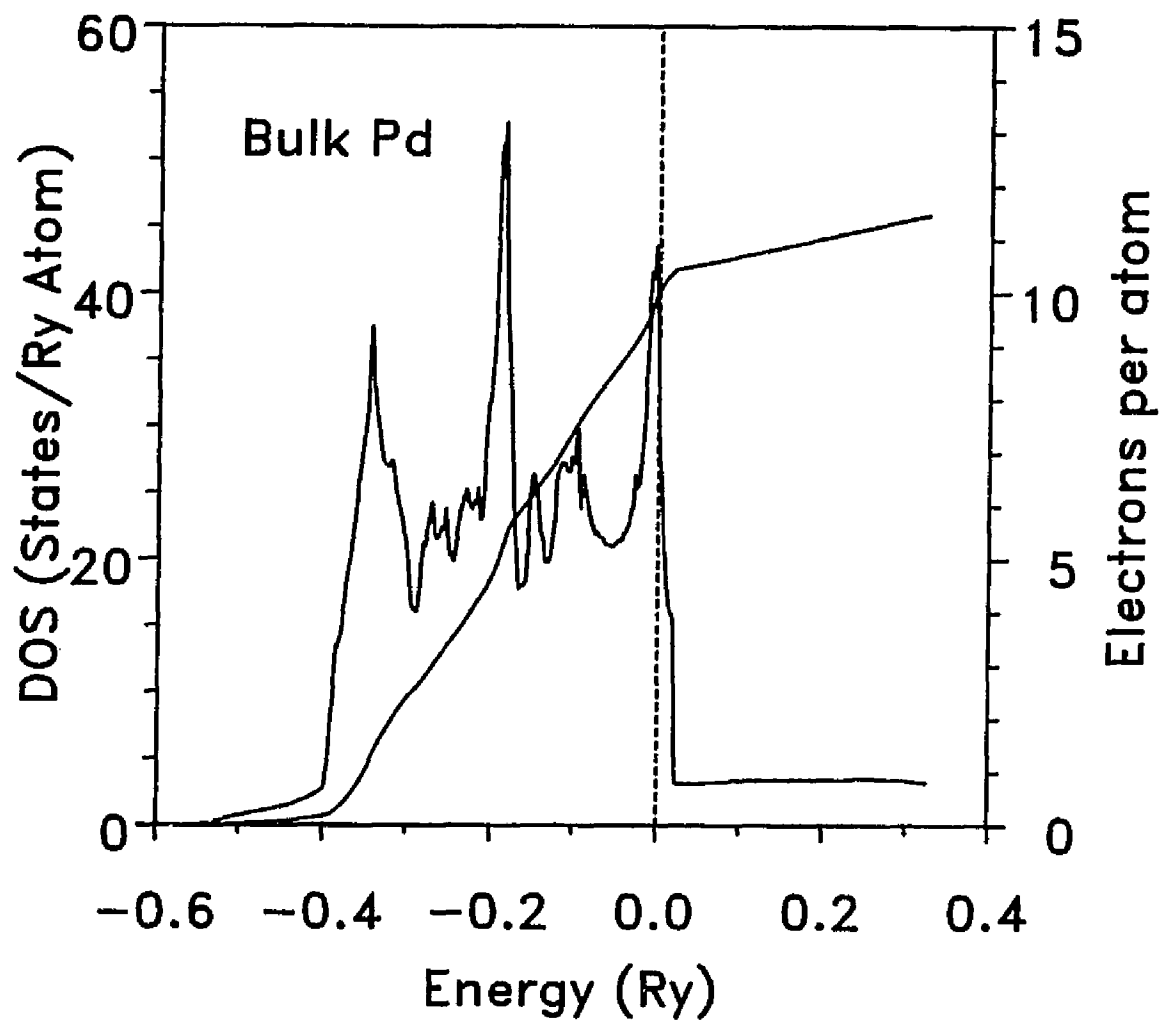


Figure 7.3 Fully relativistic density of states of Pd at the experimental lattice constant, which agrees well with the previous calculations.

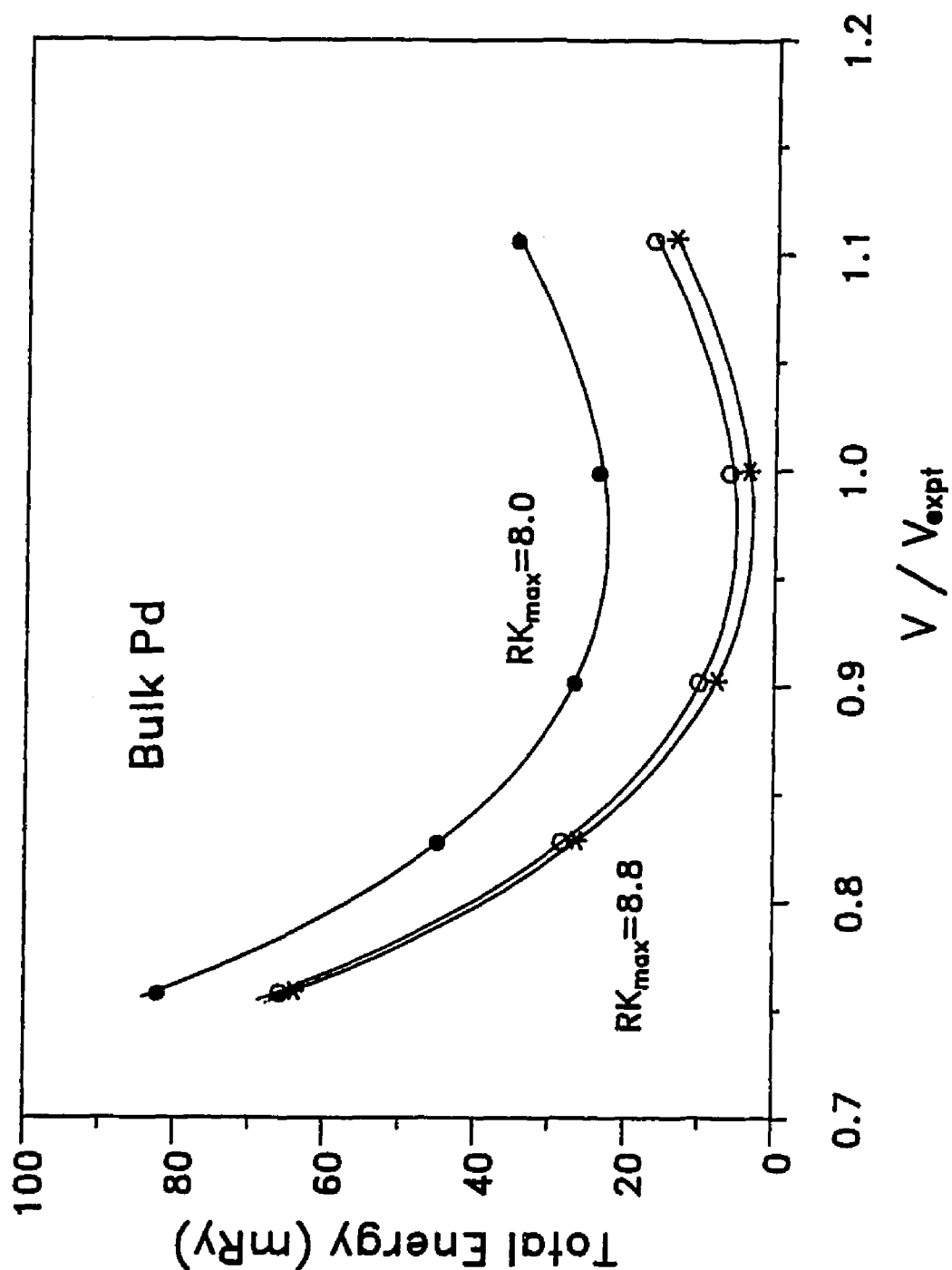


Figure 7.4 Total energy versus volume for bulk Pd. The lower two curves are the scalar and fully relativistic results, which have a larger basis set cutoff  $R_{mt}K_{max} = 8.8$ . Upper curve is the scalar relativistic result and with a smaller basis set cutoff  $R_{mt}K_{max} = 8.0$ , which converges reasonably well compared to that of the larger basis set.

Table 7.2

Density of states at the Fermi energy at the experimental volume.

	LAPW <sup>a</sup>	LAPW <sup>b</sup>	KKR <sup>c</sup>	RAPW <sup>d</sup>	RAPW <sup>e</sup>	APW <sup>f</sup>
$N(E_f)$	36.4	35.0	31.4	32.1	32.7	31.1

<sup>a</sup>Present calculation.

<sup>b</sup>Ref. Mac81.

<sup>c</sup>Ref. Mor78, self-consistent, non-relativistic.

<sup>d</sup>Ref. Chr76, non self-consistent.

<sup>e</sup>Ref. And70, non self-consistent.

<sup>f</sup>Ref. Mue70, non self-consistent.

Table 7.3

Bulk Pd structural properties.

	a (Å)	$B_0$ (Mbar)	$B_0'$	$E_c$ (eV)
$RK_{max}=8.0$ (no S-O)	3.85	2.33	4.83	4.92
$RK_{max}=8.8$ (no S-O)	3.85	2.24	4.89	5.15
$RK_{max}=8.8$ (with S-O)	3.86	2.23	4.80	5.18
Moruzzi et al. <sup>a</sup>	3.93	1.70	.	3.69
Expt.	3.887 <sup>b</sup>	1.94 <sup>c</sup>	.	3.89 <sup>d</sup>

<sup>a</sup>Ref. Mor78.

<sup>b</sup>Ref. Vi185.

<sup>c</sup>Ref. 20 Gee81, at 0 K.

<sup>d</sup>Ref. Kit76.

## 7.4 Pd(111)

### A. Surface relaxation

LEED experiments suggest that the top interlayer spac-

ing tends to contract in metals, especially on open surfaces like fcc (110) and bcc (100) (Hov79). For example, there is about 10-15% contraction for fcc Al (110) (Hov79) and 8% contraction for bcc W(100) (Mar80). The contraction or expansion of the top interlayer spacing is smaller for more close-packed faces. Fig. 7.5 depicts the total valence charge density for a  $(\bar{1}10)$  plane cutting the (111) surface along with the bulk valence charge density on a (100) plane. The charge density contour plot for Pd(111) in Fig. 7.5 shows that the effect of the surface on the charge density is localized and heals quickly. The charge density in the second layer already resembles the bulk charge density.

The total energy is evaluated as a function of the top interlayer spacing, keeping all the other parameters constant. As seen in Fig. 7.6. The top layer spacing contracts about 1% compared to the experimental bulk lattice spacing. However, in our calculation of the bulk Pd, the calculated lattice constant is about 1% smaller than that of the experimental value. We can conclude that Pd(111) is within 1% of the ideal (111) surface. Ohtani *et al.* (Oht87) have studied the multilayer surface relaxation of Pd(111) using the LEED technique and have found that the deviation of the interlayer spacings from the ideal structure were  $\Delta d_{12}$  (+1.3%),  $\Delta d_{23}$  (-1.3%),  $\Delta d_{34}$  (+2.2%), and  $\Delta d_{45}$  (+2.2%) respectively, with an uncertainty of  $\pm 1.3\%$ . They noted that these small relaxations may well be due to the contamination of

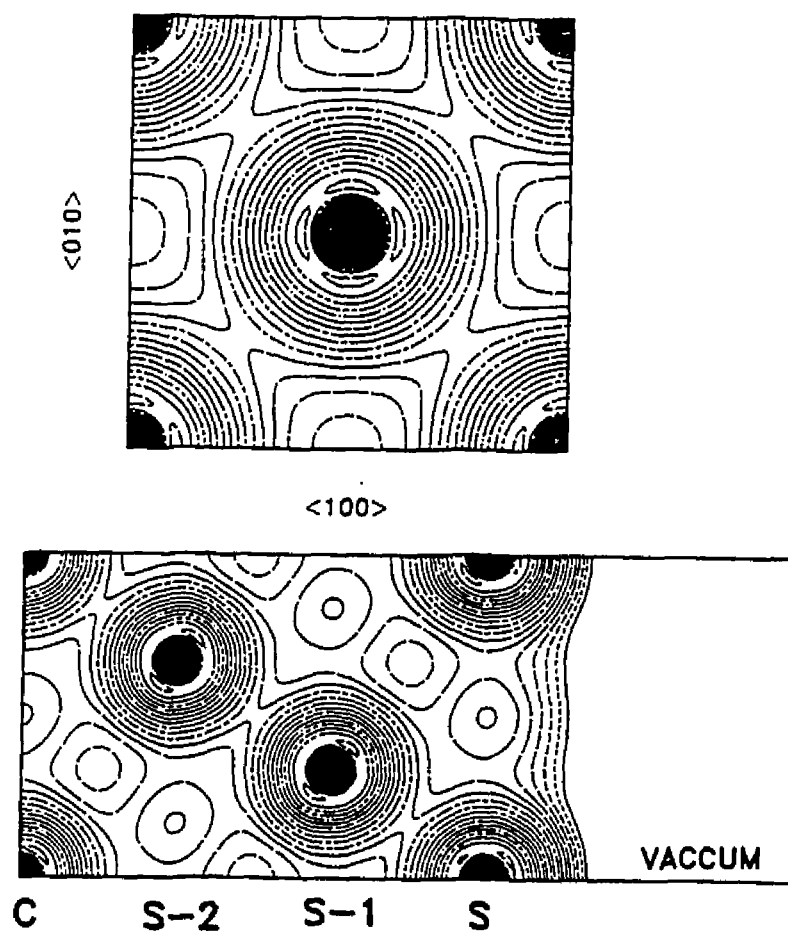


Figure 7.5 The total valence charge density is shown on the  $(\bar{1}10)$  plane cutting the Pd(111) surface. The charge density at the second layer already resembles the bulk density. The adjacent contour is separated by  $\rho(n+1)/\rho(n)=1.272$ , and in units of  $10^{-2}$  e/a.u.<sup>3</sup>.

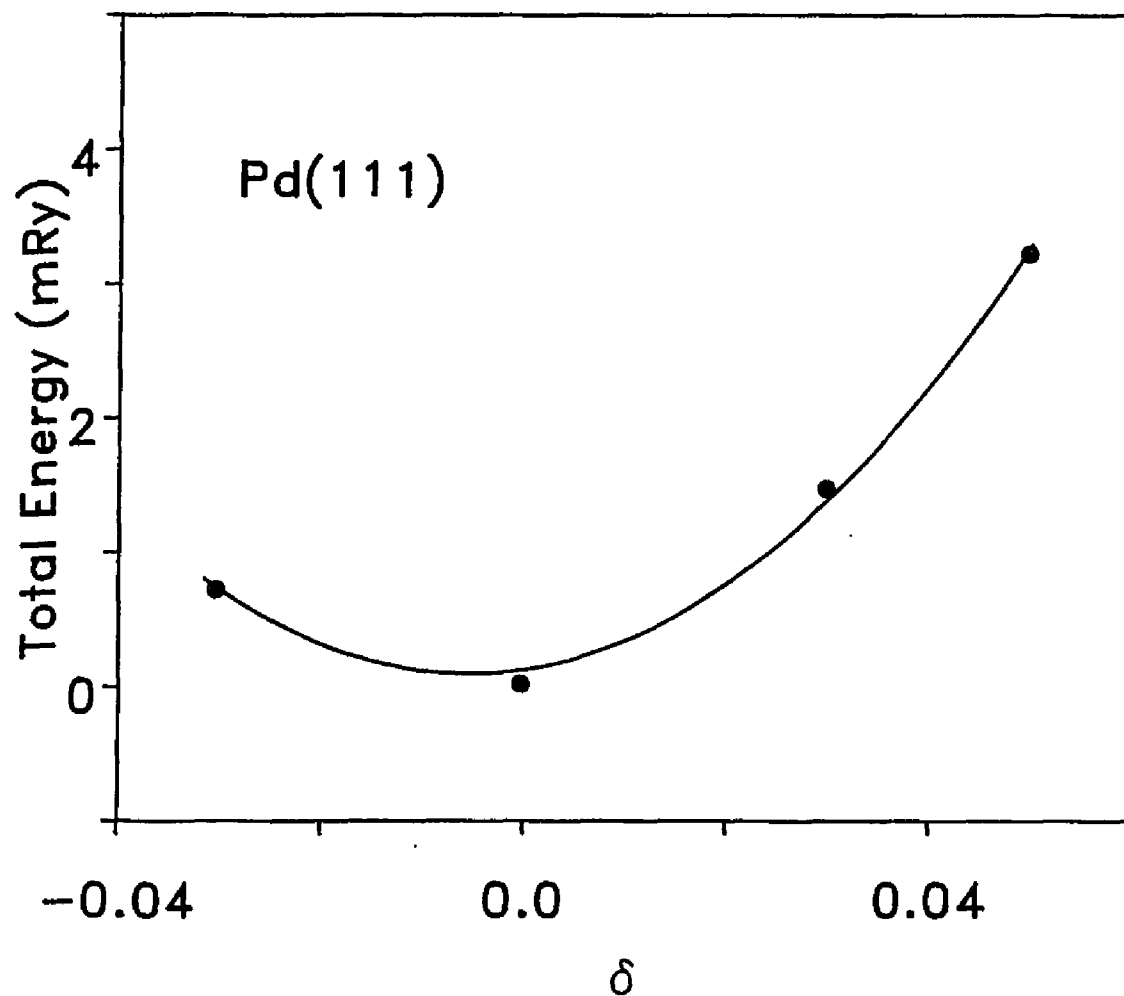


Figure 7.6 Total energy vs the top layer spacing (relative to the ideal experimental bulk spacing). The total energy minimum falls at -1%.

hydrogen on this surface. Our results show that clean Pd(111) is close to ideal, consistent with the experimental measurements.

### B. Electronic structure

Scalar relativistic electronic structure calculations were carried out for an unrelaxed Pd(111) surface. The calculated work function (see Table 7.4), which is an indication of the convergence to self-consistency, is 5.7 eV and is in excellent agreement with experiment (Dem77) (5.6 eV) and the previous self-consistent non-relativistic pseudopotential (PP) calculation (5.8 eV) of Louie (Lou78).

Table 7.4

Work function for Pd(111).

	Present LAPW	Louie <sup>a</sup> PP	Demuth <sup>b</sup> Expt.
$\phi$ (eV)	5.7	5.8	5.6

<sup>a</sup>Ref. Lou78.

<sup>b</sup>Ref. Dem77.

Table 7.5 lists the surface states and resonances for Pd(111) at high symmetry points  $\bar{\Gamma}$ ,  $\bar{K}$ , and  $\bar{M}$ . There is general agreement between the present calculation and the previous non-relativistic calculations of Louie (Lou78) and the non-self-consistent nonrelativistic LCAO calculation of



Bisi and Calandra (Bis79). In the present calculations, however, the calculated surface states and resonances consistently lie below those of Louie. The relativistic shifts are small for the states near the Fermi energy, which are primarily of d-character. The differences get larger for the lower-lying states, which have more s character. The largest difference is 1 eV at the  $\bar{\Gamma}$  point (-5.1 eV for the LAPW and -4.1 eV for the PP, respectively). These are consistent with the relativistic shifts seen in bulk Pd. The eigenvalue differences for bulk Pd at the  $\Gamma$  and L between the present calculation and the nonrelativistic calculation of Louie *et al.* (Lou79b) exhibit the same behavior, a comparison of bulk results is shown in table 7.1.

Table 7.5

Surface states and surface resonances for Pd(111) relative to the Fermi Energy (in eV).

	Present	PP <sup>a</sup>	LCAO <sup>b</sup>	Expt. <sup>c</sup>	type of state
$\bar{\Gamma}$	1.1	1.9	.	1.3 <sup>d</sup>	s, p
	-0.2	-0.2	-0.70	-0.3	d(z <sub>y</sub> ), d(z <sub>x</sub> )
	-2.4	-1.9	-2.28	-2.2	d(x <sup>2</sup> -y <sup>2</sup> ), d(xy)
	-5.1	-4.1	-4.06	.	d(3z <sup>2</sup> -r <sup>2</sup> ), s
$\bar{K}$	-1.3	-1.0	-0.49	-0.3	d(z <sub>x</sub> ), d(z <sub>y</sub> )
	-2.3	-1.9	-1.44	-2.1	d(x <sup>2</sup> -y <sup>2</sup> ), d(xy)
	-3.4	-3.0	-3.8	.	backbone
$\bar{M}$	0.3	0.4	0.18	.	d(x <sup>2</sup> -y <sup>2</sup> ), d(xy)
	-4.5	-3.8	-4.16	.	d(x <sup>2</sup> -y <sup>2</sup> ), d(xy), s

<sup>a</sup>Ref. Lou78.<sup>c</sup>Ref. Ebe83.<sup>b</sup>Ref. Bis79.<sup>d</sup>Ref. Hul86.

The unoccupied states in Pd(111) have attracted experimental (Joh82,Wes84,Hul86) and theoretical investigations (Lar81,Kou89) due to the developments of the IPES, two-photon photoemission (2PPE) and VLEED techniques. At present, IPES, 2PPE (Kou89) can probe the empty states between the Fermi energy and the vacuum level in the vicinity of the  $\bar{\Gamma}$  point. While the VLEED (Kou89) only indirectly accesses the empty states. The unoccupied surface state at the  $\bar{\Gamma}$  was first predicted by Louie (Lou78), and was later confirmed by an IPES experiment (Joh82). This surface state lies 1.9 eV above the Fermi energy, and falls near the bottom of the bulk  $L_2$ - $L_1$  band gap and is s,p-like with a long decay length. Experimentally(Joh82), this states was found 1.7 eV above the Fermi energy. Subsequent study (Wes84) withdrew the earlier assignment of this surface state, and more recently, high-resolution IPES (Hul86) places this state 1.3 eV above the Fermi energy. This is in very good agreement with value of 1.1 eV above the Fermi energy. The discrepancy between the two different calculations can again be accounted for by relativistic effects. (The eigenvalues differences at the  $L_2$ , for the two bulk calculations is about 0.7 eV.) Koukal et al. (Kou89) have recently interpreted the data obtained by the IPES (Hul86) and VLEED (Con86) techniques, and they conclude that the surface features observed by the two techniques are two distinct states, i.e., the surface states at  $\bar{\Gamma}$  1.3 eV above

the  $E_f$  seen by IPES, and the surface feature along  $\bar{\Gamma}-\bar{M}$  9 - 12 eV above the  $E_f$  seen by VLEED.

The local (muffin-tin-projected) density of states (LDOS) is shown in Fig. 7.7. The LDOS in the center layer is very close to that of the bulk Pd (see Fig. 7.3), while the LDOS in the surface layer is enhanced in the region near the Fermi energy because of the existence of surface states. The LDOS difference between the surface layer and that of the center clearly shows that the enhancement of LDOS near the Fermi energy is compensated by a decrease at the bottom of the d bands. The calculated LDOS are similar to the previous calculations (Lou78, Bis79).

Figs. 7.8-7.10 depict the charge density contour plots for various surface states (resonances) at the high symmetry points  $\bar{\Gamma}, \bar{K}$ , and  $\bar{M}$ . Most of the surface states (resonances) are primarily of various d-angular-momentum components (see table V) and localized in the top two layers. The unoccupied surface state at  $\bar{\Gamma}$  (at 1.1 eV, Fig. 7.8 (d) ) is mostly of a p-character mixed with some s- and d-character, which protrudes deeply into both the vacuum and the interior. On the other hand, the unoccupied surface state at  $\bar{M}$  (0.3 eV, Fig. 7.10 (b) ) is purely d-like ( $d_{x^2-y^2}, d_{xy}$ , the z axis is taken orthogonal to the surface) and is almost completely localized in the surface layer. Those states, which have a sizeable relativistic shift, tend to be more delocalized in the present calculation; e.g., the twofold

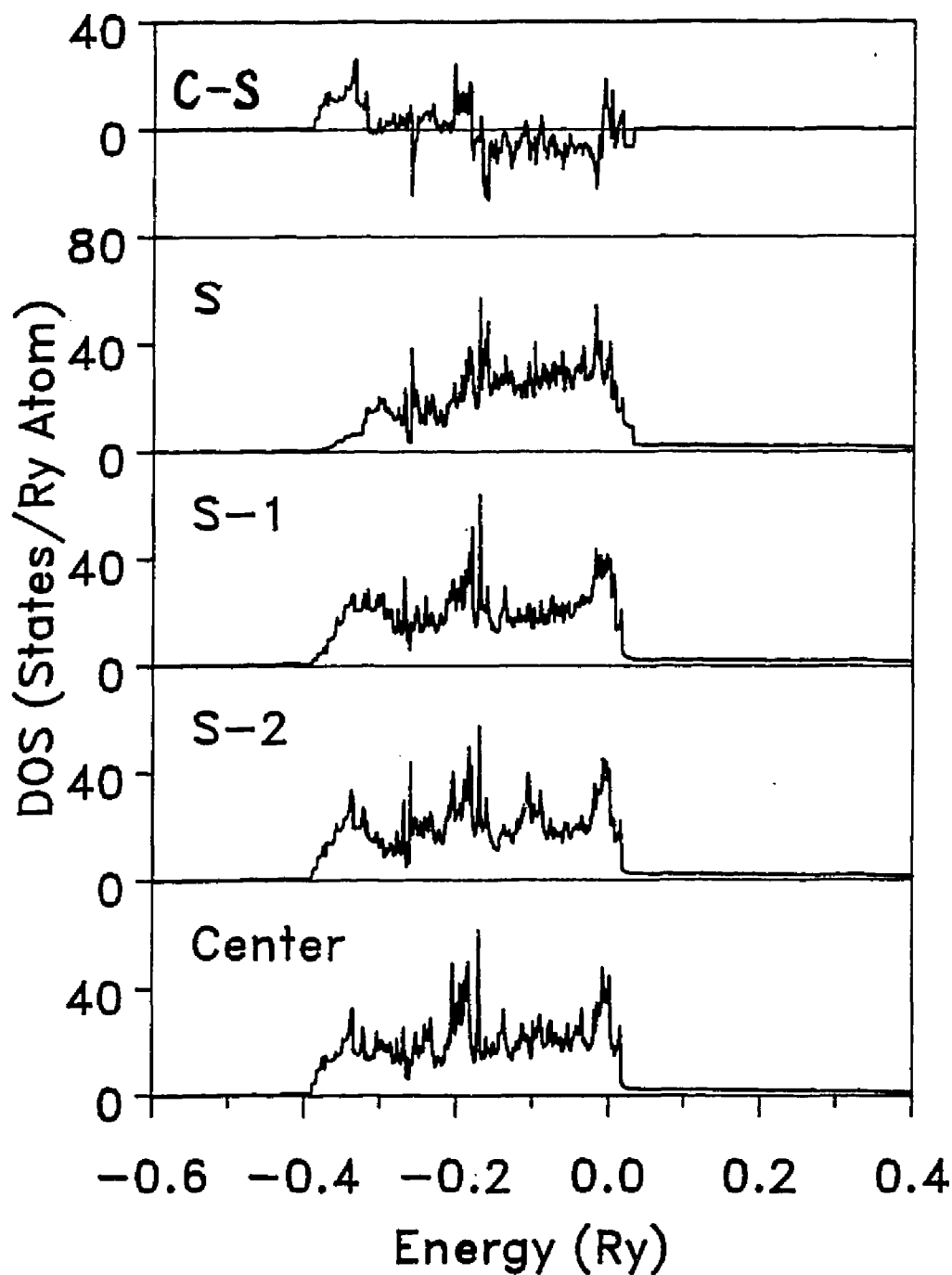


Figure 7.7 Local density of states (LDOS) for Pd(111) at the surface (S), S-1, S-2, and the center layer. The LDOS in the center layer resembles the bulk density of state (Fig. 7.3). The LDOS difference between the center and the surface layer reveals that the LDOS enhancement below the Fermi energy is at the price of the LDOS at the bottom of the d bands.

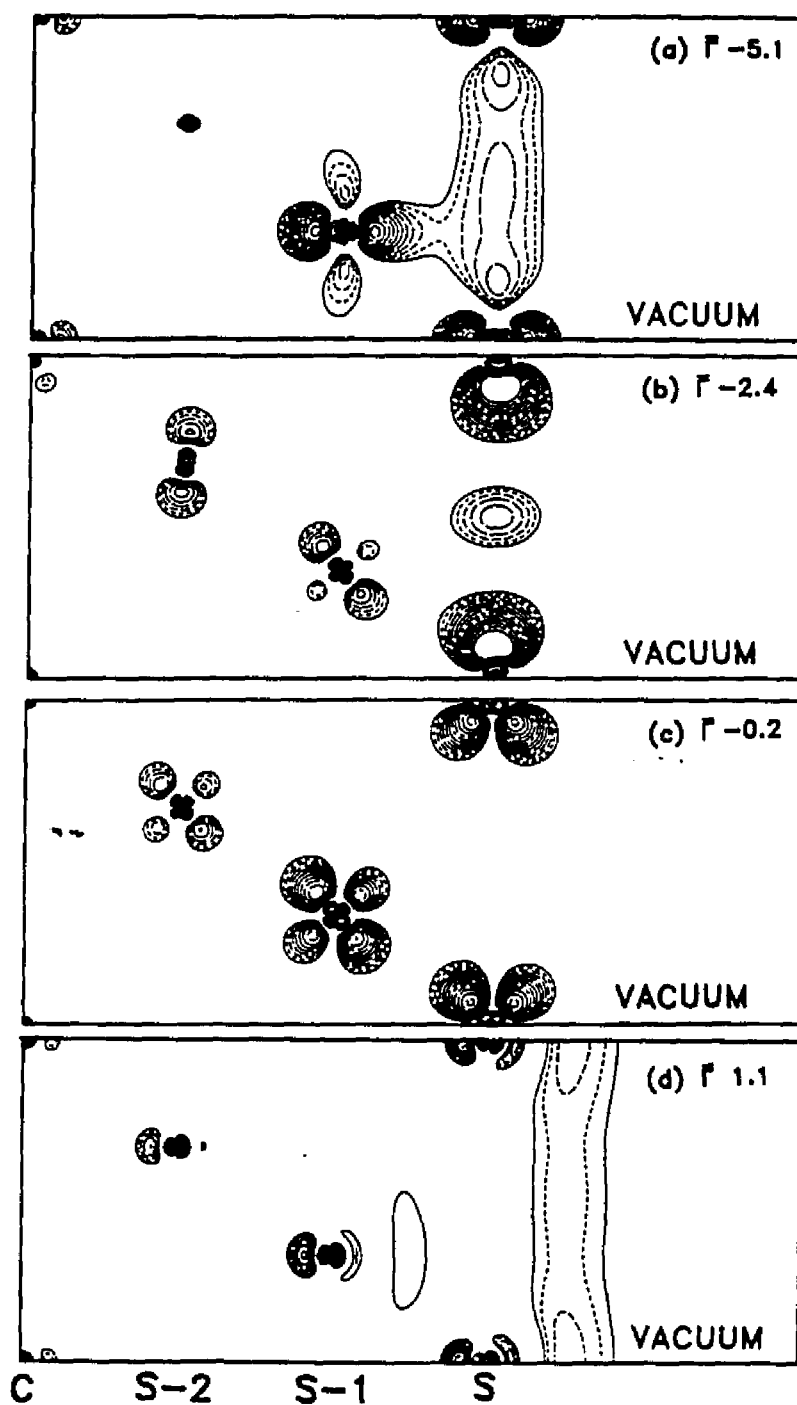


Figure 7.8 Surface states at  $\bar{\Gamma}$  (a) at -5.1 eV, (b) at -2.4 eV (doubly degenerate), (c) at -0.2 eV, and (d) at 1.1 eV. See Fig. 7.5 for units.

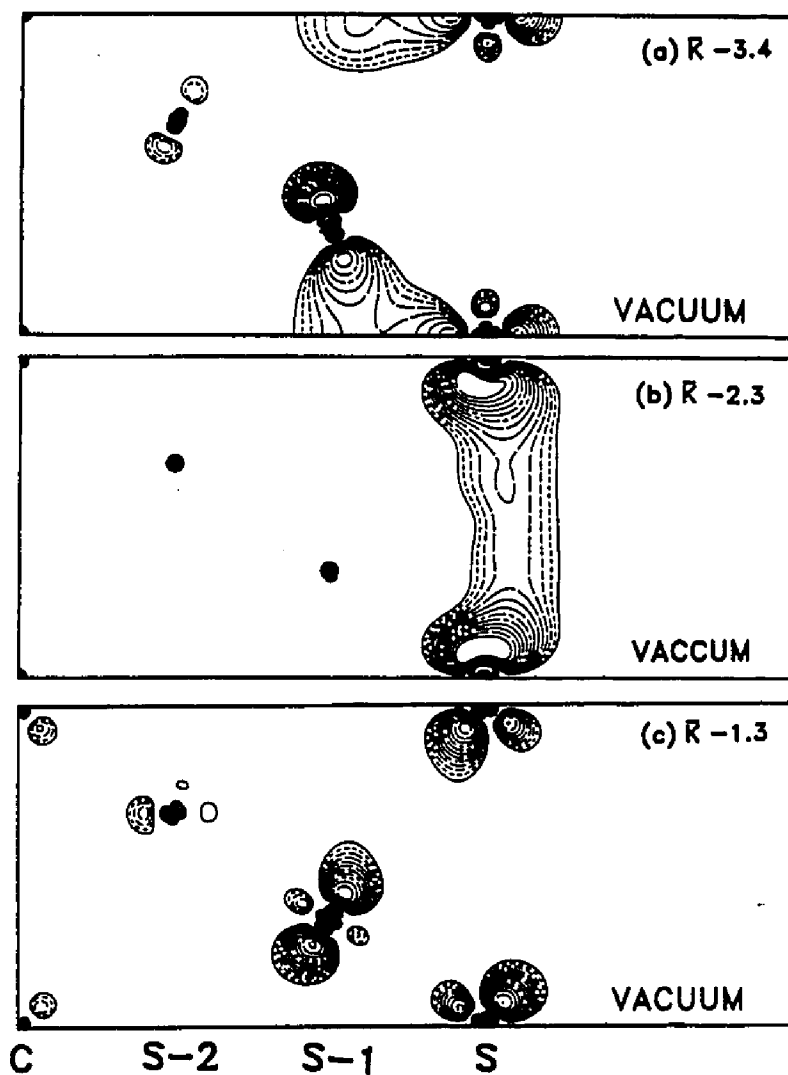


Figure 7.9 Surface states at  $\bar{K}$  (a) at  $-3.4$  eV, (b) at  $-2.3$  eV (doubly degenerate), and (c) at  $-1.3$  eV. See Fig. 7.5 for units.

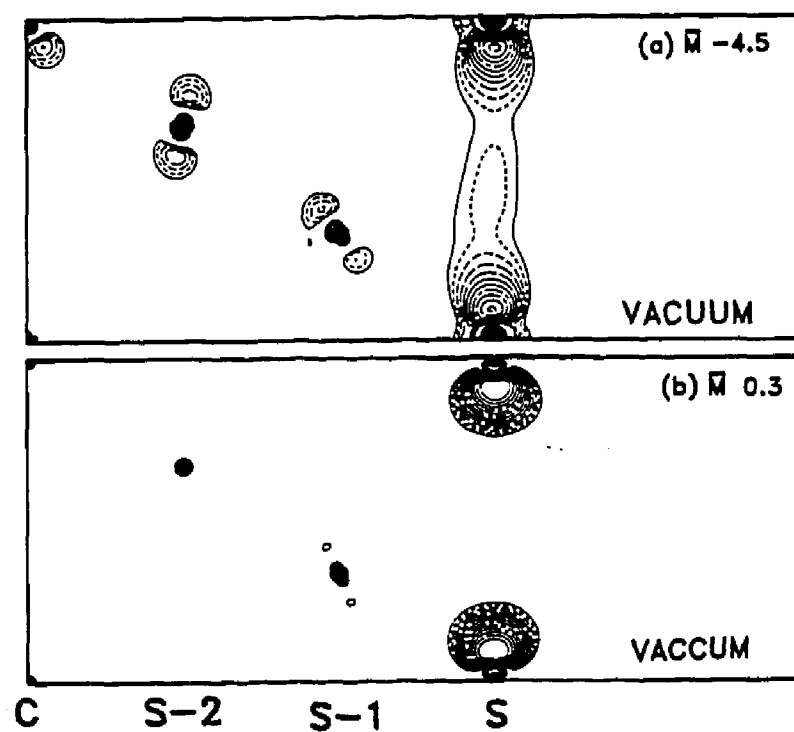


Figure 7.10 Surface states at  $\bar{M}$  (a) at -4.5 and (b) at 0.3 eV. See Fig. 7.5 for units.

degenerate occupied surface state at -2.4 eV (-1.9 eV PP calculation) at  $\bar{\Gamma}$  (Fig. 7.8 (b) ) and 1.3 eV (-1.0 eV PP calculation) at  $\bar{K}$  (Fig. 7.9 (c)) are similar to, however, more delocalized than those of Louie.

## 7.5 SUMMARY

We report accurate LAPW calculations for the bulk Pd and Pd(111) surface. For the bulk Pd, the calculated ground state properties are in good agreement with experiment, but, the cohesive energy is overestimated. The relativistic effects reduce the lattice constant, increase the bulk modulus, and increase the cohesive energy. The spin-orbit interaction has virtually no effect upon the structural and cohesive properties. For the Pd(111) surface, the structure is very close to the ideal structure. There is very small (<1%) top layer spacing contraction. The surface states (resonances) are found to be similar, but lie consistently below the previous nonrelativistic calculation.



## Chapter VIII

### CONCLUSIONS

We have applied the LDA based general potential LAPW method to a wide variety of transition and f-electron materials. LDA works well for a number of materials (Ti, Zr, La, LaS, HgTe, HgSe, Pd), however, considerable sensitivity upon the particular forms of the local density exchange-correlation potential was found for the IVA metals Ti and Zr, and the IIIA metal La. The LDA seems to be inadequate for the localized 4f-electron system SmS. The phase transition sequences in HgTe and HgSe are correctly predicted. Hg d electrons is found to be important in determining the structural properties through the Hg d - chalcogen p hybridization, however, this p-d hybridization tends to be relatively inert throughout the various phase transitions. The total energy calculation on Pd(111) reveals that the surface relaxation on this surface is very small.

## References

- Alt58a S. L. Altmann and N. V. Cohan, Proc. Phys. Soc. 71, 383 (1958).
- Alt58b S. L. Altmann, Proc. R. Soc. A 244, 153 (1958); S. L. Altmann and C. J. Bradley, Phys. Lett. 1, 336 (1962); S. L. Altmann and C. J. Bradley, Phys. Rev. A 135, 1253 (1964); S. L. Altmann and C. J. Bradley, Proc. Phys. Soc. 92, 764 (1967).
- Alo78 J. A. Alonzo and L. A. Girifalco, Phys. Rev. B 17, 3735 (1978).
- Ami81 P. M. Amirtharaj, F. H. Pollak, and J. K. Furdyna, Solid State Commun. 39, 35 (1981).
- And68 K. Andres, Phys. Rev. 168, 708 (1968).
- And70 O. K. Andersen, Phys. Rev. B 2, 883 (1970).
- And75 O. K. Andersen, Phys. Rev. B 12, 3060 (1975), and reference therein.
- App76 J. A. Appelbaum and D. R. Hamann, Rev. Mod. Phys. 48, 479 (1976)
- Bar72 U. von Barth and L. Hedin, J. Phys. C 5, 1629 (1972).
- Bar84 G. A. Baraff and M. Schlüter, Phys. B 30, 1853 (1984).
- Bis79 O. Bisi and C. Calandra, Surf. Sci. 83, 83 (1979).
- Bla75 H. Blaster and J. Wittig, J. Low Temp. Phys. 21, 377 (1975).
- Blu60 W. E. Blumberg, J. Eisinger, V. Jaccarino, and B. T. Matthias, Phys. Rev. Lett. 5, 51 (1960).
- Bro65 C. G. Broyden, Math. Comp. 19, 577 (1965).
- Cad85 N. A. Cade and P. M. Lee, Solid State Commun. 56 637 (1985).

- Car63 M. Cardona and G. Harbeke, Phys. Rev. Lett. 8, 90 (1963).
- Car74 E. Caruthers, L. Kleinman, and G. P. Alldredge, Phys. Rev. B, 8, 3330 (1974).
- Cep78 D. M. Ceperley, Phys. Rev. B18, 3126 (1978); D. M. Ceperley and B. I. Alder, Phys. Rev. Lett. 45, 566 (1980). These results are parameterized in J. P. Perdew and A. Zunger, Phys. Rev. B 23 5048 (1981).
- Cha73 D. J. Chadi and M. L. Cohen, Phys. Rev. B 8, 5747 (1973).
- Cha84 P. Chatterjee, J. Phys. F 14, 2027 (1984).
- Che85 Y. Chen, C. -L. Fu, K. -M. Ho, and B. N. Harmon, Phys. Rev. B 31, 6775 (1985)
- Che86 J. R. Chelikowsky, C. T. Chan, and S. G. Louie, Phys. Rev. B 34, 6656 (1986).
- Che88 J. Chen, D.J. Singh, and H. Krakauer, Phys. Rev. B 38, 12834 (1988).
- Chr76 N. E. Christensen, Phys. Rev. B 14, 3446 (1976).
- Con86 H. Conrad, M. E. Kordesch, R. Scala, and W. Stenzel, J. Electron Spectrosc. Relat. Phenom. 38, 289 (1986); H. Conrad, M. E. Kordesch, W. Stenzel, M. Šunjić, B. Trninić-Radja, Surf. Sci. 178, 578 (1986).
- Cot75 R. I. Cottam and G. A. Saunders, J. Phys. Chem. Solids 36, 187 (1975).
- Dav84 J. W. Davenport, Phys. Rev. B 29, 2896 (1984).
- Dem77 J. E. Demuth, Surf. Sci. 65, 369 (1977).
- Dev85 Electronic Structure, Dynamics, and Quantum Structural Properties of Condensed Matter, ed. by J. T. Devreese and P. Van Camp, (Plenum Press, New York, 1985)
- Ebe81 W. Eberhardt, F. Greuter, and E. W. Plummer, Phys. Rev. Lett. 40, 1085 (1981).
- Ebe83 W. Eberhardt, S. G. Louie, and E. W. Plummer, Phys. Rev. 28, 465 (1983).
- Eli64 A. A. Eliseev et al., Russ. J. Inorg. Chem. 9, 565

- (1964).
- Fei79 P. J. Feibelman, J. A. Appelbaum, and D. R. Hamann, Phys. Rev. B 20, 1433 (1979).
- Fin74 M. Finnis and V. Heine, J. Phys. F 4, L37 (1974).
- Fis64. E. S. Fisher and C. J. Renken, Phys. Rev. 135, A482 (1964).
- For82 P.J. Ford, A. J. Miller, G. A. Saunders, Y. K. Yogurtçu, J. K. Furdyna and M. Jaczynski, J. Phys. C, 15, 657 (1982).
- Fro83 S. Froyen and M. L. Cohen, Solid State Commun., 43, 447 (1982), Phys. Rev. 28, 3258 (1983).
- Gee81 B. M. Geerken, A. M. Hoefsloot, R. Griessen, and E. Walker, Physics of Transition Metals 1980, Edited by P. Rhodes, ( Institute of Physics Conference Series; no 55, Bristol and London, 1981) p. 595.
- Gel83. C. D. Gelatt Jr., A. R. Williams, and V. L. Moruzzi, Phys. Rev. B 27, 2005 (1983).
- Glö78 D. Glötzel, J. Phys. F 8, L163 (1978).
- Glö83 D. Glötzel, J. Phys. F L163 (1978); R. Podloucky and D. Glötzel, Phys. Rev. B 27, 3390 (1983).
- Gul73 Y. Guldner, C. Rigaux, M. Grynberg, and A. Mycielski, Phys. Rev. B 8, 3875 (1973).
- Gun74 O. Gunnarsson, B. I. Lundqvist, and J. W. Wilkens, Phys. Rev. B 10, 1319 (1974).
- Gun76 O. Gunnarsson and B. I. Lundqvist, Phys. Rev. B 13, 4274 (1976).
- Gun79 O. Gunnarsson, M. Johnson and B. I. Lundqvist, Phys. Rev. B 20, 3136 (1979).
- Gun80 O. Gunnarsson and R. O. Jones, Phys. Scr. 21, 394 (1980).
- Gun81 O. Gunnarsson and R. O. Jones, Solid State Commun. 37, 249 (1981).
- Hai84 T. Hailing, G. A. Saunders, Y. K. Yogurtçu, H. Bach, and S. Methfessel, J. Phys. C: Solid State Phys., 17, 4559 (1984).

- Ham79 D. R. Hamann, Phys. Rev. Lett. 42, 662 (1979).
- Has87 K. C. Hass and D. Vanderbilt, in Proceedings of the 18th International Conference on the Physics of Semiconductors, edited by O. Engström (World Scientific, Singapore, 1987); p. 1181; J. Vac. Technol. A 5, 3019 (1987).
- Hat73 T. M. Hattox, J. B. Conklin, JR., J. C. Slater, and S. B. Trickey, J. Phys. Chem. Solids, 34, 1627, (1973).
- Hea80 R. A. Heaton and C. C. Lin, Phys. Rev. B 22, 3629 (1980).
- Hea84 R. A. Heaton and C. C. Lin, J. Phys. C 17, 1853 (1984).
- Hed71 L. Hedin and B. I. Lundqvist, J. Phys. C 4, 2064 (1971).
- Him78 F. J. Himpsel and D. E. Eastman, Phys. Rev. B 18, 5236 (1978).
- Hoh64 P. Hohenberg and W. Kohn, Phys. Rev. 136 (1964) B864.
- Hol83 E. Holzschuh, Phys. Rev. B 28, 7346 (1983).
- Hor84 R. Hora and M. Scheffler, Phys. Rev. B 29, 692 (1984).
- Hov79 M. A. Van Hove and S. Y. Tong, Surface crystallography by LEED, (Springer-Verlag, Berlin, 1979). (R26)
- Hua83 T.-L. Huang and A. L. Ruoff, Phys. Rev. B 27, 7811 (1983).
- Hua84 T.-L. Huang and A. L. Ruoff, Phys. Rev. B 31, 5976 (1984).
- Hul86 S. L. Hulbert, and P. D. Johnson, and M. Weinert, Phys. Rev. B, 34, 3670 (1986).
- Hyg70 E. H. Hygh and R. M. Welch, Phys. Rev. B 1, 2424 (1970); R. M. Welch and E. H. Hygh, ibid, B 4, 4261 (1971); ibid, B 9, 1993, (1974).
- Ihm79 J. Ihm, A. Zunger, and M. L. Cohen, J. Phys. C 12, 4409 (1979).
- Ihm81 J. Ihm and J. D. Joannopoulos, Phys. Rev. B 24,

- 4191 (1981); M. T. Yin and M. L. Cohen, ibid 26, 5668 (1982).; S. Froyen and M. L. Cohen, Solid State Comm. 43, 447 (1982).
- Iya76 K. Iyakutti, C. K. Majumdar, R. S. Rao, and V. Devanathan, J. Phys. F 6, (1976).
- Jac75 J. D. Jackson, Classical Electrodynamics, 2nd Edition (Wiley, New York, 1975).
- Jan85 H. Jansen, A. J. Freeman, and R. Monnier, Phys. Rev. B 31, 4092 (1985).
- Jay65 A. Jayaraman, Phys. Rev. 139, A690 (1965).
- Jay70 A. Jayaraman, V. Narayanamurti, E. Bucher, and R. G. Maines, Phys. Rev. Lett. 25, 1430 (1970).
- Jep71 O. Jepsen and O. K. Andersen, Solid State Comm. 9, 1763 (1971).
- Jep75a O. Jepsen, Phys. Rev. B 12, 2988 (1975).
- Jep75b O. Jepsen, O. K. Andersen, and A. R. Mackintosh, Phys. Rev. B 12, 3084 (1975).
- Joh67 D. L. Johnson and D. K. Finnemore, Phys. Rev. 158, 376 (1967).
- Joh82 P. D. Johnson and N. V. Smith, Phys. Rev. Lett. 49, 290 (1982).
- Kam74 G. N. Kamm and J. R. Anderson, Low Temperature Physics (Plenum, New York, 1974), Vol. 4.
- Kit76 C. Kittel, Introduction to Solid State Physics, 5th ed. (Wiley, New York, 1976)
- Koe75 D. D. Koelling and G. Arbman, J. Phys. F5, 2041 (1975).
- Koe77 D. D. Koelling and B. N. Harmon, J. Phys. C 10, 3107 (1977).
- Koh65 W. Kohn and L. J. Sham, Phys. Rev. 140 (1965) A1133, and L. J. Sham and W. Kohn, Phys. Rev. 145 (1966) B561.
- Kou89 J. Koukal, M. Šunjić, Z. Lenac, H. Conrad, W. Stenzel, and M. E. Kordesch, Phys. Rev. B 39, 4911 (1989).

- Kra79 H. Krakauer, M. Posternak, and A. J. Freeman, Phys. Rev. B 19, 1706 (1979).
- Kum75 K. Kumazaki, Phys. Status Solidi (a) 33, 615 (1975).
- Lan73 N. D. Lang, in Solid State Physics, edited by F. Seitz and D. Turnbull (Academic, New York, 1973), Vol. 28, p. 225.
- Lan83 D. C. Langreth and M. J. Mehl, Phys. Rev. B 28, 1809 (1983).
- Lar81 C. G. Larsson and P. O. Nilsson, Phys. Lett. 85A, 393 (1981).
- Ley74 L. Ley, R. A. Pollak, F. F. McFeely, S. P. Kowalczyk, and D. A. Shirley, Phys. Rev. B 9, 600 (1974).
- Lib65 D. Liberman, J. T. Waber, and D. T. Cromer, Phys. Rev. 137, A27 (1965).
- Loc57 J. M. Lock, Proc. Phys. Soc. London B70, 566 (1957).
- Lóp86a F. López-Aguilar and J. Costa-Quintana J. Phys. C:Solid State Phys. 19, 2485 (1986).
- Lóp86b F. López-Aguilar, J. Phys. C:Solid State Phys., 19, L735 (1986).
- Lou67a T. L. Loucks Augmented Plane Wave Method, (W. A. Benjamin, New York, 1967).
- Lou67b T. L. Loucks, Phys. Rev. 159, 544 (1967).
- Lou78 S. G. Louie, Phys. Rev. Lett. 40, 1525 (1978).
- Lou79a S. G. Louie, Phys. Rev. Lett. 42, 476 (1979).
- Lou79b S. G. Louie, K.-M. Ho, and M. L. Cohen, Phys. Rev. B 19, 1774 (1979).
- Lou85a S. G. Louie, Bull. of Am. Phys. Soc. 30, 546 (1985).
- Lou85b S. G. Louie in Electronic Structure, Dynamics, and Quantum Structural Properties of Condensed Matter, ed. by J. T. Devreese and P. Van Camp, (Plenum Press, New York, 1985) p. 335.

- Lun83 S. Lundqvist, Theory of the Inhomogeneous Electron Gas, ed. by S. Lundqvist and N. H. March, (Plenum Press, New York, 1983).
- Mac80 A. H. MacDonald, W. E. Pickett and D. D. Koelling, *J. Phys. C* 13, 2675 (1980)
- Mac81 A. H. MacDonald, J. M. Daams, S. H. Vosko, and D. D. Koelling, *Phys. Rev. B* 23, 6377 (1981).
- Mad82 Landolt-Börnstein: Numerical Data and Functional Relationships in Science and Technology, edited by O. Madelung (Springer-Verlag, Berlin, 1982), Vol. 17b.
- Mar80 F. S. Marsh, M. K. Debe, and D. A. King, *J. Phys. C* 13, 2799 (1980).
- Mar85 R. M. Martin in Electronic Structure, Dynamics, and Quantum Structural Properties of Condensed Matter, ed. by J. T. Devreese and P. Van Camp, (Plenum Press, New York, 1985) p. 175.
- Mat64 L. F. Mattheiss, *Phys. Rev.* 134, A970 (1964).
- McM81a A. K. McMahan, H. L. Skriver, and B. Johansson, *Phys. Rev. B* 23, 5016 (1981).
- McM81b A. K. McMahan, M. T. Yin, and M. L. Cohen, *Phys. Rev. B* 24, 7210 (1981).
- Mil81 A. J. Miller, G. A. Saunders, Y. K. Yogurtçu and A. E. Abey, *Phil. Mag. A* 43, 1447 (1981).
- Min86a B. I. Min, H. J. F. Jansen, T. Oguchi, and A. J. Freeman, *Phys. Rev. B* 34, 369 (1986).
- Min86b B. I. Min, H. J. F. Jansen, T. Oguchi, and A. J. Freeman, *J. of Mag. and Mag. Mat.* 59, 277 (1986).
- Mon76 H. J. Monkhorst and J. D. Pack, *Phys. Rev. B* 13, 5188 (1976).
- Mor73 A. Mortitani, K. Taniguchi, C. Hamaguchi, and J. Nakai, *J. Phys. Soc. Jpn.* 34, 79 (1973)
- Mor78 V. L. Moruzzi, J. F. Janak, and A. R. Williams, Calculated Electronic Properties of Metals (Pergamon, Oxford, 1978).
- Mue70 F. M. Mueller, A. J. Freeman, J. O. Dimmock, and A. M. Furdyna, *Phys. Rev. B* 1, 4617 (1970).



- Mur44 F. D. Murnaghan, Proc. Natl. Acad. Sci. U.S.A. 30, 244 (1944).
- Nor87 M. R. Norman and D. D. Koelling, J. Less-Common Met. 127, 357 (1987).
- Ono82 A. Onodera, A. Ohtani, M. Motobayashi, T. Seike, O. Shimomura, and O. Fukunaga, in Proceedings of the 8th AIRAPT conference, Uppsala, Sweden, 1981, edited by C. M. Backman, T. Johannisson, and L. Tegner (Arkitektkopia, Uppsala, 1982), Vol. I, p321.
- Ohi82 A. Ohtani, T. Seike, M. Motobayashi and A. Onodera, J. Phys. Chem. Solids 43, 627 (1982).
- Oht87 H. Ohtani, M. A. Van Hove, and G. A. Somorjai, Surf. Sci. 187, 372 (1987).
- Par51 D. H. Parkinson, F. E. Simon, and F. H. Spedding, Proc. R. Soc. London A207, 137 (1951).
- Per81 J. P. Perdew and A. Zunger, Phys. Rev. B 23, 5048 (1981).
- Pic80 W. Pickett, A. J. Freeman, and D. D. Koelling, Phys. Rev. B 22, 2695 (1980).
- Pic81 W. E. Pickett, A. J. Freeman and D. D. Koelling, Phys. Rev. B 23, 1266 (1981).
- Pic84 W. E. Pickett and C. S. Wang, Phys. Rev. B 30, 4719 (1984).
- Raj73 A. K. Rajagopal and J. Callaway, Phys. Rev. B 7, 1912 (1973).
- Sco64 W. J. Scouler and G. B. Wright, Phys. Rev. 133, A 736 (1964).
- Sha83 L. J. Sham and M. Schlüter, Phys. Rev. Lett. 51, 1888 (1983).
- She73 N. J. Shevchik, J. Tejeda, M. Cardona, and D. W. Langer, Phys. Status Solidi B 59, 87 (1973).
- Sla37 J. C. Slater, Phys. Rev. 51, 151 (1937).
- Sla51 J. C. Slater, Phys. Rev. 81, 385 (1951).
- Sla72 J. C. Slater and K. H. Johnson, Phys. Rev. B 5, 844 (1972).

- Sin75 S. P. Singhal, Phys. Rev. B 12, 564 (1975).
- Sin86 D. J. Singh, H. Krakauer, and C. S. Wang, Phys. Rev. B 34, 8391 (1986); and references therein.
- Sin88 D. J. Singh and H. Krakauer, Phys. Rev. B, 37, 3999 (1988).
- Spe61 F. H. Spedding, J. J. Hanak, and A. H. Daane, J. Less-Common Met., 3, 110 (1961).
- Sta84 C. Stassis and J. Zarestky, Solid State Commun. 52, 9 (1984).
- Sti85 J. Sticht and J. Kübler, Solid State Comm. 54, 389 (1985).
- Str84 P. Strange, J Phys. C:Solid State Phys. 17, 4273 (1984).
- Sya75 K. Syassen and W. B. Holzapfel, Solid State Comm., 16, 553. (1975).
- Tak79 T. Takeda and J. Kübler, J. Phys. F 9, 661 (1979).
- Tom86 D. Tománek, S. G. Louie, and C.-T. Chan, Phys. Rev. Lett., 57, 2594 (1986).
- Tri73 S. B. Trickey, F. R. Green, Jr., and F. W. Averill, Phys. Rev B 8, 4822 (1973).
- Vil85 P. Villars and L. L. Calvert, Pearson's Handbook of Crystallographic Data for Intermetallic Phases (American Society for Metals, Metals Park, Oh, 1985).
- Vla85 S. V. Vlasov and O. V. Farberovich, Solid State Comm., 56, 967 (1985).
- Vos80 S. H. Vosko, L. Wilk and M. Nusair, Can. J. Phys. 58, 1200 (1980); S. H. Vosko and L. Wilk, Phys. Rev. B 22, 3812.
- Wan86 X. W. Wang, B. N. Harmon, Y. Chen, K.-M. Ho, C. Stassis, and W. Weber, Phys. Rev. B 33, 3851 (1986).
- Wei81 M. Weinert J. Math. Phys. 22, 2433 (1981).
- Wei82 M. Weinert, E. Wimmer, and A. J. Freeman, Phy. Rev. B 26, 4571 (1982).

- Wei85 S. H. Wei, Ph. D. Disseration First Principles Structure Calculations Using the General Potential LAPW Method (College of William and Mary, 1985)
- Wei87 S.-H. Wei, A. A. Mbaye, L. G. Ferreira, and A. Zunger, *Phy. Rev. B* 36, 4163 (1987).
- Wei88 S. -H. Wei and A. Zunger, *Phys. Rev. B* 37, 8958 (1988).
- Wer83 A. Werner, H. D. Hochheimer, K. Strössner and A. Jayaraman, *Phys. Rev. B*, 28 3330 (1983).
- Wes84 D. A. Wesner, P. D. Johnson, and N. V. Smith, *Phys. Rev. B*, 30, 503 (1984).
- Wig34 E. Wigner, *Phys. Rev.* 46, 1002 (1934).
- Wim85 E. Wimmer, H. Krakauer, and A. J. Freeman, in Advances in Electronics and Electron Physics, edited by P. W. Hawkes (Academic, New York, 1985), Vol. 65, p. 357.
- Ye87 Y.-Y. Ye, Y. Chen, K.-M. Ho, B. N. Harmon, and P.-A. Lindgård, *Phys. Rev. Lett.*, 58, 1769 (1987).
- Yin80 M. T. Yin and M. L. Cohen, *Phys. Rev. Lett.* 45, 1004 (1980).
- Yin82 M. T. Yin and M. L. Cohen, *Phys. Rev. B* 26, 5668 (1982).

VITA

Zhi Wei Lu

Born in Jiang Su Province, China, october 29, 1962.  
Graduate from Nanjing University, Nanjing, China, July 1983  
with a B.S. in Physics. Received an M.S. at College of  
William and Mary in 1984 and completed Ph. D. requirments in  
physics, May, 1989.